MOUNTAIN-PLAINS CONSORTIUM

MPC 23-495 | H.N. Mahmoud and E.M. Hassan

EVALUATION OF A NEW DOUBLE-COMPOSITE SIMPLY-SUPPORTED STEEL BRIDGE SYSTEM

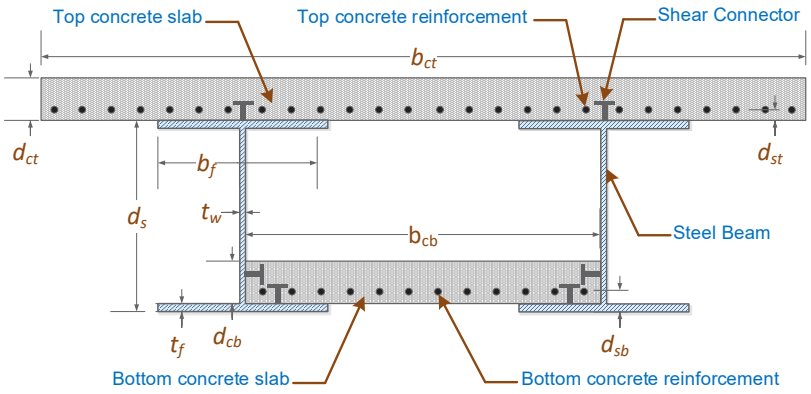

MOUNTAIN-PLAINS CONSORTIUM REGION 8

A University Transportation Center sponsored by the U.S. Department of Transportation serving the Mountain-Plains Region. Consortium members:

Colorado State University
North Dakota State University
South Dakota State University
University of Colorado Denver
University of Denver
University of Utah
Utah State University
University of Wyoming

Evaluation of a New Double-Composite Simply-Supported Steel Bridge System

Hussam N. Mahmoud

Emad M. Hassan

Department of Civil and Environmental Engineering
Colorado State University
Fort Collins, CO 80523

March 2023

Acknowledgments

The funds for this study were provided, in part, by the United States Department of Transportation to the Mountain-Plains Consortium (MPC). Matching funds were provided by Colorado State University. The data for this study, provided by Colorado State Patrol and Colorado Department of Transportation, are greatly appreciated.

Disclaimer

ABSTRACT

Built-up plate girders are considered a viable solution for long-span bridges due to their ability to meet the requirements for deflection limits. They are made up of flanges, webs, and stiffeners, which are typically welded together. The webs in plate girders are relatively thin, which requires the addition of transverse stiffeners to achieve the required shear capacity. The thin webs can also corrode through fairly quickly once corrosion begins. From a maintenance perspective, the added stiffeners to enhance the shear capacity can trap debris and moisture on the bottom flange. This can give rise to corrosion fatigue, which is not addressed in the AASHTO Design Specifications. On the other hand, the use of rolled beams in steel bridges can be very advantageous since the webs are an integral part of the flanges in that the beams are rolled out of one piece of steel and the webs are significantly thicker than built-up girder webs. Therefore, there is no need for transverse stiffeners to enhance the shear capacity of the web. From a maintenance and deterioration perspective, the beams have smoother lines with no stiffeners to trap moisture and debris on the bottom flange.

Despite their advantages, rolled beams are limited in size, which imposes constraints on their use to relatively short spans due to deflection requirements. The main overarching goal of this project is to propose a new superstructure system, which utilizes rolled beams in combination with reinforced concrete slabs, resting on the bottom flanges of the beams, to enhance the deflection of the system and allow for longer spans to be built using rolled beams. This was realized through various tasks that include 1) devising a mathematical/analytical formulation that allows for rapid assessment of the non-linear response of double composite bridges, 2) developing finite element models using commercial software that can capture the overall linear and non-linear response of the bridge in addition to the response of various components, 3) validating the results of the mathematical formulation against the results of the finite element models, and 4) using the developed tools to compare and assess the improvements in deflection and moment capacity for double composite bridges over single composite bridges.

The significance of this work includes the formulation of the mathematical model, which can readily be used by structural engineers to evaluate the behavior of the bridges, the development of the linear and non-linear models, and the parametric studies and the associated findings. The results of the numerical finite element analyses were shown to be in very good agreement with the mathematical model. The results showed substantial enhancement of the overall bridge deflection and capacity for double composite sections over their single composite counterparts.

TABLE OF CONTENTS

LIST OF FIGURES

Nomenclature

w : the steel beam web thickness (*inch*)
d_s : the steel beam total depth (*inch*)
b : the steel beam flange width (*inch*)
t_f : the steel beam flange thickness (*inch*)
b_{ct} : top concrete effective width (*inch*)
d_{ct} : top concrete depth (*inch*)
b_{cb} : bottom concrete effective width (*inch*)
d_{cb} : bottom concrete depth (*inch*)
d_{sb} : distance from the edge of bottom flange of the steel beam to the bottom slab reinforcement (*inch*)
ρ : reinforcement ratio for the bottom slab
E_s : steel elastic modulus (*ksi*)
E_c : concrete elastic modulus (*ksi*)
f_y : steel yield stresses (*ksi*)
f_c : concrete yield stresses (*psi*)
e_{st} : strain hardening for steel
e_{yc} : yield strain for concrete
e_{ys} : yield strain for steel
e_u : ultimate concrete strain
A_s : Steel total area ($inch^2$)
A_f : Steel flanges area ($inch^2$)
I_s : Moment of inertia of the steel ($inch^4$)
n : Ratio between the steel elastic modulus to the concrete elastic modulus
A_{ct} : Concrete upper section area ($inch^2$)
A_{cb} : Concrete bottom section area ($inch^2$)
A_c : Concrete section total area ($inch^2$)
I : Cross-section moment of inertia ($inch^4$)
M : Moment resistance of the composite section
K : Section curvature
c : Max compressive stresses in the upper concrete
α : Location of the neutral axis in the steel beam
η : Percent plastification in the steel beam
μ : Location of the neutral axis in the concrete slab
ξ : Percent plastification in the concrete slab

1. INTRODUCTION

1.1 Overview

The increased number of constructed bridges around the United States and the growing requirement for speed of construction, especially for moderate- to long-span bridges, as well as low maintenance cost, encourage the use of hot rolled steel sections instead of the built-up sections. The use of built-up sections, while it has its own advantages, requires more time to fabricate. In addition, since built-up girders are made up of flanges, webs, and stiffeners, which are typically welded together, they could be susceptible to fatigue cracking, which could manifest at the welded details. Moreover, the webs are relatively thin, which requires the addition of transverse stiffeners to achieve the required shear capacity. The thin webs can also corrode through fairly quickly once corrosion begins. From a maintenance perspective, the added stiffeners to enhance the shear capacity can trap debris and moisture on the bottom flange. This can give rise to corrosion fatigue, which is not addressed in the AASHTO Design Specifications (American Association of State Highway and Transportation Officials 2012). The use of rolled beams in steel bridges, on the other hand, can be very advantageous since the webs are an integral part of the flanges in that the beams are rolled out of one piece of steel and the webs are significantly thicker than built-up girder webs. Therefore, there is no need for transverse stiffeners to enhance the shear capacity of the web. From a maintenance and deterioration perspective, the beams have smoother lines with no stiffeners to trap moisture and debris on the bottom flange. Despite their advantages, rolled beams are limited in terms of their depth, which confine their use to relatively short spans due to deflection requirements.

To mitigate the deflection limitations of hot-rolled beams in long-span bridges, a newly proposed superstructure, which utilizes rolled beams in combination with a reinforced concrete slab resting on the bottom flanges of the beams, is being proposed. The added slab increases the cross-sectional moment of inertia, thereby lowering the deflection of the whole system. The bottom slab also significantly enhances the torsional stability of the bridge as the geometry of the bridge is transformed to a closed section. The enhanced torsional stability eliminates the need for cross-bracing or lateral bracings, which eradicates potential problems associated with distortion fatigue at the web gab. In addition, the new system will employ the Simple Made Continuous concept (SMC) where the connection of the spans over the pier is "simple for dead – continuous for live" or SD-CL. Typically, continuous bridges are more economical than simple span bridges because they develop smaller positive interior span moments due to the negative moments at the continuous ends. The advantage of double composite over a single composite bridge is also evident in that single composite sections are not effective in negative moment regions close to the supports where the concrete is subjected to tensile stresses. Therefore, the use of double composite sections shall enhance the overall flexural stiffness of the cross-section, particularly in the negative moment region.

1.2 Scope of the Study

This report presents an analysis of a double composite section to quantify the enhancement that can be gained by employing them in bridge construction. The report pertains primarily to the development of analytical/mathematical and numerical finite element tools that can allow structural engineers to evaluate the performance of double composite sections for any bridge span. Three analysis methods are discussed in this report: 1) analytical/mathematical formulation of section analysis, 2) finite element analysis approach using SAP2000, and 3) numerical finite element analysis using ABAQUS, which is a general-purpose finite element software capable of handling nonlinear analysis. The presented analytical approach considers two cases for composite sections: open section, in which no effect of concrete under tensile stresses is considered; and closed section, where the effect of concrete reinforcement under tensile stresses is considered.

1.3 Organization of Report

The current study primarily focuses on the analysis of double composite bridges using 1) non-linear numerical modeling, and 2) linear and non-linear finite element modeling using SAP2000 and ABAQUS finite element packages. Chapter 2 is a comprehensive literature review of the applications and recent research efforts pertaining to double composite bridges. In Chapter 3, the analytical/mathematical approach devised to determine a double composite section capacity is presented. Chapter 4 provides detailed descriptions of the developed numerical finite element models for the double composite bridge. In Chapter 5, a discussion of the results from the numerical and analytical models is presented, and a comparison between the double composite bridge system and the conventional single composite bridge is made.

2. BACKGROUND AND LITERATURE REVIEW

A traditional composite section consisting of a top concrete slab supported by steel beams is commonly used in bridge and building construction. Advantages of using a composite section include increasing the total moment of inertia of the section, restraining the compression flange of the steel section against lateral-torsional buckling, reducing the overall bridge deflection, and increasing the global stiffness, which can eventually allow more economic sections to be used and longer spans to be constructed. These advantages could also be realized if the concrete of an additional concrete slab is placed to provide a composite section with the bottom flanges of the steel section. In doing so, a "double composite" section is created since the section would have both a top and a bottom concrete slab and its behavior is thought to follow that of a composite section for the positive and negative moments.

Many studies were conducted on understanding the behavior of single composite sections (Abbiati et al. 2018; Culver 1960; Matos et al. 2019) and most code provisions have provided adequate guidelines to design these sections for service and ultimate loads (ACI Committee 318 2014; American Association of State Highway and Transportation Officials 2012; EN 1992-1-1 1992). While double composite sections are uncommon in bridge constructions, their usage surprisingly started in 1978 (Patel 2009). The limited usage of the double composite sections is reflected also in the limited number of research studies that have been conducted on these sections (Deng and Morcous 2013; Mendes 2010; Saul 1997; Stroh et al. 2010; Xu et al. 2011). This study aims to significantly advance in understanding the behavior of double composite systems. The proposed section to be evaluated in this study is schematically shown in Figure 2.1. The section comprises a top and bottom slab that are composite with steel beams to form a box section.

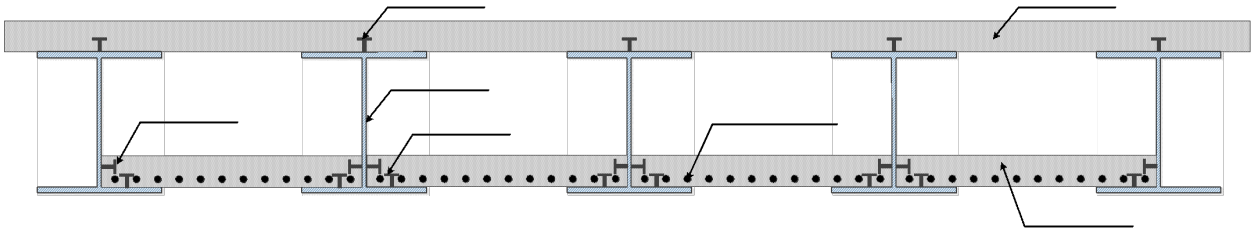

Figure 2.1 Cross-sectional view of the proposed double composite bridge system

2.1 General

A box-girder bridge is one in which the main beams are made of girders in the shape of a hollow box. A typical box girder comprises either prestressed concrete, structural steel, or a combination of both and is rectangular or trapezoidal in cross-section, as shown in Figure 2.2. This closed section has a much greater torsional stiffness and strength than an open section, which makes an attractive alternative, particularly for curved or skewed bridges. In recent years, single or multi-cell reinforced concrete box-girder bridges have been widely used in modern highway systems for over crossings, under crossings, grade separation structures, and viaducts. The closed cellular section of the boxes makes the structure beneath it more aesthetically pleasing than an open-web type system. In the case of long-span bridges, prestressing cables are accommodated in section flanges. Box interiors can be used to accommodate service utilities such as gas pipes, water mains, and others. In addition to their structural advantages, maintenance of box girder bridges is easier since the interior space is directly accessible without the need to use scaffolding. The bottom flange is often wider, leading to greater bending moment resistance and, as a result, it has high structural efficiency, which minimizes the pre-stressing force required to resist a given bending moment.

Box girders can also be classified according to the materials used for construction, which are mainly concrete, steel, and hybrid box girders.

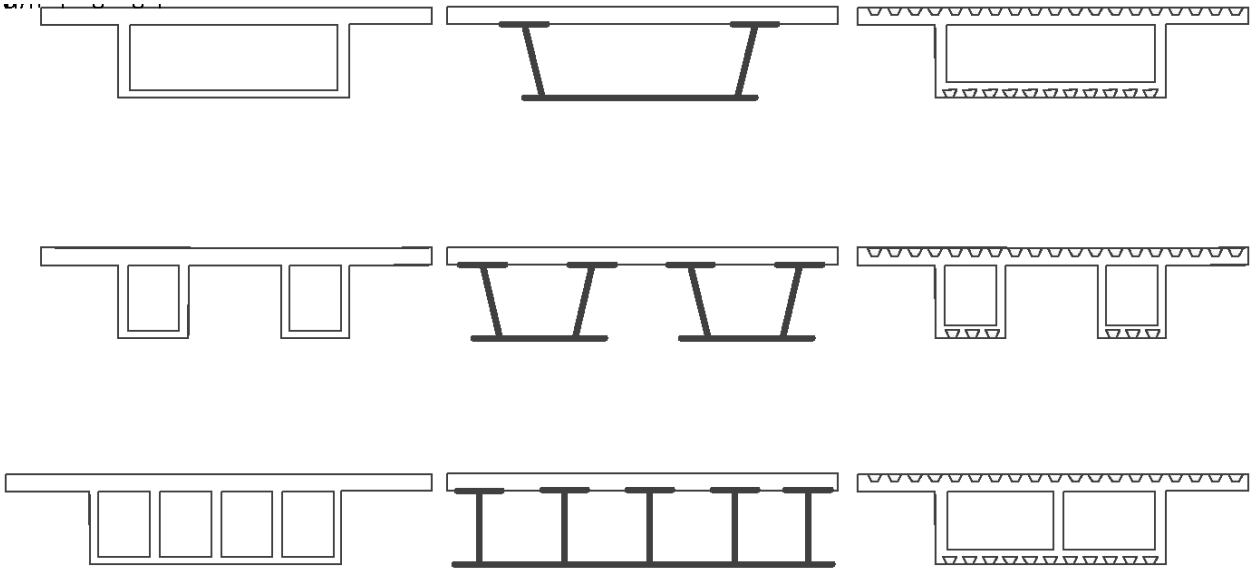

Figure 2.2 Box girder classification: *redrawn from* (Sennah and Kennedy 2002)

Concrete box girders

Concrete box girders are unique in that they are typically built in short sections. Figure 2.3 shows an example of a typical concrete box girder. To reduce the fabrication costs associated with formwork and pre-casting, the segments are usually cast-in-place instead of precast. This type of bridge becomes more economical as the span length increases. If less than 100 segments are to be used, then other bridge types could become more attractive cost-wise. Casting the segments in place removes the need for a casting yard, specialized forms, and transportation of the girders, which also reduces the cost. However, for bridges more than 80 feet high, there will be significant challenges with setting up formwork or even getting large enough cranes to the site. This may actually turn out to be an advantage given that the bridge will span the creek, and as such machinery at the ground level will be reduced. On the other hand, there is a low chance that local contractors will be familiar with this construction method. As a result, contractors and labor may have to be brought from other places, which could dramatically increase costs.

Figure 2.3 Example of concrete box girder bridge (Wordpress 2015)

Steel box girders

Steel box girders are normally fabricated off-site and lifted into place by cranes, with sections connected by bolting or welding. If a composite concrete bridge deck is used, it is often cast-in-place using temporary falsework supported by the steel girder. Figure 2.4 shows an example of a typical steel box girder. These are lightweight comparatively, and longer spans are viable. Costs may be reduced as fewer piers are needed to support the bridge. Due to its high torsional stiffness, steel box girder bridges handle curvature well and are ideal for horizontally curved bridges. Lastly, steel box girders are considered to be aesthetically pleasing because of their smooth and clean lines. However, issues associated with steel corrosion and maintenance could mount to large costs throughout the lifetime of the bridge. Another factor in maintenance is accessibility within the confined space within the steel box. These girders are also expensive because of the reduced options for automated fabrication.

Figure 2.4 Example of steel box girder bridge (SteelConstruction.info 2019)

Hybrid box girders

Hybrid box girder bridges are those that have an additional concrete slab cast between the bottom flanges to provide additional stiffness to the structure. These bridges are built by launching the deck from both abutments, with all the structural steel, the complete bottom concrete, and the top precast slabs being present, not yet connected to the deck. The top reinforcement steel is also placed in its final position, leaving the bridge ready once closed, to pour the concrete on the top slab.

These bridges offer higher torsional resistance comparatively. Compression stresses from bending keep the bottom slab to crack less, so bending resistance is higher than those of steel or concrete box girders. Double composite action greatly improves the deformational and dynamic response to both bending and torsion. However, compared with conventional composite decks, hybrid girder bridges are expected to have longer construction time due to the implementation of the lower slabs and the higher dead load of the structure, which may need more expensive bearing supports piers and foundations.

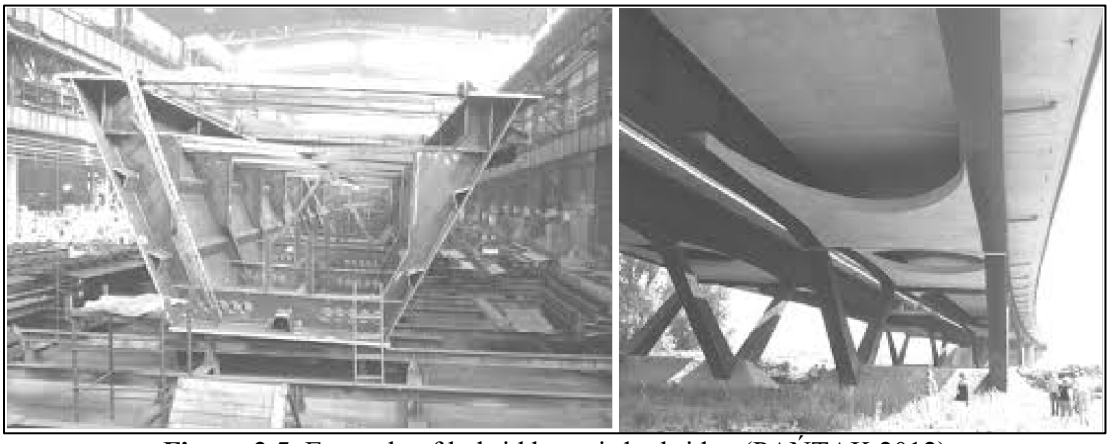

Figure 2.5 Example of hybrid box girder bridge (PAŃTAK 2012)

2.2 Previous Studies on Double Composite Bridges

Long-span bridges, which generally refer to bridges with spans over 1,000 ft, are built using various structural systems based on the required functions and limitations of each bridge (Miranda, M. 2016). One of the main components of bridges is the girder, which can be built using different materials based on the load applied and the bridge span. Since deflection and cost typically control the design of bridges, the maximum bridge span changes by the girder system since the girder size has a substantial effect on the overall deflection. For example, concrete box girders can cover up to a 120-ft span; prestressed concrete box girders can work for spans up to 200 ft; and the maximum span for steel box girders can reach 400 ft (Bharil, R.K. 2016). Historically, the concrete box girder bridges first appeared in the 1950s. Long-span concrete girder bridges use a box cross-section because of its structural advantages. This section is able to resist both positive and negative moments present in continuous bridges because it has both top and bottom flanges. The large torsional strength and rigidity of a closed section are favorable for resisting torsional moments due to curved alignments or eccentric live loads (Rodriguez 2004). The dimensioning of the cross-section is a critical step in the design of a long-span concrete bridge and is influenced by the construction method and the post-tensioning layout.

Steel and composite steel-concrete box girders, on the other hand, have recently become increasingly popular as bridge superstructures. This is because they are a) structurally efficient because of their high torsional rigidity, b) aesthetically pleasing because of their long span with shallow depth, and c) highly economical in fabrication and maintenance because of their segmental type of construction (Yen 1982).

Deng and Marcos (2013) introduced a new double composite system where a lightweight W-shaped steel section was used with a cast-in-place concrete deck connected to its top flange and pre-tensioned concrete connected to its bottom flange, as shown in Figure 2.6. The presented composite section by Deng and Marcos was light in weight, more durable, and easier to fabricate compared with a single composite section. In spite of the previously mentioned advantages of box sections, it behaved as an open section, and the advantages of box sections were not fully realized. This research was only focused on the linear behavior of the double composite section, and the non-linear behavior was ignored.

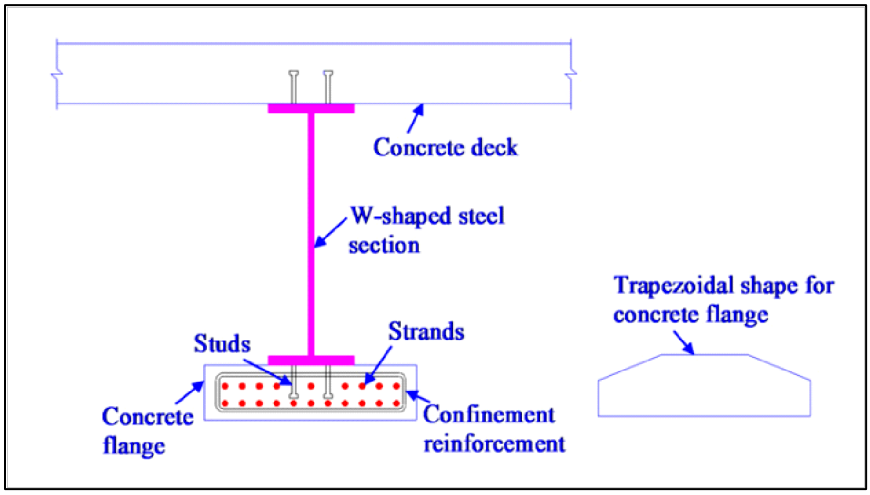

Figure 2.6 Double composite system introduced by Deng and Marcos (2013)

Mendes (2010) performed a bending analysis of two different bridges using double composite sections. The author also compared the performance of double composite and single composite sections to highlight the significance of using the double composite section. This study noted that bridges with double composite sections use less structural steel per unit area, have a higher resistance to bending

moments, and better response to torsional effects when compared with a conventional single composite bridge. Similar to the other double composite analysis, this work ignored the non-linear behavior. One of the analyzed bridges is shown in Figure 2.7.

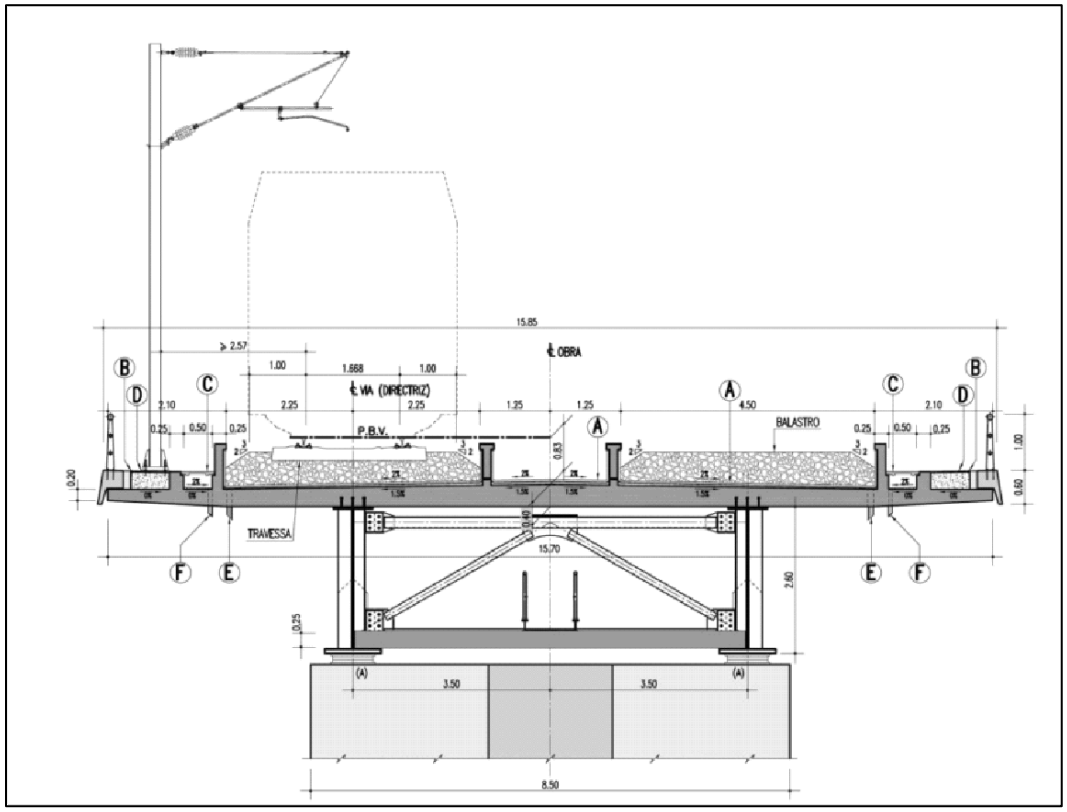

Figure 2.7 Double composite bridge analyzed by Mendes (2010)

Xu et al. (2011) experimentally tested a double composite bridge to investigate the behavior of this section in negative flexural regions. A two-span composite box girder system was manufactured and tested. The first bridge was a conventional single composite bridge and the second was a double composite bridge with reinforced concrete slabs connecting both the top and bottom flanges. This research showed that attaching an additional concrete slab to the steel bottom flange is an effective way to increase the overall sectional stiffness and local buckling strength of the steel. The focus of this study was to evaluate the mechanical properties, assess concrete cracking, determine the sectional plastic hinges, and estimate the load-carrying capacity of the double composite bridges. An experimental test setup composed of two loading points with two edge supports and one middle support was utilized to test the bridges, as shown in Figure 2.8.

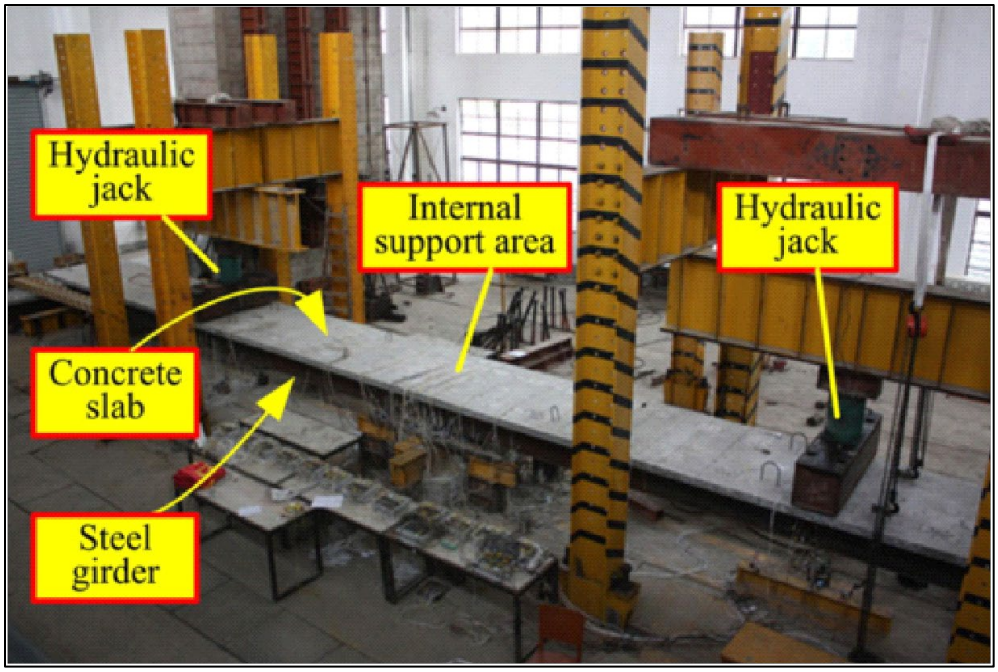

Figure 2.8 Experimental test setup for a double composite bridge by Xu et al. (2011)

Saul (2010) conducted an experimental investigation of a double composite high-speed railway bridge. The study evaluated the fatigue performance of the double composite bridges. A short span with a two-girder bridge was tested under a negative moment, and crack initiation and distribution were monitored during the fatigue test. Figure 2.9 shows the tested specimen and the crack distribution after 2.0 million cycles when the full plastic capacity of the tested bridge was reached. The widest crack measured in the slab was 0.0078 in.

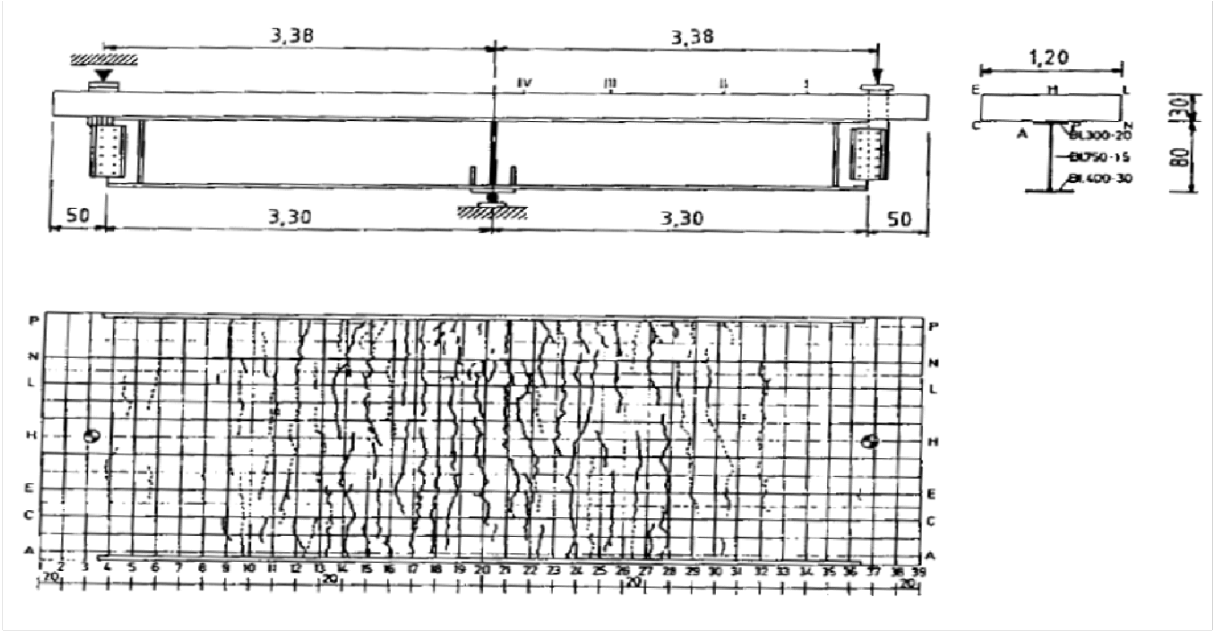

Figure 2.9 Test specimen details and crack distribution in the tested double composite bridge by Saul (1997)

As part of the research conducted at the University of South Florida and Florida Department of Transportation Research Center (Florida DOT), Stroh et al. (2010) performed a series of experimental tests as well as finite element analysis for a double composite box girder bridge. The goal of this project was to provide Florida DOT with the necessary evaluations, testing, and verification that would facilitate the implementation of the double-composite concept in future bridge construction using high-performance steel. A prototype bridge was designed and fabricated and then tested under service, fatigue, and ultimate loading condition. The structural response of the bridge for each loading case was evaluated. The test specimen comprised a full-scale box girder 48 ft long, 16 ft wide, and 4 ft 10⅛ in deep, representing a section of a bridge between inflection points. A cross-section view of the tested bridge is shown in Figure 2.10. The specimen was designed to be supported at the middle; however, this was not possible. As a result, it was asymmetrically supported with spans of 23 ft and 25 ft. The load was applied at the free end of the longer span while a hold-down frame prevented movement at the other end. The double composite showed potential significance for good performance and cost savings compared with the conventional bridge system.

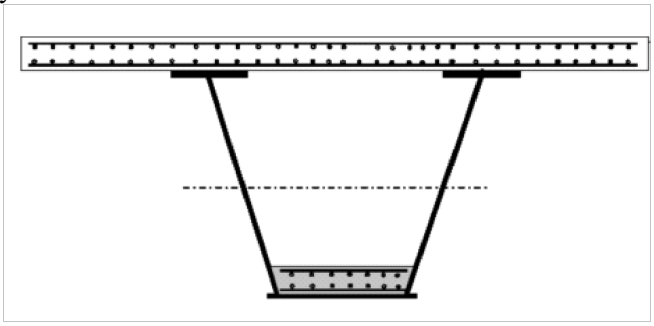

Figure 2.10 Cross-section view of the tested double composite bridge by Stroh et al. (2010)

Code provisions, to date, provide limited information and guidance on the design of double composite sections. However, it is logical to assume that double composite bridges should be designed against limit states similar to those in which single composite is designed for including, for example, serviceability, strength, and fatigue (Patel 2009). The components to be designed to these limit states would include reinforcements in the top and bottom slabs, concrete deck, steel webs and flanges, shear connector, etc.

2.3 Double Composite Bridge Applications

Over the years, several conventional single composite bridges were built, but very limited applications have been realized for double composite bridges worldwide (Stroh et al. 2010). The first double composite bridge was built in Ciaran, Spain, in 1978. Several models of this bridge were found in Europe, but this design has yet to be implemented in the U.S. (Stroh and Sen 2009). Other examples of bridges that utilized double composite sections can be found around the world. Examples include the following:

*Highway Bridge over the Odra River in Ostrava, Czech Republi*c: This bridge is located within highway D-1 near the Polish-Czech border crossing Chałupki-Starý Bohumín. The total length of the bridge is 871 ft (265.5 m). The bridge was built using a continuous double composite beam with five spans and a maximum span length of 277 ft (84.5 m). The cross-section consists of two steel plate girders made of steel combined with a reinforced concrete deck (PAŃTAK 2012). A general view of the bridge, shown in Figure 2.11, includes the bridge support and the bottom slab that is only used in the negative moment regions.

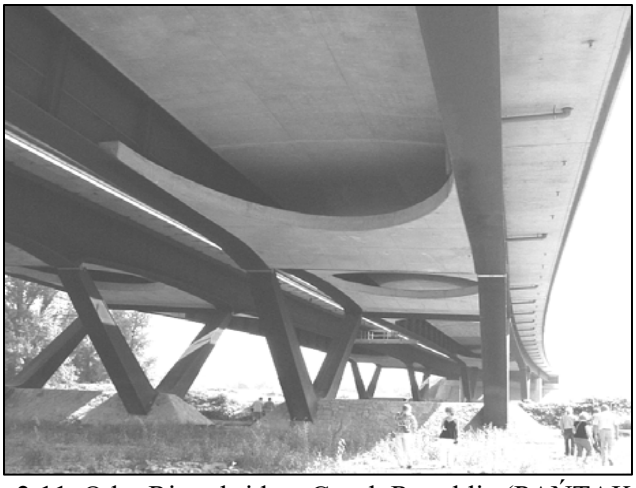

Figure 2.11 Odra River bridge, Czech Republic (PAŃTAK 2012)

Highway bridge over the Ostravice River in Ostrava, Czech Republic: Another example of a double composite bridge is in the Czech Republic within highway D-1 in Ostrava over the Ostravice River. With four spans wide and continuous girders, this bridge opened in 2005 with a total length of 955 ft (~291 m) and a maximum span length of 329 ft (~100 m). The bridge main girder is a single cell composite box girder with variable height and longitudinally prestressed to reduce the bridge weight (PAŃTAK 2012). Figure 2.12 shows a general view of the bridge's main girder.

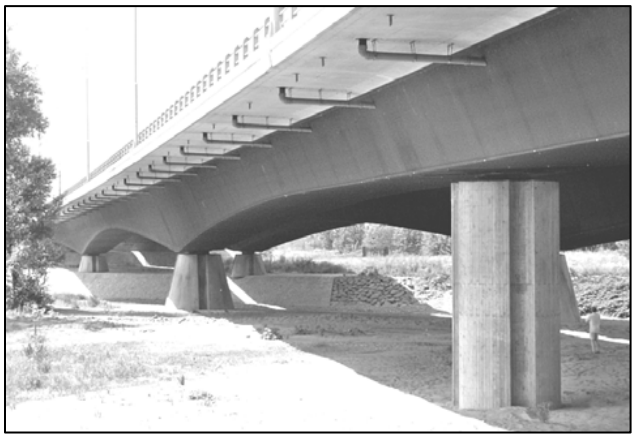

Figure 2.12 Ostravice River bridge, Czech Republic (PAŃTAK 2012)

Bridge over the Elbe River in Torgau, Germany: The Elbe bridge in Torgau is a 1,670-ft-long (~509 m) road bridge that lies in the federal highway 87, which connects Leipzig with Frankfurt, Germany. This bridge was opened in 1993 with two lanes, sidewalks, and bike paths on both sides. The bridge was built using a double composite section with prestressed concrete elements as a superstructure. The bridge main girder is a continuous composite section with six intermediate supports. The maximum bridge span is 213 ft (~65.0 m), which is located in the middle of the bridge. Figure 2.13 shows a general view of the bridge and its main girder.

Figure 2.13 Elbe River in Torgau bridge, Germany (PAŃTAK 2012)

Bridge over the Inn River in Neuötting: The Inn River bridge in Neuötting is a 1542-ft-long (~470 m) and 97 ft-wide (~30 m) bridge that lies along the A94 Motorway, Germany. This bridge was opened in 2000 as a freeway bridge (PAŃTAK 2012) and was built using a double composite section with a variable depth girder. The bridge main girder is a continuous composite section with four intermediate supports. The maximum bridge span is 505 ft (~154 m), which is located in the middle of the bridge. Figure 2.14 shows a general view of the bridge and its main girder.

Figure 2.14 Inn River in Neuötting bridge, Germany (PAŃTAK 2012)

Bridge over the Nalón River in Langreo, Spain: The bridge over the Nalón River in Langreo is 1,542 ft (~470 m) long and is a three-span bridge located along highway AS-17, Spain. The bridge main girder was built using a double composite section for the positive moment regions and a concrete box section for the negative moment regions (above the bridge supports). The maximum bridge span is 361 ft (~110 m), which is located in the middle of the bridge. The construction of the bridge was completed in 2007 (PAŃTAK 2012). Figure 2.15 shows a general view of the bridge during and after the construction.

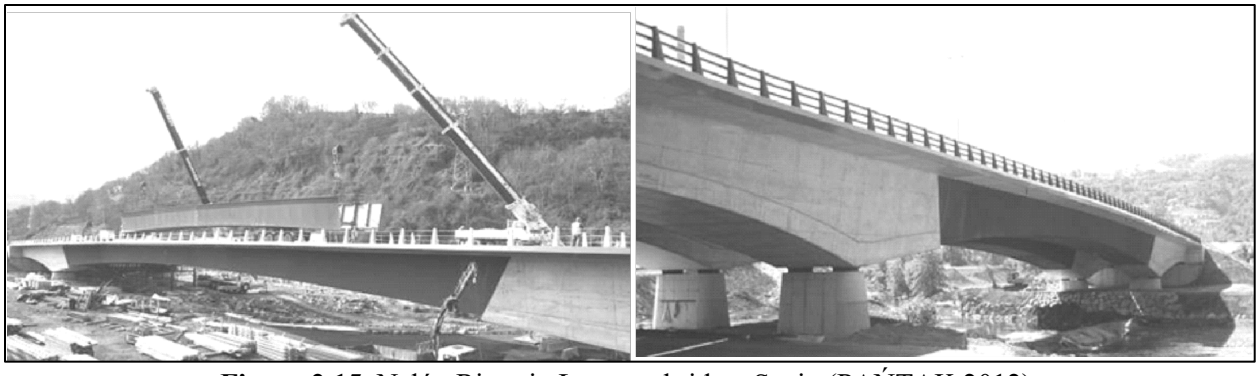

Figure 2.15 Nalón River in Langreo bridge, Spain (PAŃTAK 2012)

Bridge over the Sella River in Cangas de Onis, Spain: The bridge over the Sella River in Cangas de Onis is 378 ft (~115 m) long and 43 ft (~13.0 m) wide and is a three-span bridge. This bridge was opened in 2005. The bridge girder was built using a double composite section for the negative moment locations. The maximum bridge span is 262 ft (~80.0 m), which is located in the middle of the bridge. Figure 2.16 shows a general view of the bridge during and after construction.

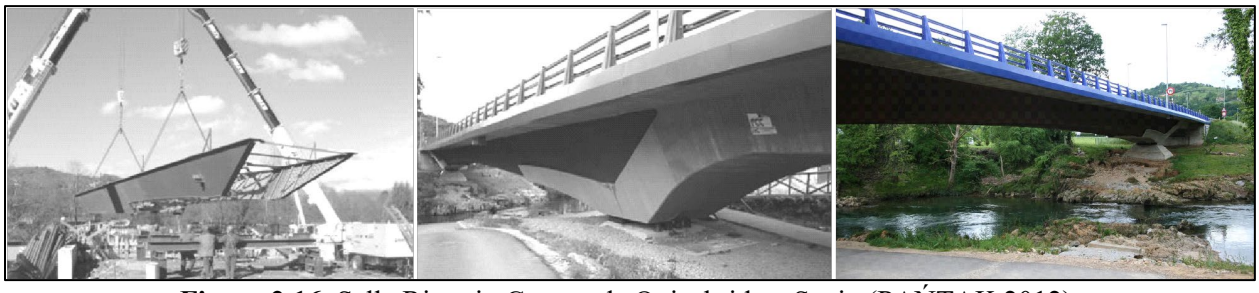

Figure 2.16 Sella River in Cangas de Onis, bridge, Spain (PAŃTAK 2012)

3. ANALYTICAL APPROACH

3.1 General

In this section, the analytical formulation developed and utilized to obtain the non-linear behavior of the double composite section, shown in Figure 3.1, is summarized. The analytical approach is used to obtain the behavior of a double composite section comprising a symmetric number of steel I-beams that are rigidly connected to one upper concrete slab and several bottom concrete slabs using shear connectors. The upper concrete slab is connected to the top faces of the upper flanges while the bottom concrete slabs are connected to the inner top faces of the lower flange. The composite section is subjected to positive bending moments as a straining action, implying that the bottom concrete slabs are located in the tension zone. The implication of these concrete slabs being located in tension zones are not fully effective in providing flexural resistance where only the slab longitudinal reinforcement can provide resistance to tensile stresses. The approach utilized to obtain the double composite behavior is based on the work presented by Charles Culver (1960), which was conducted only for single composite sections. The analytical formulation presented below was coded in MATLAB, and a graphical user interface (GUI) was built to aid in the analysis process. The GUI is shown in the results section of this report.

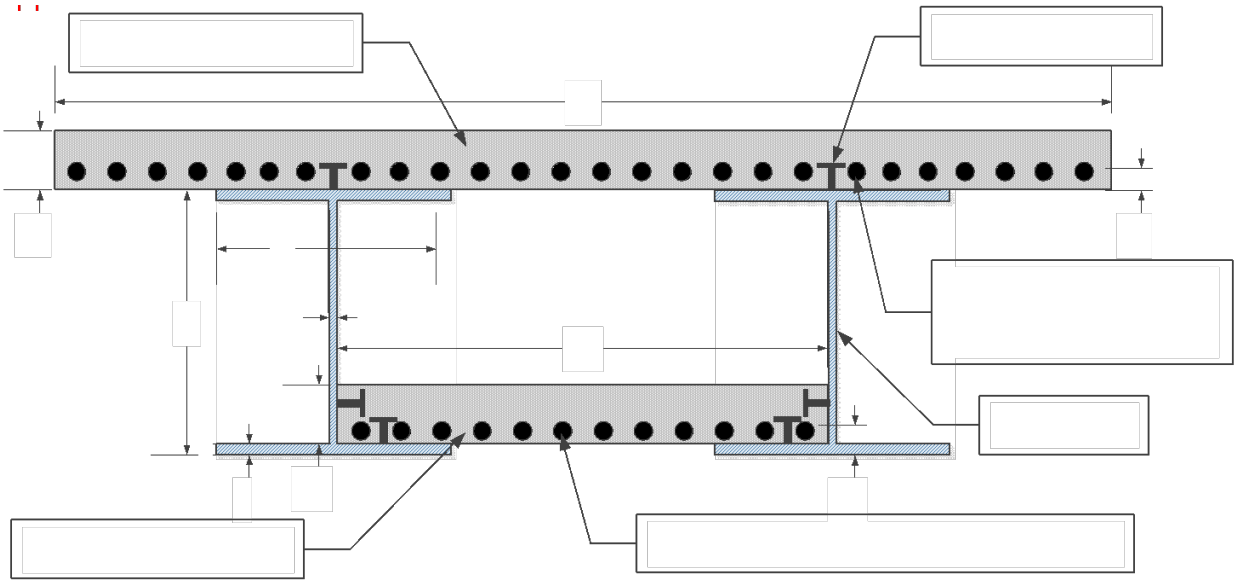

Figure 3.1 Double Composite Section General Components

3.2 Assumptions

To derive the behavior of the double composite beams analytically, some assumptions had to be made to simplify the developed equations. These assumptions include the following:

- The Bernoulli-Navier hypothesis, in which shear deformations are neglected, holds especially since this study is focused on hot rolled steel members that have limited depth.
- No slippage is allowed between the concrete slab and the steel beams. This assumption guarantees that full composite action is developed between the steel and concrete at all stress levels. To enforce this assumption in real bridge construction, proper design of shear connectors, in terms of the number of connectors and their placement, shall be provided.
- Elastic perfectly-plastic stress-strain relationships are assumed for both the steel and the concrete material as shown in Figure 3-2. The steel material behavior is assumed to be symmetric in tension and compression; however, the concrete is assumed to have no tensile resistance.

- The yield stress is the same for both the flanges and the webs of the steel beam regardless of their thickness. This is because the apparent yield stress for steel is reduced as the thickness increases.
- Only transverse loading is applied to the cross-section, and as such only in-plane deformations of the composite sections are considered.

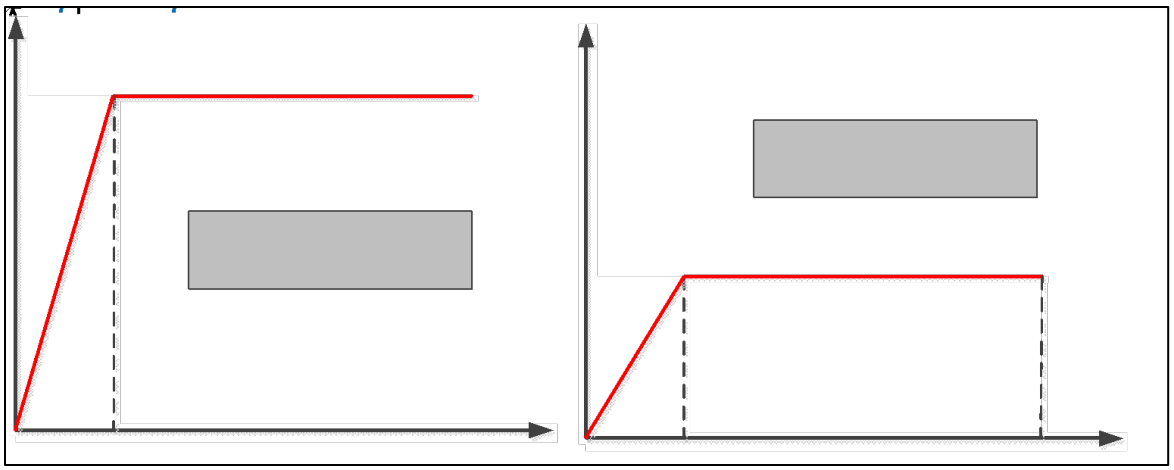

Figure 3.2 (a) Steel material behavior and (b) concrete material behavior

3.3 Method of the Solution – Double Composite Section Analysis

The method of analysis can be classified into elastic and plastic stages. In the elastic range, the tension failure of the bottom concrete slab shall be considered. Two different approaches of the analytical solution will be presented based on the behavior of the concrete slabs. The first approach assumes no resistance in the concrete slabs when tension stresses are applied. The second approach assumes that the steel rebars will work in tension even when the concrete fails in tension. The first part of the analysis is to define the cross-sectional elastic stresses and strains. By calculating the neutral axis location (Y) and the moment of inertia (I), in addition to defining the steel yield stress fy, the composite section elastic moment (M_y) can be predicted as $My = (fy * I) \ / \ Y$. Once the yield moment is calculated, the cross-sectional curvature at the yield point (K_y) can be calculated as $Ky = My \ / \ (Es * I)$.

Cross-Section subjected to a positive moment

The analysis in the plastic stage is based on the stress and strain distributions in addition to the equilibrium of forces. In the outlined formulation, 13 different stress distributions are assumed. Every stress distribution has a limit to its use, depending on the following parameters:

- The location of the neutral axis (α, μ)
- The steel plastic stress distribution (η)
- The concrete maximum stress distribution (ξ)

This section presents the analytical approach introduced to obtain the non-linear behavior of the double composite section with the bottom slab rebar contribution. The listed equations in this section consider only the double composite sections under a positive moment as a straining point. Therefore, the bottom concrete slab is always located in the tension zone (subjected to tensile stresses only) and the slab longitudinal reinforcement can develop tensile stresses. The implication of such is that the bottom reinforced concrete slab contributes to the overall flexural resistance and enhances the shear and torsional behavior of the composite section. As previously noted, 13 different stress distributions are assumed.

Those distributions cover most of the possible distributions for a single composite section. The 13 different stress distributions are listed below.

Stress Distribution One:

This distribution takes place when the neutral axis is located in the steel beam web, the steel lower flange is partially plastified, the stresses in the bottom slab reinforcements are less than the yield stress and the stress in the upper concrete slab is less than the maximum allowable stress, as shown in Figure 3.3.

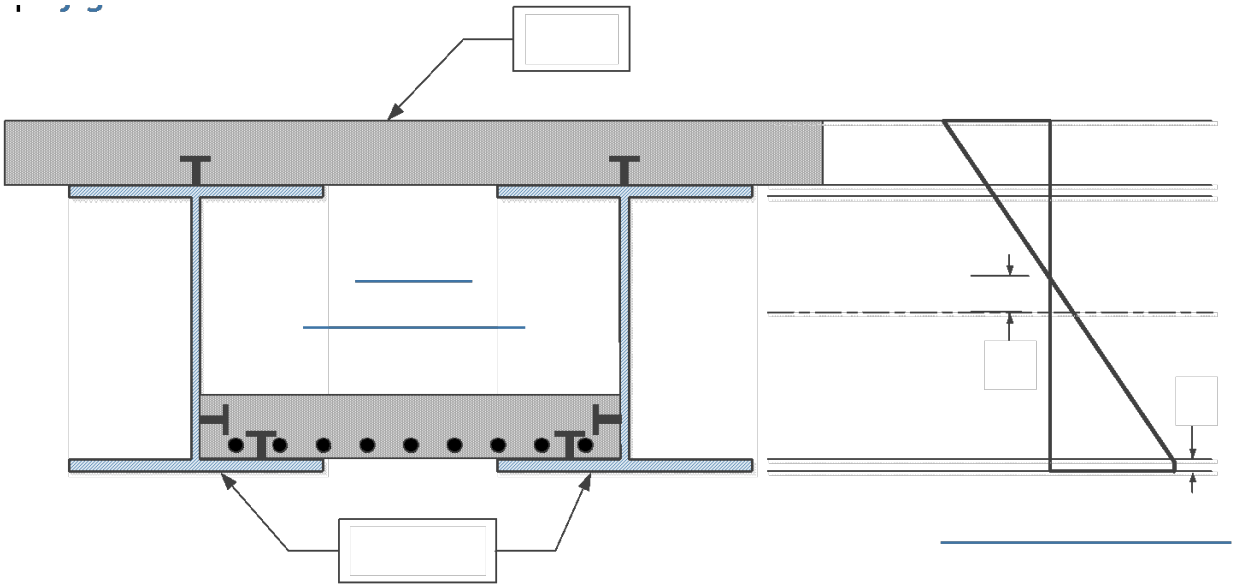

Figure 3.3 Stress distribution one

Stress distribution one can only be applicable if the following limits are satisfied:

- The neutral axis is located inside the steel beam webs.
- Only part of the lower steel flanges is plastified.
- The maximum stresses in the upper concrete do not exceed the concrete maximum stresses (f_c).

To analyze the cross-section with stress distribution one, the first step is to assume different values for the percent plastification in the steel lower flanges (η). Following the various assumptions of percent plastification, the following equation is solved to obtain the location of the neutral axis (α). All values of α shall fall in the previously mentioned range.

$$\frac{1}{2}*\left(fy*\frac{\frac{ds}{2}+dc_t-\alpha*ds}{\frac{ds}{2}+\alpha*ds-\eta*tf}-fy*\frac{\frac{ds}{2}-\alpha*ds}{\frac{ds}{2}+\alpha*ds-\eta*tf}\right)*\frac{bc_t}{n}*dc_t+\ fy*\frac{\frac{ds}{2}-\alpha*ds}{\frac{ds}{2}+\alpha*ds-\eta*tf}*\frac{bc_t}{n}*dc_t$$

$$+\ \ \frac{1}{2}*\left(fs*\frac{\frac{ds}{2}-\alpha*ds}{\frac{ds}{2}+\alpha*ds-\eta*tf}-fy*\frac{\frac{ds}{2}-\alpha*ds-tf}{\frac{ds}{2}+\alpha*ds-\eta*tf}\right)*b*tf\ +fy$$

$$*\frac{\frac{ds}{2}-\alpha*ds-tf}{\frac{ds}{2}+\alpha*ds-\eta*tf}*b*tf\ +\frac{1}{2}*fy*\frac{\frac{ds}{2}-\alpha*ds-tf}{\frac{ds}{2}+\alpha*ds-\eta*tf}*w*\left(\frac{ds}{2}-\alpha*ds-tf\right)-\frac{1}{2}$$

$$*fy*\frac{\frac{ds}{2}+\alpha*ds-tf}{\frac{ds}{2}+\alpha*ds-\eta*tf}*w*\left(\frac{ds}{2}+\alpha*ds-tf\right)-\ fy*\frac{\frac{ds}{2}+\alpha*ds-tf}{\frac{ds}{2}+\alpha*ds-\eta*tf}*b$$

$$*(tf-\eta*tf)-\frac{1}{2}*\left(fy-fy*\frac{\frac{ds}{2}+\alpha*ds-tf}{\frac{ds}{2}+\alpha*ds-\eta*tf}\right)*b*(tf-\eta*tf)-\ fy*b*\eta*tf$$

$$-\ fy*\frac{\frac{ds}{2}+\alpha*ds-dsb}{\frac{ds}{2}+\alpha*ds-\eta*tf}*\rho\ *\ bcb\ *\ dcb\ =\ 0$$

The maximum stresses in the upper concrete slab shall be calculated using the following equation for stress distribution one. The maximum stresses in the upper concrete slab shall not exceed the previously mentioned limits.

$$C\ =\frac{fy}{n}*\frac{\frac{ds}{2}+dc_t-\alpha*ds}{\frac{ds}{2}+\alpha*ds-e*tf}$$

Using the assumed values of η and α, the cross-sectional moment can be calculated as follows:

$$M = \frac{1}{2} * \left(fy * \frac{\frac{ds}{2} + dc_t - \alpha * ds}{\frac{ds}{2} + \alpha * ds - \eta * tf} - fy * \frac{\frac{ds}{2} - \alpha * ds}{\frac{ds}{2} + \alpha * ds - \eta * tf} \right) * \frac{bc_t}{n} * dc_t * \left(ds + \frac{2}{3} * dc_t \right) + fy$$

$$* \frac{\frac{ds}{2} - \alpha * ds}{\frac{ds}{2} + \alpha * ds - \eta * tf} * \frac{bc_t}{n} * dc_t * \left(ds + \frac{1}{2} * dc_t \right) + \frac{1}{2}$$

$$* \left(fy * \frac{\frac{ds}{2} - \alpha * ds}{\frac{ds}{2} + \alpha * ds - \eta * tf} - fy * \frac{\frac{ds}{2} - \alpha * ds - tf}{\frac{ds}{2} + \alpha * ds - \eta * tf} \right) * b * tf * \left(ds - \frac{1}{3} * tf \right) + fy$$

$$* \frac{\frac{ds}{2} - \alpha * ds - tf}{\frac{ds}{2} + \alpha * ds - \eta * tf} * b * tf * \left(ds - \frac{1}{2} * tf \right) + \frac{1}{2} * fy * \frac{\frac{ds}{2} - \alpha * ds - tf}{\frac{ds}{2} + \alpha * ds - \eta * tf} * w$$

$$* \left(\frac{ds}{2} - \alpha * ds - tf \right) * \left(\frac{ds}{2} + \alpha * ds + \frac{2}{3} * \left(\frac{ds}{2} - \alpha * ds - tf \right) \right) - \frac{1}{2} * fy$$

$$* \frac{\frac{ds}{2} + \alpha * ds - tf}{\frac{ds}{2} + \alpha * ds - \eta * tf} * w * \left(\frac{ds}{2} + \alpha * ds - tf \right) * \left(tf + \frac{1}{3} * \left(\frac{ds}{2} + \alpha * ds - tf \right) \right) - fy$$

$$* \frac{\frac{ds}{2} + \alpha * ds - tf}{\frac{ds}{2} + \alpha * ds - \eta * tf} * b * (tf - \eta * tf) * \left(\eta * tf + \frac{1}{2} * (tf - \eta * tf) \right) - \frac{1}{2}$$

$$* \left(fy - fy * \frac{\frac{ds}{2} + \alpha * ds - tf}{\frac{ds}{2} + \alpha * ds - \eta * tf} \right) * b * (tf - \eta * tf) * \left(\eta * tf + \frac{1}{3} * (tf - \eta * tf) \right) - fy * b$$

$$* \eta * tf * \left(\frac{1}{2} * \eta * tf \right) - fy * \frac{\frac{ds}{2} + \alpha * ds - dsb}{\frac{ds}{2} + \alpha * ds - \eta * tf} * \rho * bcb * dcb * dsb$$

Using the assumed values of η and α, the curvature of the cross-section can be calculated as follows:

$$K = 2 * \frac{\eta ys}{ds + 2 * \alpha * ds - 2 * \eta * tf}$$

Stress Distribution Two:

This distribution takes place when the neutral axis is located in the steel beam web, the steel web is partially plastified, the stress in the bottom slab reinforcement can be less or more than the yield stress based on the level of reinforcement, and the stress in the upper concrete slab is less than the maximum allowable stress, as shown in Figure 3.4.

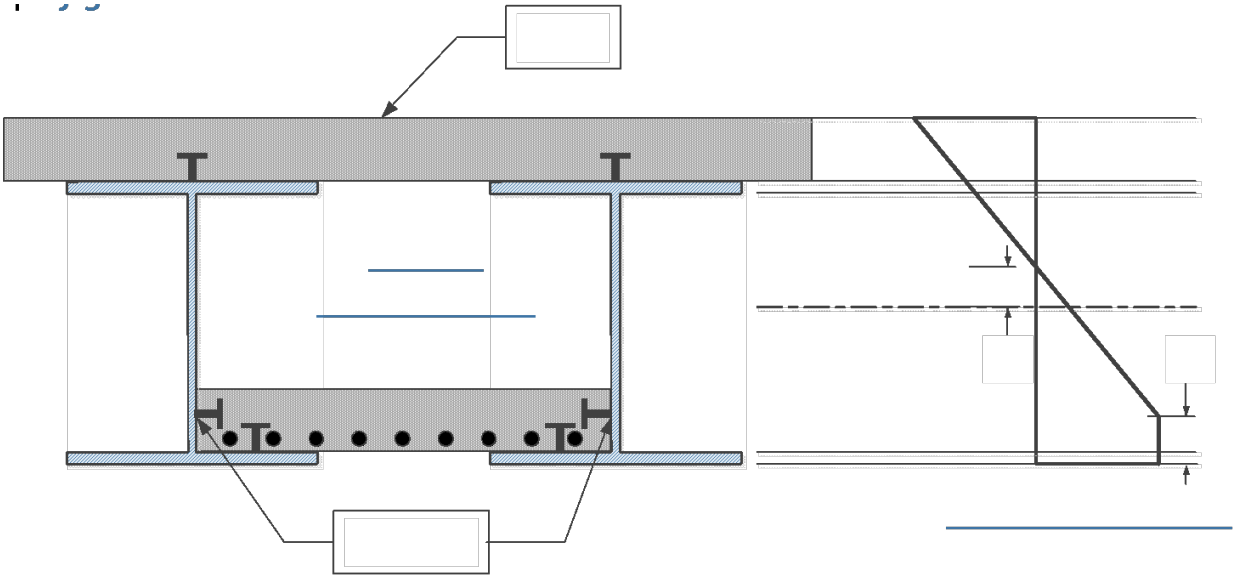

Figure 3.4 Stress distribution two

Stress distribution two can only be applicable if the following limits are satisfied:

- The neutral axis location is inside the steel beam webs.
- All lower steel flanges are plastified in addition to part of the steel webs.
- The maximum stresses in the upper concrete shall not exceed the concrete maximum stresses (f_c).

To analyze the cross-section with stress distribution two, the first step is to assume different values for percent plastification in the steel webs (η), and then solve the following equation to obtain the location of the neutral axis (α). All values of α shall fall in the previously mentioned range.

$$\frac{1}{2}*\left(fy*\frac{\frac{ds}{2}+dc_t-\alpha*ds}{\frac{ds}{2}+\alpha*ds-\eta*ds}-fy*\frac{\frac{ds}{2}-\alpha*ds}{\frac{ds}{2}+\alpha*ds-\eta*ds}\right)*\frac{bc_t}{n}*dc_t+\ fy*\frac{\frac{ds}{2}-\alpha*ds}{\frac{ds}{2}+\alpha*ds-\eta*ds}*\frac{bc_t}{n}*dc_t$$

$$+\frac{1}{2}*\left(fy*\frac{\frac{ds}{2}-\alpha*ds}{\frac{ds}{2}+\alpha*ds-\eta*ds}-fy*\frac{\frac{ds}{2}-\alpha*ds-tf}{\frac{ds}{2}+\alpha*ds-\eta*ds}\right)*b*tf\ +\ fy$$

$$*\frac{\frac{ds}{2}-\alpha*ds-tf}{\frac{ds}{2}+\alpha*ds-\eta*ds}*b*tf\ +\frac{1}{2}*fy*\frac{\frac{ds}{2}-\alpha*ds-tf}{\frac{ds}{2}+\alpha*ds-\eta*ds}*w*\left(\frac{ds}{2}-\alpha*ds-tf\right)-\frac{1}{2}$$

$$*fy*w*\left(\frac{ds}{2}+\alpha*ds-\eta*ds\right)-\ fy*w*(\eta*ds-tf)-\ fy*b*tf\ -\ f*\rho\ *\ bcb$$

$$*\ dcb\ =\ 0$$

The location of the neutral axis (α), distance from the edge of the bottom flange of the steel beam to the bottom slab reinforcements (d_{sb}), and percent of plastification in the steel web (η) are then used to calculate the stresses in the bottom slab reinforcements (f) as shown.

$$f = fy * \frac{\frac{ds}{2} + \alpha * ds - dsb}{\frac{ds}{2} + \alpha * ds - \eta * ds}$$

The maximum stresses in the upper concrete slab shall be calculated using the following equation for stress distribution two. The maximum stresses in the upper concrete slab shall not exceed the previously mentioned limits.

$$C = \frac{fy}{n} * \frac{dc_t + ds - \frac{ds}{2} - \alpha * ds}{\frac{ds}{2} + \alpha * ds - \eta * ds}$$

Using the assumed values of η and α, the cross-sectional moment can be calculated as follows:

$$\begin{aligned} M = {} & \frac{1}{2} * \left(fy * \frac{\frac{ds}{2} + dc_t - \alpha * ds}{\frac{ds}{2} + \alpha * ds - \eta * ds} - fy * \frac{\frac{ds}{2} - \alpha * ds}{\frac{ds}{2} + \alpha * ds - \eta * ds} \right) * \frac{bc_t}{n} * dc_t * \left(ds + \frac{2}{3} * dc_t \right) + fy \\ & * \frac{\frac{ds}{2} - \alpha * ds}{\frac{ds}{2} + \alpha * ds - \eta * ds} * \frac{bc_t}{n} * dc_t * \left(ds + \frac{1}{2} * dc_t \right) + \frac{1}{2} \\ & * \left(fy * \frac{\frac{ds}{2} - \alpha * ds}{\frac{ds}{2} + \alpha * ds - \eta * ds} - fy * \frac{\frac{ds}{2} - \alpha * ds - tf}{\frac{ds}{2} + \alpha * ds - \eta * ds} \right) * b * tf * \left(ds - \frac{1}{3} * tf \right) + fy \\ & * \frac{\frac{ds}{2} - \alpha * ds - tf}{\frac{ds}{2} + \alpha * ds - \eta * ds} * b * tf * \left(ds - \frac{1}{2} * tf \right) + \frac{1}{2} * fy * \frac{\frac{ds}{2} - \alpha * ds - tf}{\frac{ds}{2} + \alpha * ds - \eta * ds} * w \\ & * \left(\frac{ds}{2} - \alpha * ds - tf \right) * \left(\frac{ds}{2} + \alpha * ds + \frac{2}{3} * \left(\frac{ds}{2} - \alpha * ds - tf \right) \right) - \frac{1}{2} * fy * w \\ & * \left(\frac{ds}{2} + \alpha * ds - \eta * ds \right) * \left(\eta * ds + \frac{1}{3} * \left(\frac{ds}{2} + \alpha * ds - \eta * ds \right) \right) - fy * w * (\eta * ds - tf) \\ & * \left(tf + \frac{1}{2} * (\eta * ds - tf) \right) - fy * b * tf * \frac{1}{2} * tf - f * \rho * bcb * dcb * dsb \end{aligned}$$

Using the assumed values of η and α, the curvature of the cross-section can be calculated as follows:

$$K = 2 * \frac{eys}{ds + 2 * \alpha * ds - 2 * \eta * ds}$$

Stress Distribution Three:

This distribution takes place when the neutral axis is located in the steel beam web, the steel lower flange is partially plastified, the stress in the bottom slab reinforcements is less than the yield stresses, and the stress in the upper concrete slab reaches the maximum allowable stress, as shown in Figure 3.5.

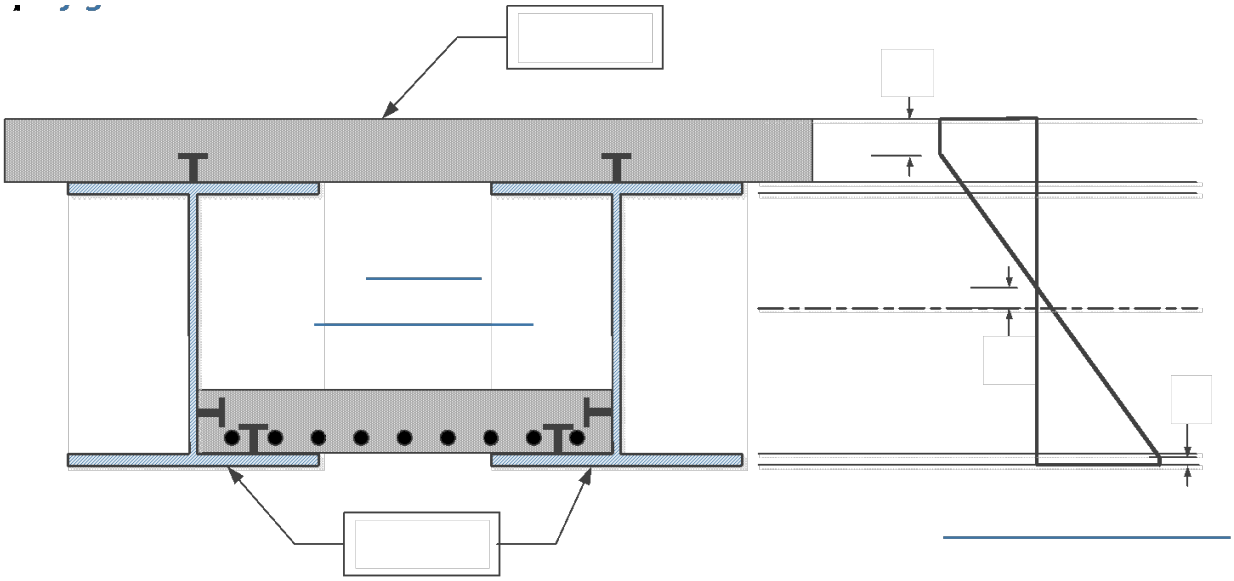

Figure 3.5 Stress distribution three

Stress distribution three can only be applicable if the following limits are satisfied:

- The neutral axis location is inside the steel beam webs.
- Only part of the lower steel flanges is plastified.
- The maximum stresses in the upper concrete exceed the concrete maximum stresses (f_c).

To analyze the cross-section with stress distribution three, the first step is to assume different values for the percent plastification in the steel webs (η), and then solve the following two equations to obtain the location of the neutral axis (α) and the percent plastification of the upper concrete slab (ξ). All values of α and ξ shall fall in the previously mentioned range.

$$fc/1000) * bc\_t * \xi * dc\_t + 0.5 * ((fc/1000) * n - fy * (0.5 - \alpha)/(0.5 - \eta * tf/ds + \alpha)) * bc\_t/n * (dc\_t - \xi * dc\_t) + fy * (0.5 - \alpha)/(0.5 - \eta * tf/ds + \alpha) * bc\_t/n * (dc\_t - \xi * dc\_t) + 0.5 * (fy * (0.5 - \alpha)/(0.5 - \eta * tf/ds + \alpha) - fy * (0.5 - \alpha - tf/ds)/(0.5 - \eta * tf/ds + \alpha)) * b * tf + fy * (0.5 - \alpha - tf/ds)/(0.5 - \eta * tf/ds + \alpha) * b * tf + 0.5 * fy * (0.5 - \alpha - tf/ds)/(0.5 - \eta * tf/ds + \alpha) * w * (ds/2 - \alpha * ds - tf) - 1/2 * fy * (0.5 + \alpha - tf/ds)/(0.5 - \eta * tf/ds + \alpha) * w * (ds/2 + \alpha * ds - tf) - fy * (0.5 + \alpha - tf/ds)/(0.5 - \eta * tf/ds + \alpha) * b * (tf - \eta * tf) - 1/2 * (fy - fy * (0.5 + \alpha - tf/ds)/(0.5 - \eta * tf/ds + \alpha)) * b * (tf - \eta * tf) - fy * \eta * tf * b - fy * (0.5 + \alpha - dsb/ds)/(0.5 - \eta * tf/ds + \alpha) * \rho * bcb * dcb = 0$$

$$\left(\frac{fc}{1000}\right) * n * \left(\frac{ds}{2} - \eta * tf + \alpha * ds\right) = fy * \left(\frac{ds}{2} - \alpha * ds + dc_t - \xi * dc_t\right)$$

Using the assumed values of η and the calculated values of α and ξ, the cross-sectional moment can be calculated as follows:

$$M = \left(\frac{fc}{1000}\right) * bc_t * \xi * dc_t * \left(ds + dc_t - \xi * \frac{dc_t}{2}\right) + 0.5 * \left(\left(\frac{fc}{1000}\right) * n - fy * \frac{0.5 - \alpha}{0.5 - \eta * \frac{tf}{ds} + \alpha}\right) * \frac{bc_t}{n}$$
$$* (dc_t - \xi * dc_t) * \left(ds + \frac{2}{3} * dc_t * (1 - \xi)\right) + fy * \frac{0.5 - \alpha}{0.5 - \eta * \frac{tf}{ds} + \alpha} * \frac{bc_t}{n} * (dc_t - \xi * dc_t)$$
$$* \left(ds + \frac{1}{2} * dc_t * (1 - \xi)\right) + 0.5 * \left(fy * \frac{0.5 - \alpha}{0.5 - \eta * \frac{tf}{ds} + \alpha} - fy * \frac{0.5 - \alpha - \frac{tf}{ds}}{0.5 - \eta * \frac{tf}{ds} + \alpha}\right) * b * tf$$
$$* \left(ds - \frac{1}{3} * tf\right) + fy * \frac{0.5 - \alpha - \frac{tf}{ds}}{0.5 - \eta * \frac{tf}{ds} + \alpha} * b * tf * \left(ds - \frac{1}{2} * tf\right) + 0.5 * fy * \frac{0.5 - \alpha - \frac{tf}{ds}}{0.5 - \eta * \frac{tf}{ds} + \alpha}$$
$$* w * \left(\frac{ds}{2} - \alpha * ds - tf\right) * \left(ds - tf - \frac{1}{3} * \left(\frac{ds}{2} - \alpha * ds - tf\right)\right) - \frac{1}{2} * fy * \frac{0.5 + \alpha - \frac{tf}{ds}}{0.5 - \eta * \frac{tf}{ds} + \alpha}$$
$$* w * \left(\frac{ds}{2} + \alpha * ds - tf\right) * \left(tf + \frac{1}{3} * \left(\frac{ds}{2} + \alpha * ds - tf\right)\right) - fy * \frac{0.5 + \alpha - \frac{tf}{ds}}{0.5 - \eta * \frac{tf}{ds} + \alpha} * b$$
$$* (tf - \eta * tf) * \left(\eta * tf + \frac{1}{2} * (tf - \eta * tf)\right) - \frac{1}{2} * \left(fy - fy * \frac{0.5 + \alpha - \frac{tf}{ds}}{0.5 - \eta * \frac{tf}{ds} + \alpha}\right) * b$$
$$* (tf - \eta * tf) * \left(\eta * tf + \frac{1}{3} * (tf - \eta * tf)\right) - fy * \eta * tf * b * \left(\frac{1}{2} * \eta * tf\right) - fy$$
$$* \frac{0.5 + \alpha - \frac{dsb}{ds}}{0.5 - \eta * \frac{tf}{ds} + \alpha} * \rho * bcb * dcb * dsb$$

Using the assumed values of η and the calculated values of α and ξ, the curvature of the cross-section can be calculated as follows:

$$K = 2 * \frac{eys}{ds + 2 * \alpha * ds - 2 * \eta * tf}$$

Stress Distribution Four:

This distribution takes place when the neutral axis is located in the steel beam web, the steel web is partially plastified, the stress in the bottom slab reinforcements can be less or more than the yield stress based on the level of the reinforcement, and the stress in the upper concrete slab reaches the maximum allowable stress, as shown in Figure 3.6.

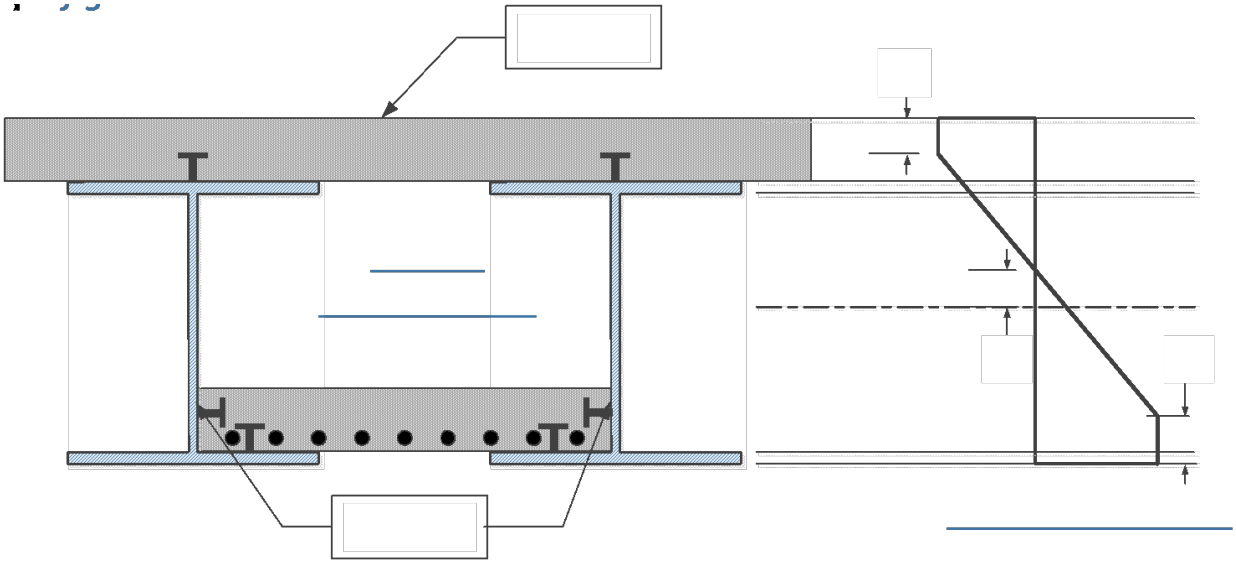

Figure 3.6 Stress distribution four

Stress distribution four can only be applicable if the following limits are satisfied:

- The neutral axis location is inside the steel beam webs.
- All lower steel flanges are plastified in addition to part of the steel webs.
- The maximum stresses in the upper concrete shall be exceeded by the concrete maximum stresses (f_c).

To analyze the cross-section with stress distribution four, the first step is to assume different values for the percent plastification in the steel webs (η), then solve the following two equations to obtain the location of the neutral axis (α) and the percent plastification of the upper concrete slab (ξ). All values of α and ξ shall fall in the previously mentioned range.

$$\frac{1}{2}*\left(fy*\frac{\frac{ds}{2}+dc_t-\alpha*ds}{\frac{ds}{2}+\alpha*ds-\eta*ds}-fy*\frac{\frac{ds}{2}-\alpha*ds}{\frac{ds}{2}+\alpha*ds-\eta*ds}\right)*\frac{bc_t}{n}*dc_t+\ fy*\frac{\frac{ds}{2}-\alpha*ds}{\frac{ds}{2}+\alpha*ds-\eta*ds}*\frac{bc_t}{n}*dc_t$$

$$+\frac{1}{2}*fy*\frac{\frac{ds}{2}-\alpha*ds}{\frac{ds}{2}+\alpha*ds-\eta*ds}*b*\left(\frac{ds}{2}-\alpha*ds\right)-\frac{1}{2}*fy*\frac{tf-\frac{ds}{2}+\alpha*ds}{\frac{ds}{2}+\alpha*ds-\eta*ds}*b$$

$$*\left(tf-\frac{ds}{2}+\alpha*ds\right)-\ fy*\frac{tf-\frac{ds}{2}+\alpha*ds}{\frac{ds}{2}+\alpha*ds-\eta*ds}*w*(ds-tf-\eta*ds)-\frac{1}{2}$$

$$*\left(fy-fy*\frac{tf-\frac{ds}{2}+\alpha*ds}{\frac{ds}{2}+\alpha*ds-\eta*ds}\right)*w*(ds-tf-\eta*ds)-\ fy*w*(\eta*ds-tf)-\ fy$$

$$*b*tf\ -\ f*\rho\ *\ bcb\ *\ dcb\ =\ 0$$

The location of the neutral axis (α), distance from the edge of the bottom flange of the steel beam to the bottom slab reinforcements (d_{sb}), and percent of plastification in the steel web (η) are then used to calculate the stresses in the bottom slab reinforcements (f) as shown.

$$f\ =\ fy*\frac{\frac{ds}{2}+\alpha*ds-dsb}{\frac{ds}{2}+\alpha*ds-\eta*ds}$$

Using the assumed values of η and the calculated values of α and ξ, the cross-sectional moment can be calculated as follows:

$$M = \frac{1}{2} * \left(fy * \frac{\frac{ds}{2} + dc_t - \alpha * ds}{\frac{ds}{2} + \alpha * ds - \eta * ds} - fy * \frac{\frac{ds}{2} - \alpha * ds}{\frac{ds}{2} + \alpha * ds - \eta * ds} \right) * \frac{bc_t}{n} * dc_t * \left(ds + \frac{2}{3} * dc_t \right) + fy$$

$$* \frac{\frac{ds}{2} - \alpha * ds}{\frac{ds}{2} + \alpha * ds - \eta * ds} * \frac{bc_t}{n} * dc_t * \left(ds + \frac{1}{2} * dc_t \right) + \frac{1}{2} * fy * \frac{\frac{ds}{2} - \alpha * ds}{\frac{ds}{2} + \alpha * ds - \eta * ds} * b$$

$$* \left(\frac{ds}{2} - \alpha * ds \right) * \left(ds - \frac{1}{3} * \left(\frac{ds}{2} - \alpha * ds \right) \right) - \frac{1}{2} * fy * \frac{tf - \frac{ds}{2} + \alpha * ds}{\frac{ds}{2} + \alpha * ds - \eta * ds} * b$$

$$* \left(tf - \frac{ds}{2} + \alpha * ds \right) * \left(ds - tf + \frac{1}{3} * \left(tf - \frac{ds}{2} + \alpha * ds \right) \right) - fy * \frac{tf - \frac{ds}{2} + \alpha * ds}{\frac{ds}{2} + \alpha * ds - \eta * ds} * w$$

$$* (ds - tf - \eta * ds) * \left(\eta * ds + \frac{1}{2} * (ds - tf - \eta * ds) \right) - \frac{1}{2}$$

$$* \left(fy - fy * \frac{tf - \frac{ds}{2} + \alpha * ds}{\frac{ds}{2} + \alpha * ds - \eta * ds} \right) * w * (ds - tf - \eta * ds)$$

$$* \left(\eta * ds + \frac{1}{3} * (ds - tf - \eta * ds) \right) - fy * w * (\eta * ds - tf) * \left(tf + \frac{1}{2} * (\eta * ds - tf) \right) - fy$$

$$* b * tf * \left(\frac{tf}{2} \right) - f * \rho * bcb * dcb * dsb$$

Using the assumed values of η and the calculated values of α and ξ, the curvature of the cross-section can be calculated as follows:

$$K = 2 * \frac{eys}{ds + 2 * \alpha * ds - 2 * \eta * ds}$$

Stress Distribution Five:

This distribution takes place when the neutral axis is located in the steel beam upper flange, the steel lower flange is partially plastified, the stresses in the bottom slab reinforcements are less than the yield stresses, and the stress in the upper concrete slab is less than the maximum allowable stress, as shown in Figure 3.7.

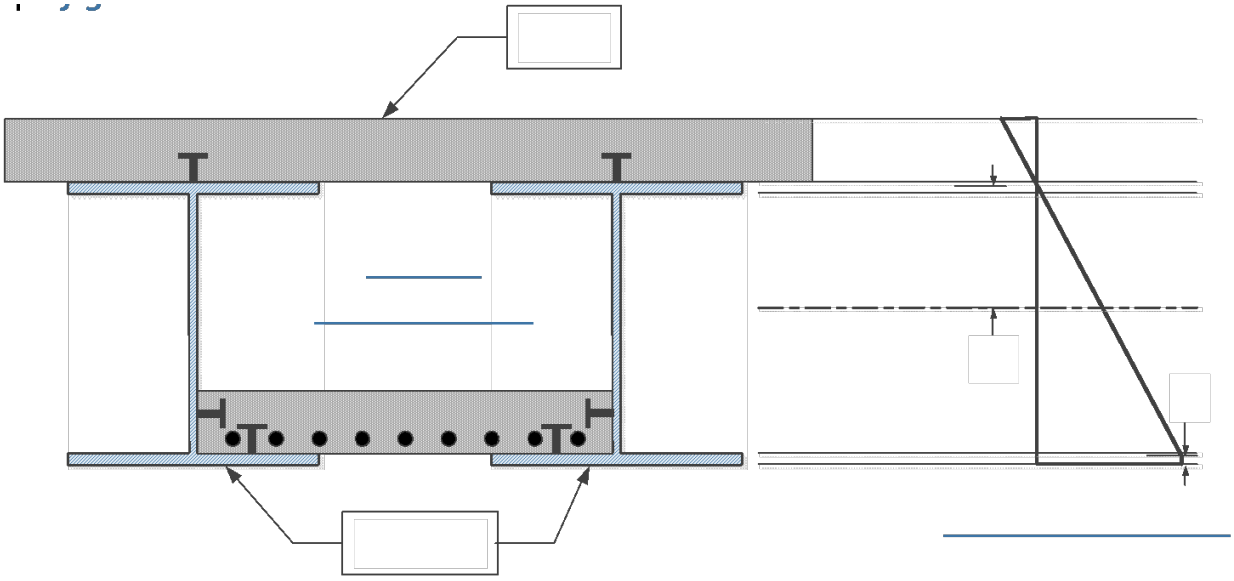

Figure 3.7 Stress distribution five

Stress distribution five can only be applicable if the following limits are satisfied:

- The neutral axis location is inside the steel beam upper flanges.
- Only part of the lower steel flanges is plastified.
- The maximum stresses in the upper concrete shall not exceed the concrete maximum stresses (f_c).

To analyze the cross-section with stress distribution five, the first step is to assume different values for the percent plastification in the steel lower flanges (η), then solve the following equation to obtain the location of the neutral axis (α). All values of α shall fall in the previously mentioned range.

$$\frac{1}{2}*\left(fy*\frac{\frac{ds}{2}+dc_t-\alpha*ds}{\frac{ds}{2}+\alpha*ds-\eta*tf}-fy*\frac{\frac{ds}{2}-\alpha*ds}{\frac{ds}{2}+\alpha*ds-\eta*tf}\right)*\frac{bc_t}{n}*dc_t+\ fy*\frac{\frac{ds}{2}-\alpha*ds}{\frac{ds}{2}+\alpha*ds-\eta*tf}*\frac{bc_t}{n}*dc_t$$

$$+\frac{1}{2}*fy*\frac{\frac{ds}{2}-\alpha*ds}{\frac{ds}{2}+\alpha*ds-\eta*tf}*b*\left(\frac{ds}{2}-\alpha*ds\right)-\frac{1}{2}*fy*\frac{tf-\frac{ds}{2}+\alpha*ds}{\frac{ds}{2}+\alpha*ds-\eta*tf}*b$$

$$*\left(tf-\frac{ds}{2}+\alpha*ds\right)-\ fy*\frac{tf-\frac{ds}{2}+\alpha*ds}{\frac{ds}{2}+\alpha*ds-\eta*tf}*w*(ds-2*tf)-\frac{1}{2}$$

$$*\left(fy*\frac{\frac{ds}{2}+\alpha*ds-tf}{\frac{ds}{2}+\alpha*ds-\eta*tf}-fy*\frac{tf-\frac{ds}{2}+\alpha*ds}{\frac{ds}{2}+\alpha*ds-\eta*tf}\right)*w*(ds-2*tf)-\ fy$$

$$*\frac{\frac{ds}{2}+\alpha*ds-tf}{\frac{ds}{2}+\alpha*ds-\eta*tf}*b*(tf-\eta*tf)-\frac{1}{2}*\left(fy-fy*\frac{\frac{ds}{2}+\alpha*ds-tf}{\frac{ds}{2}+\alpha*ds-\eta*tf}\right)*b$$

$$*(tf-\eta*tf)-\ fy*b*\eta*tf\ -\ fy*\frac{\frac{ds}{2}+\alpha*ds-dsb}{\frac{ds}{2}+\alpha*ds-\eta*tf}*\rho\ *\ bcb\ *\ dcb\ =\ 0$$

The maximum stresses in the upper concrete slab shall be calculated using the following equation for stress distribution five. The maximum stresses in the upper concrete slab shall not exceed the previously mentioned limits.

$$C\ =\frac{fy}{n}*\frac{\frac{ds}{2}+dc_t-\alpha*ds}{\frac{ds}{2}+\alpha*ds-\eta*tf}$$

Using the assumed values of η and α, the cross-sectional moment can be calculated as follows:

$$M = \frac{1}{2} * \left(fy * \frac{\frac{ds}{2} + dc_t - \alpha * ds}{\frac{ds}{2} + \alpha * ds - \eta * tf} - fy * \frac{\frac{ds}{2} - \alpha * ds}{\frac{ds}{2} + \alpha * ds - \eta * tf} \right) * \frac{bc_t}{n} * dc_t * \left(ds + \frac{2}{3} * dc_t \right) + fy$$

$$* \frac{\frac{ds}{2} - \alpha * ds}{\frac{ds}{2} + \alpha * ds - \eta * tf} * \frac{bc_t}{n} * dc_t * \left(ds + \frac{1}{2} * dc_t \right) + \frac{1}{2} * fy * \frac{\frac{ds}{2} - \alpha * ds}{\frac{ds}{2} + \alpha * ds - \eta * tf} * b$$

$$* \left(\frac{ds}{2} - \alpha * ds \right) * \left(ds - \frac{1}{3} * \left(\frac{ds}{2} - \alpha * ds \right) \right) - \frac{1}{2} * fy * \frac{tf - \frac{ds}{2} + \alpha * ds}{\frac{ds}{2} + \alpha * ds - \eta * tf} * b$$

$$* \left(tf - \frac{ds}{2} + \alpha * ds \right) * \left(ds - tf + \frac{1}{3} * \left(tf - \frac{ds}{2} + \alpha * ds \right) \right) - fy * \frac{tf - \frac{ds}{2} + \alpha * ds}{\frac{ds}{2} + \alpha * ds - \eta * tf} * w$$

$$* (ds - 2 * tf) * \left(tf + \frac{1}{2} * (ds - 2 * tf) \right) - \frac{1}{2}$$

$$* \left(fy * \frac{\frac{ds}{2} + \alpha * ds - tf}{\frac{ds}{2} + \alpha * ds - \eta * tf} - fy * \frac{tf - \frac{ds}{2} + \alpha * ds}{\frac{ds}{2} + \alpha * ds - \eta * tf} \right) * w * (ds - 2 * tf)$$

$$* \left(tf + \frac{1}{3} * (ds - 2 * tf) \right) - fy * \frac{\frac{ds}{2} + \alpha * ds - tf}{\frac{ds}{2} + \alpha * ds - \eta * tf} * b * (tf - \eta * tf)$$

$$* \left(\eta * tf + \frac{1}{2} * (tf - \eta * tf) \right) - \frac{1}{2} * \left(fy - fy * \frac{\frac{ds}{2} + \alpha * ds - tf}{\frac{ds}{2} + \alpha * ds - \eta * tf} \right) * b * (tf - \eta * tf)$$

$$* \left(\eta * tf + \frac{1}{3} * (tf - \eta * tf) \right) - fy * b * \eta * tf * \frac{1}{2} * \eta * tf - fy * \frac{\frac{ds}{2} + \alpha * ds - dsb}{\frac{ds}{2} + \alpha * ds - \eta * tf} * \rho$$

$$* bcb * dcb * dsb$$

Using the assumed values of η and α, the curvature of the cross-section can be calculated as follows:

$$K = 2 * \frac{eys}{ds + 2 * \alpha * ds - 2 * \eta * tf}$$

Stress Distribution Six:

This distribution takes place when the neutral axis is located in the steel beam upper flange, the steel web is partially plastified, the stresses in the bottom slab reinforcements can be less or more than the yield stress based on the level of the reinforcement, and the stress in the upper concrete slab is less than the maximum allowable stress, as shown in Figure 3.8.

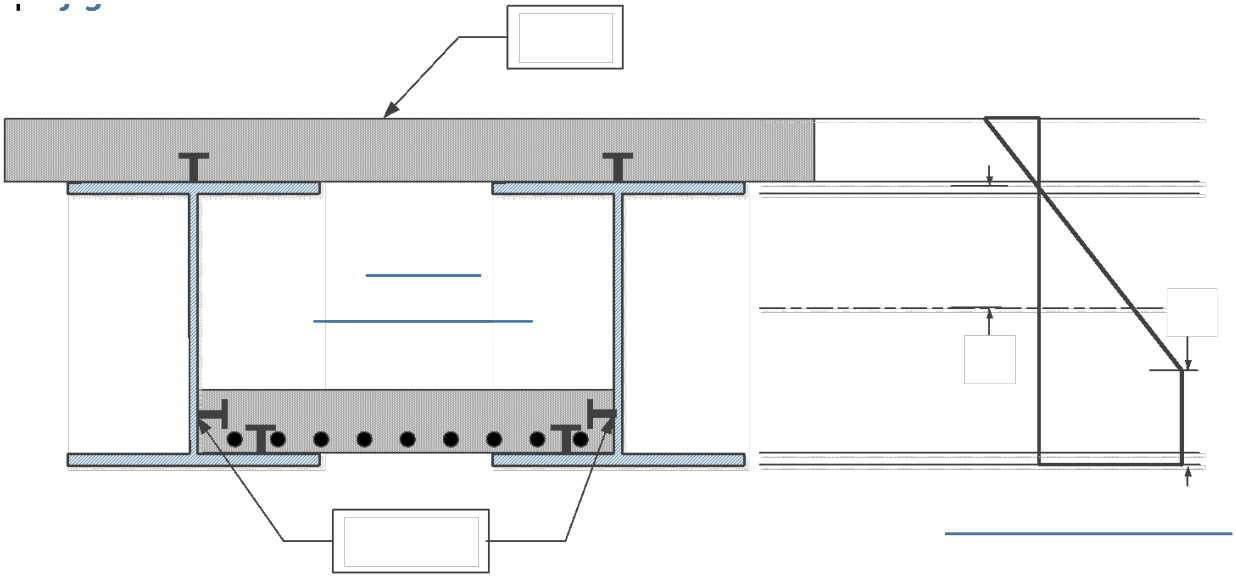

Figure 3.8 Stress distribution six

Stress distribution six can only be applicable if the following limits are satisfied:

- The neutral axis location is inside the steel beam upper flanges.
- All the lower steel flanges are plastified in addition to part of the steel webs.
- The maximum stresses in the upper concrete shall not exceed the concrete maximum stresses (f_c).

To analyze the cross-section with stress distribution six, the first step is to assume different values for the percent plastification in the steel webs (η) then solve the following equation to obtain the location of the neutral axis (α). All values of α shall fall in the previously mentioned range.

$$\frac{1}{2}*\left(fy*\frac{\frac{ds}{2}+dc_t-\alpha*ds}{\frac{ds}{2}+\alpha*ds-\eta*ds}-fy*\frac{\frac{ds}{2}-\alpha*ds}{\frac{ds}{2}+\alpha*ds-\eta*ds}\right)*\frac{bc_t}{n}*dc_t+\ fy*\frac{\frac{ds}{2}-\alpha*ds}{\frac{ds}{2}+\alpha*ds-\eta*ds}*\frac{bc_t}{n}*dc_t$$

$$+\frac{1}{2}*fy*\frac{\frac{ds}{2}-\alpha*ds}{\frac{ds}{2}+\alpha*ds-\eta*ds}*b*\left(\frac{ds}{2}-\alpha*ds\right)-\frac{1}{2}*fy*\frac{tf-\frac{ds}{2}+\alpha*ds}{\frac{ds}{2}+\alpha*ds-\eta*ds}*b$$

$$*\left(tf-\frac{ds}{2}+\alpha*ds\right)-\ fy*\frac{tf-\frac{ds}{2}+\alpha*ds}{\frac{ds}{2}+\alpha*ds-\eta*ds}*w*(ds-tf-\eta*ds)-\frac{1}{2}$$

$$*\left(fy-fy*\frac{tf-\frac{ds}{2}+\alpha*ds}{\frac{ds}{2}+\alpha*ds-\eta*ds}\right)*w*(ds-tf-\eta*ds)-\ fy*w*(\eta*ds-tf)-\ fy$$

$$*b*tf\ -\ f*\rho\ *\ bcb\ *\ dcb\ =\ 0$$

The location of the neutral axis (α), distance from the edge of the bottom flange of the steel beam to the bottom slab reinforcements (d_{sb}), and percent of plastification in the steel web (η) are then used to calculate the stresses in the bottom slab reinforcements (f) as shown.

$$f = fy * \frac{\frac{ds}{2} + \alpha * ds - dsb}{\frac{ds}{2} + \alpha * ds - \eta * ds}$$

The maximum stresses in the upper concrete slab shall be calculated using the following equation for stress distribution six. The maximum stresses in the upper concrete slab shall not exceed the previously mentioned limits.

$$C = \frac{fy}{n} * \frac{\frac{ds}{2} + dc_t - \alpha * ds}{\frac{ds}{2} + \alpha * ds - \eta * ds}$$

Using the assumed values of η and α, the cross-sectional moment can be calculated as follows:

$$\begin{aligned} M = {} & \frac{1}{2} * \left(fy * \frac{\frac{ds}{2} + dc_t - \alpha * ds}{\frac{ds}{2} + \alpha * ds - \eta * ds} - fy * \frac{\frac{ds}{2} - \alpha * ds}{\frac{ds}{2} + \alpha * ds - \eta * ds} \right) * \frac{bc_t}{n} * dc_t * \left(ds + \frac{2}{3} * dc_t \right) + fy \\ & * \frac{\frac{ds}{2} - \alpha * ds}{\frac{ds}{2} + \alpha * ds - \eta * ds} * \frac{bc_t}{n} * dc_t * \left(ds + \frac{1}{2} * dc_t \right) + \frac{1}{2} * fy * \frac{\frac{ds}{2} - \alpha * ds}{\frac{ds}{2} + \alpha * ds - \eta * ds} * b \\ & * \left(\frac{ds}{2} - \alpha * ds \right) * \left(ds - \frac{1}{3} * \left(\frac{ds}{2} - \alpha * ds \right) \right) - \frac{1}{2} * fy * \frac{tf - \frac{ds}{2} + \alpha * ds}{\frac{ds}{2} + \alpha * ds - \eta * ds} * b \\ & * \left(tf - \frac{ds}{2} + \alpha * ds \right) * \left(ds - tf + \frac{1}{3} * \left(tf - \frac{ds}{2} + \alpha * ds \right) \right) - fy * \frac{tf - \frac{ds}{2} + \alpha * ds}{\frac{ds}{2} + \alpha * ds - \eta * ds} * w \\ & * (ds - tf - \eta * ds) * \left(\eta * ds + \frac{1}{2} * (ds - tf - \eta * ds) \right) - \frac{1}{2} \\ & * \left(fy - fy * \frac{tf - \frac{ds}{2} + \alpha * ds}{\frac{ds}{2} + \alpha * ds - \eta * ds} \right) * w * (ds - tf - \eta * ds) \\ & * \left(\eta * ds + \frac{1}{3} * (ds - tf - \eta * ds) \right) - fy * w * (\eta * ds - tf) * \left(tf + \frac{1}{2} * (\eta * ds - tf) \right) - fy \\ & * b * tf * \left(\frac{tf}{2} \right) - f * \rho * bcb * dcb * dsb \end{aligned}$$

Using the assumed values of η and α, the curvature of the cross-section can be calculated as follows:

$$K = 2 * \frac{eys}{ds + 2 * \alpha * ds - 2 * \eta * ds}$$

Stress Distribution Seven:

This distribution takes place when the neutral axis is located in the steel beam upper flange, the steel lower flange is partially plastified, the stresses in the bottom slab reinforcements are less than the yield stresses, and the stress in the upper concrete slab reaches the maximum allowable stress, as shown in Figure 3.9.

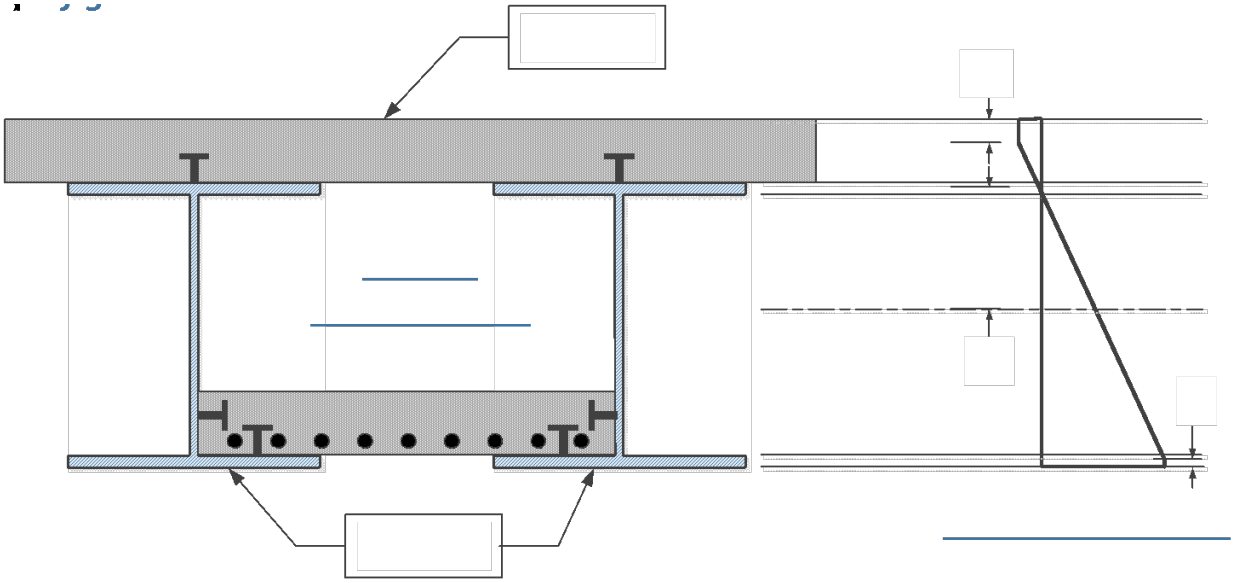

Figure 3.9 Stress distribution seven

Stress distribution seven can only be applicable if the following limits are satisfied:

- The neutral axis location is inside the steel beam upper flanges.
- Only part of the lower steel flanges is plastified.
- The maximum stresses in the upper concrete shall exceed the concrete maximum stresses (f_c).

To analyze the cross-section with stress distribution seven, the first step is to assume different values for the percent plastification in the steel webs (η), then solve the following two equations to obtain the location of the neutral axis (α) and the percent plastification of the upper concrete slab (ξ). All values of α and ξ shall fall in the previously mentioned range.

$$\left(\frac{fc}{1000}\right) * bc_t * \xi * dc_t + 0.5 * \left(\left(\frac{fc}{1000}\right) * n - fy * \frac{0.5-\alpha}{0.5-\eta * \frac{tf}{ds}+\alpha}\right) * \frac{bc_t}{n} * (dc_t - \xi * dc_t) + fy$$

$$* \frac{0.5-\alpha}{0.5-\eta * \frac{tf}{ds}+\alpha} * \frac{bc_t}{n} * (dc_t - \xi * dc_t) + 0.5 * fy * \frac{0.5-\alpha}{0.5-\eta * \frac{tf}{ds}+\alpha} * b * \left(\frac{ds}{2} - \alpha * ds\right)$$

$$-\frac{1}{2} * fy * \frac{tf - \frac{ds}{2} + \alpha * ds}{\frac{ds}{2} + \alpha * ds - \eta * tf} * b * \left(tf - \frac{ds}{2} + \alpha * ds\right) - fy * \frac{tf - \frac{ds}{2} + \alpha * ds}{\frac{ds}{2} + \alpha * ds - \eta * tf} * w$$

$$* (ds - 2 * tf) - \frac{1}{2} * \left(fy * \frac{\frac{ds}{2} + \alpha * ds - tf}{\frac{ds}{2} + \alpha * ds - \eta * tf} - fy * \frac{tf - \frac{ds}{2} + \alpha * ds}{\frac{ds}{2} + \alpha * ds - \eta * tf}\right) * w$$

$$* (ds - 2 * tf) - fy * \frac{\frac{ds}{2} + \alpha * ds - tf}{\frac{ds}{2} + \alpha * ds - \eta * tf} * b * (tf - \eta * tf) - \frac{1}{2}$$

$$* \left(fy - fy * \frac{\frac{ds}{2} + \alpha * ds - tf}{\frac{ds}{2} + \alpha * ds - \eta * tf}\right) * b * (tf - \eta * tf) - fy * b * \eta * tf - fy$$

$$* \frac{\frac{ds}{2} + \alpha * ds - dsb}{\frac{ds}{2} + \alpha * ds - \eta * tf} * \rho * bcb * dcb = 0$$

$$\left(\frac{fc}{1000}\right) * n * \left(\frac{ds}{2} - \eta * tf + alfa * ds\right) = fy * \left(\frac{ds}{2} - alfa * ds + dc_t - \xi * dc_t\right)$$

Using the assumed values of η and the calculated values of α and ξ, the cross-sectional moment can be calculated as follows:

$$M = \left(\frac{fc}{1000}\right) * bc_t * \xi * dc_t * \left(ds + dc_t - \xi * \frac{dc_t}{2}\right) + 0.5 * \left(\left(\frac{fc}{1000}\right) * n - fy * \frac{0.5 - \alpha}{0.5 - \eta * \frac{tf}{ds} + \alpha}\right) * \frac{bc_t}{n}$$

$$* (dc_t - \xi * dc_t) * \left(ds + \frac{2}{3} * dc_t * (1 - \xi)\right) + fy * \frac{0.5 - \alpha}{0.5 - \eta * \frac{tf}{ds} + \alpha} * \frac{bc_t}{n} * (dc_t - \xi * dc_t)$$

$$* \left(ds + \frac{1}{2} * dc_t * (1 - \xi)\right) + 0.5 * fy * \frac{0.5 - \alpha}{0.5 - \eta * \frac{tf}{ds} + \alpha} * b * \left(\frac{ds}{2} - \alpha * ds\right)$$

$$* \left(ds - \frac{1}{3} * \left(\frac{ds}{2} - \alpha * ds\right)\right) - \frac{1}{2} * fy * \frac{tf - \frac{ds}{2} + \alpha * ds}{\frac{ds}{2} + \alpha * ds - \eta * tf} * b * \left(tf - \frac{ds}{2} + \alpha * ds\right)$$

$$* \left(ds - tf + \frac{1}{3} * \left(tf - \frac{ds}{2} + \alpha * ds\right)\right) - fy * \frac{tf - \frac{ds}{2} + \alpha * ds}{\frac{ds}{2} + \alpha * ds - \eta * tf} * w * (ds - 2 * tf) * \left(\frac{ds}{2}\right)$$

$$- \frac{1}{2} * \left(fy * \frac{\frac{ds}{2} + \alpha * ds - tf}{\frac{ds}{2} + \alpha * ds - \eta * tf} - fy * \frac{tf - \frac{ds}{2} + \alpha * ds}{\frac{ds}{2} + \alpha * ds - \eta * tf}\right) * w * (ds - 2 * tf)$$

$$* \left(tf + \frac{1}{3} * (ds - 2 * tf)\right) - fy * \frac{\frac{ds}{2} + \alpha * ds - tf}{\frac{ds}{2} + \alpha * ds - \eta * tf} * b * (tf - \eta * tf)$$

$$* \left(\eta * tf + \frac{1}{2} * (tf - \eta * tf)\right) - \frac{1}{2} * \left(fy - fy * \frac{\frac{ds}{2} + \alpha * ds - tf}{\frac{ds}{2} + \alpha * ds - \eta * tf}\right) * b * (tf - \eta * tf)$$

$$* \left(\eta * tf + \frac{1}{3} * (tf - \eta * tf)\right) - fy * b * \eta * tf * \left(\frac{1}{2} * \eta * tf\right) - fy * \frac{\frac{ds}{2} + \alpha * ds - dsb}{\frac{ds}{2} + \alpha * ds - \eta * tf} * \rho$$

$$* bcb * dcb * dsb$$

Using the assumed values of η and calculated values of α and ξ, the curvature of the cross-section can be calculated as follows:

$$K = 2 * \frac{eys}{ds + 2 * \alpha * ds - 2 * \eta * tf}$$

Stress Distribution Eight:

This stress distribution takes place when the neutral axis is located in the steel beam upper flange, the steel web is partially plastified, the stresses in the bottom slab reinforcements can be less or more than the yield stress based on the level of the reinforcement, and the stress in the upper concrete slab reaches the maximum allowable stress, as shown in Figure 3.10.

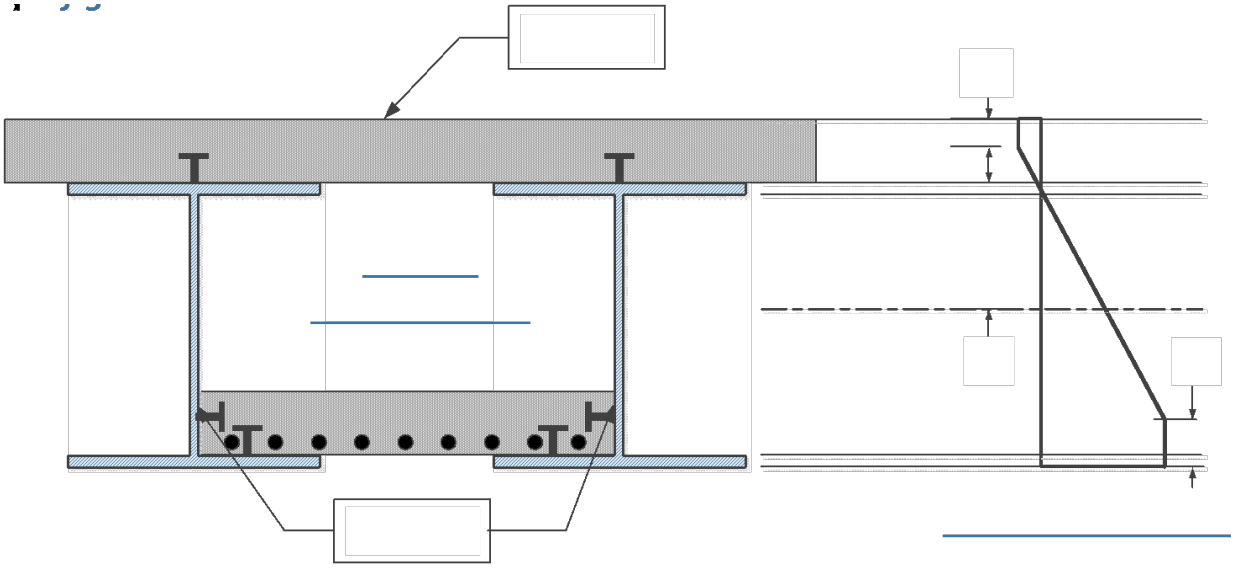

Figure 3.10 Stress distribution eight

The stress distribution eight can only be applicable if the following limits are satisfied:

- The neutral axis location is inside the steel beam upper flanges.
- All the lower steel flanges are plastified in addition to part of the steel webs.
- The maximum stresses in the upper concrete shall exceed the concrete maximum stresses (f_c).

To analyze the cross-section with stress distribution seven, the first step is to assume different values for the percent plastification in the steel webs (η), then solve the following two equations to obtain the location of the neutral axis (α) and the percent plastification of the upper concrete slab (ξ). All values of α and ξ shall fall in the previously mentioned range.

$$\left(\frac{fc}{1000}\right) * bc_t * \xi * dc_t + 0.5 * \left(\left(\frac{fc}{1000}\right) * n - fy * \frac{0.5-\alpha}{\alpha+0.5-\eta}\right) * \frac{bc_t}{n} * (dc_t - \xi * dc_t) + fy * \frac{0.5-\alpha}{\alpha+0.5-\eta}$$

$$* \frac{bc_t}{n} * (dc_t - \xi * dc_t) + \frac{1}{2} * fy * \frac{0.5-\alpha}{\alpha+0.5-\eta} * b * \left(\frac{ds}{2} - \alpha * ds\right) - \frac{1}{2} * fy * \frac{\frac{tf}{ds} - 0.5 + \alpha}{\alpha+0.5-\eta}$$

$$* b * \left(tf - \frac{ds}{2} + \alpha * ds\right) - fy * \frac{\frac{tf}{ds} - 0.5 + \alpha}{\alpha+0.5-\eta} * w * (ds - tf - \eta * ds) - \frac{1}{2}$$

$$* \left(fy - fy * \frac{\frac{tf}{ds} - 0.5 + \alpha}{\alpha+0.5-\eta}\right) * w * (ds - tf - \eta * ds) - fy * w * (\eta * ds - tf) - fy * tf$$

$$* b - f * \rho * bcb * dcb = 0$$

$$fy * \frac{0.5-\alpha}{\alpha+0.5-\eta} * \left(\frac{ds}{2} - \alpha * ds + dc_t - \xi * dc_t\right) = \left(\frac{fc}{1000}\right) * n * \left(\frac{ds}{2} - \alpha * ds\right)$$

The location of the neutral axis (α), distance from the edge of the bottom flange of the steel beam to the bottom slab reinforcements (d_{sb}), and percent of plastification in the steel web (η) are then used to calculate the stresses in the bottom slab reinforcements (f) as shown.

$$f = fy * \frac{\frac{ds}{2} + \alpha * ds - dsb}{\frac{ds}{2} + \alpha * ds - \eta * ds}$$

Using the assumed values of η and calculated values of α and ξ, the cross-sectional moment can be calculated as follows:

$$M = \left(\frac{fc}{1000}\right) * bc_t * \xi * dc_t * \left(ds + dc_t - \xi * \frac{dc_t}{2}\right) + 0.5 * \left(\left(\frac{fc}{1000}\right) * n - fy * \frac{0.5 - \alpha}{\alpha + 0.5 - \eta}\right) * \frac{bc_t}{n}$$

$$* (dc_t - \xi * dc_t) * \left(ds + \frac{2}{3} * dc_t * (1 - \xi)\right) + fy * \frac{0.5 - \alpha}{\alpha + 0.5 - \eta} * \frac{bc_t}{n} * (dc_t - \xi * dc_t)$$

$$* \left(ds + 0.5 * dc_t * (1 - \xi)\right) + \frac{1}{2} * fy * \frac{0.5 - \alpha}{\alpha + 0.5 - \eta} * b * \left(\frac{ds}{2} - \alpha * ds\right)$$

$$* \left(\frac{ds}{2} + \alpha * ds + \frac{2}{3} * \left(\frac{ds}{2} - \alpha * ds\right)\right) - \frac{1}{2} * fy * \frac{\frac{tf}{ds} - 0.5 + \alpha}{\alpha + 0.5 - \eta} * b * \left(tf - \frac{ds}{2} + \alpha * ds\right)$$

$$* \left(\frac{ds}{2} + \alpha * ds - \frac{2}{3} * \left(tf - \frac{ds}{2} + \alpha * ds\right)\right) - fy * \frac{\frac{tf}{ds} - 0.5 + \alpha}{\alpha + 0.5 - \eta} * w * (ds - tf - \eta * ds)$$

$$* \left(\eta * ds + 0.5 * (ds - tf - \eta * ds)\right) - \frac{1}{2} * \left(fy - fy * \frac{\frac{tf}{ds} - 0.5 + \alpha}{\alpha + 0.5 - \eta}\right) * w * (ds - tf - \eta * ds)$$

$$* \left(\eta * ds + \frac{1}{3} * (ds - tf - \eta * ds)\right) - fy * w * (\eta * ds - tf) * \left(\eta * ds - 0.5 * (\eta * ds - tf)\right)$$

$$- fy * tf * b * \frac{tf}{2} - f * \rho * bcb * dcb * dsb$$

Using the assumed values of η and calculated values of α and ξ, the curvature of the cross-section can be calculated as follows:

$$K = 2 * \frac{eys}{ds + 2 * \alpha * ds - 2 * \eta * ds}$$

Stress Distribution Nine:

The stress distribution nine takes place when the neutral axis is located in the upper concrete slab, the steel lower flange is partially plastified, the stresses in the bottom slab reinforcements are less than the yield stresses, and the stress in the upper concrete slab is less than the maximum allowable stress, as shown in Figure 3.11.

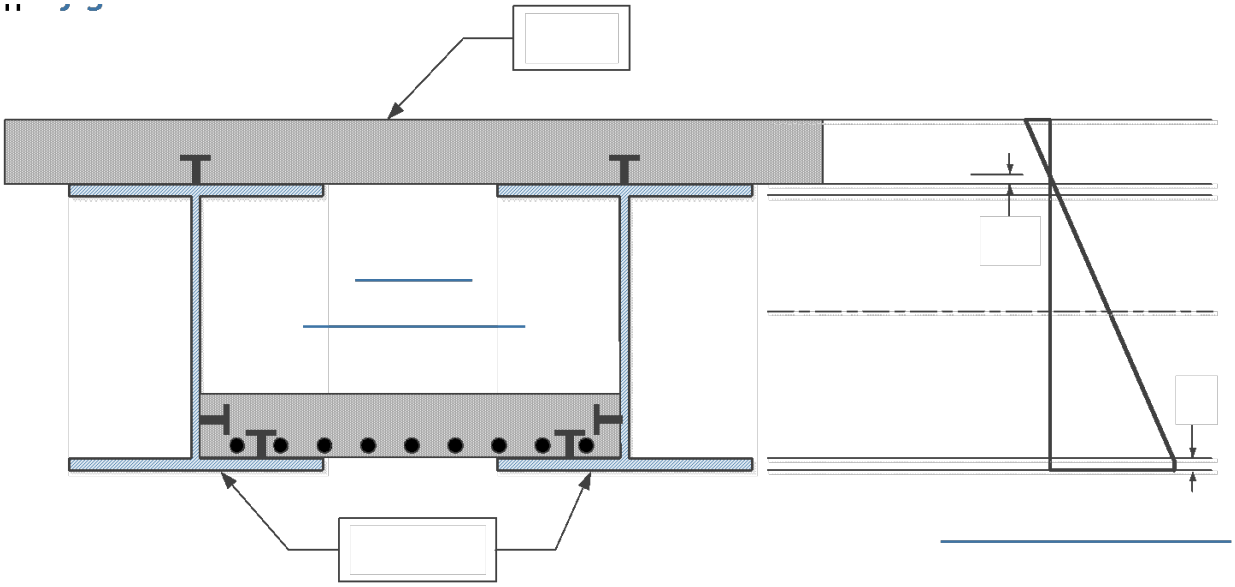

Figure 3.11 Stress distribution nine

The stress distribution nine can only be applicable if the following limits are satisfied:

- The neutral axis location is inside the upper concrete slab.
- Only part of the lower steel flanges is plastified.
- The maximum stresses in the upper concrete shall not exceed the concrete maximum stresses (f_c).

To analyze the cross-section with stress distribution nine, the first step is to assume different values for the percent plastification in the steel lower flanges (η), then solve the following second-order equation to obtain the location of the neutral axis (μ). All values of μ shall fall in the previously mentioned range.

$$0.5 * fy * \frac{dc_t - \mu * dc_t}{ds + \mu * dc_t - \eta * tf} * \frac{bc_t}{n} * (dc_t - \mu * dc_t) - fy * \frac{\mu * dc_t}{ds + \mu * dc_t - \eta * tf} * b * tf - 0.5$$
$$* \left(fy * \frac{\mu * dc_t + tf}{ds + \mu * dc_t - \eta * tf} - fy * \frac{\mu * dc_t}{ds + \mu * dc_t - \eta * tf}\right) * b * tf - fy$$
$$* \frac{\mu * dc_t + tf}{ds + \mu * dc_t - \eta * tf} * w * (ds - 2 * tf) - 0.5$$
$$* \left(fy * \frac{ds + \mu * dc_t - tf}{ds + \mu * dc_t - \eta * tf} - fy * \frac{\mu * dc_t + tf}{ds + \mu * dc_t - \eta * tf}\right) * w * (ds - 2 * tf) - fy$$
$$* \frac{ds + \mu * dc_t - tf}{ds + \mu * dc_t - \eta * tf} * b * (tf - \eta * tf) - 0.5 * \left(fy - fy * \frac{ds + \mu * dc_t - tf}{ds + \mu * dc_t - \eta * tf}\right) * b$$
$$* (tf - \eta * tf) - fy * b * \eta * tf - fy * \frac{ds + \mu * dc_t - dsb}{ds + \mu * dc_t - \eta * tf} * \rho * bcb * dcb = 0$$

The maximum stresses in the upper concrete slab shall be calculated using the following equation for the stress distribution nine. The maximum stresses in the upper concrete slab shall not exceed the previously mentioned limits.

$$C = \frac{fy}{n} * \frac{dc_t - \mu * dc_t}{ds + \mu * dc_t - \eta * tf}$$

Using the assumed values of η and μ, the cross-sectional moment can be calculated as follows:

$$\begin{aligned} M = {} & 0.5 * fy * \frac{dc_t - \mu * dc_t}{ds + \mu * dc_t - \eta * tf} * \frac{bc_t}{n} * (dc_t - \mu * dc_t) * \left(ds + dc_t - \frac{1}{3} * (dc_t - \mu * dc_t)\right) - fy \\ & * \frac{\mu * dc_t}{ds + \mu * dc_t - \eta * tf} * b * tf * \left(ds - \frac{1}{2} * tf\right) - 0.5 \\ & * \left(fy * \frac{\mu * dc_t + tf}{ds + \mu * dc_t - \eta * tf} - fy * \frac{\mu * dc_t}{ds + \mu * dc_t - \eta * tf}\right) * b * tf * \left(ds - \frac{2}{3} * tf\right) - fy \\ & * \frac{\mu * dc_t + tf}{ds + \mu * dc_t - \eta * tf} * w * (ds - 2 * tf) * \left(\frac{ds}{2}\right) - 0.5 \\ & * \left(fy * \frac{ds + \mu * dc_t - tf}{ds + \mu * dc_t - \eta * tf} - fy * \frac{\mu * dc_t + tf}{ds + \mu * dc_t - \eta * tf}\right) * w * (ds - 2 * tf) \\ & * \left(tf + \frac{1}{3} * (ds - 2 * tf)\right) - fy * \frac{ds + \mu * dc_t - tf}{ds + \mu * dc_t - \eta * tf} * b * (tf - \eta * tf) \\ & * \left(\eta * tf + \frac{1}{2} * (tf - \eta * tf)\right) - 0.5 * \left(fy - fy * \frac{ds + \mu * dc_t - tf}{ds + \mu * dc_t - \eta * tf}\right) * b * (tf - \eta * tf) \\ & * \left(\eta * tf + \frac{1}{3} * (tf - \eta * tf)\right) - fy * b * \eta * tf * \left(\frac{1}{2} * \eta * tf\right) - fy * \frac{ds + \mu * dc_t - dsb}{ds + \mu * dc_t - \eta * tf} \\ & * \rho * bcb * dcb * dsb \end{aligned}$$

Using the assumed values of η and μ, the curvature of the cross-section can be calculated as follows:

$$K = \frac{eys}{ds + \mu * dct - \eta * tf}$$

Stress Distribution Ten:

This distribution occurs when the neutral axis is located in the upper concrete slab, the steel web is partially plastified, the stresses in the bottom slab reinforcements can be less or more than the yield stress based on the level of the reinforcement, and the stress in the upper concrete slab is less than the maximum allowable stress, as shown in Figure 3.12.

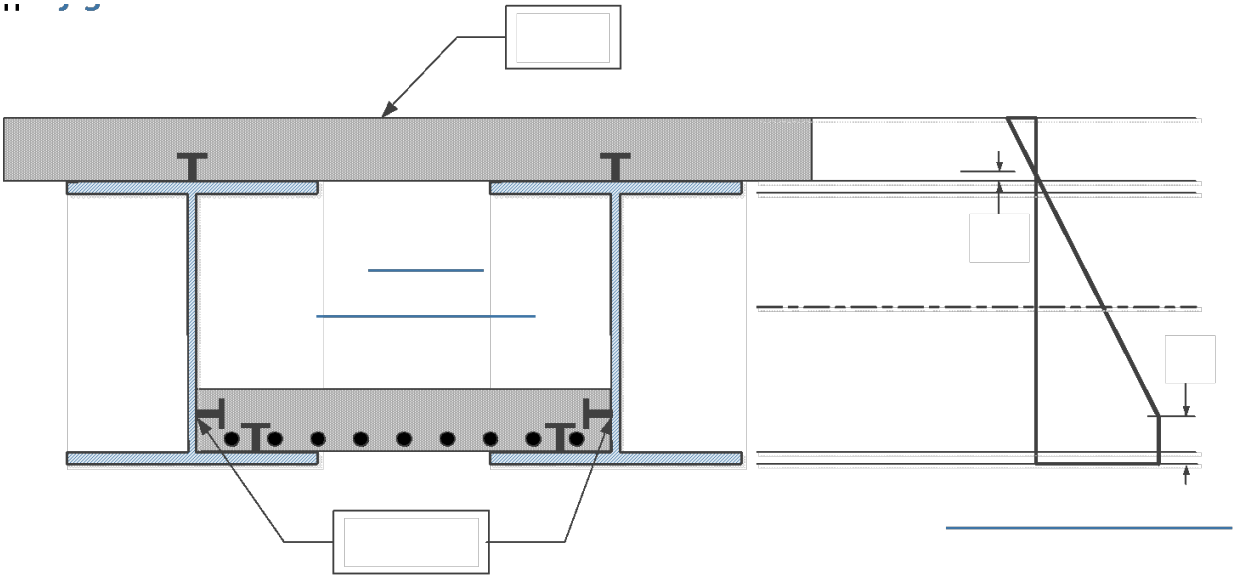

Figure 3.12 Stress distribution ten

The stress distribution ten can only be applicable if the following limits are satisfied:

- The neutral axis location is inside the upper concrete slab.
- All the lower steel flanges are plastified in addition to part of the steel webs.
- The maximum stresses in the upper concrete shall not exceed the concrete maximum stresses (f_c).

To analyze the cross-section with stress distribution ten, the first step is to assume different values for the percent plastification in the steel webs (η), then solve the following second-order equation to obtain the location of the neutral axis (μ). All values of μ shall fall in the previously mentioned range.

$$0.5 * fy * \frac{dc_t - \mu * dc_t}{ds + \mu * dc_t - \eta * ds} * \frac{bc_t}{n} * (dc_t - \mu * dc_t) - fy * \frac{\mu * dc_t}{ds + \mu * dc_t - \eta * ds} * b * tf - \frac{1}{2}$$
$$* \left(fy * \frac{\mu * dc_t + tf}{ds + \mu * dc_t - \eta * ds} - fy * \frac{\mu * dc_t}{ds + \mu * dc_t - \eta * ds}\right) * b * tf - fy$$
$$* \frac{\mu * dc_t + tf}{ds + \mu * dc_t - \eta * ds} * w * (ds - tf - \eta * ds) - \frac{1}{2} * \left(fy - fy * \frac{\mu * dc_t + tf}{ds + \mu * dc_t - \eta * ds}\right) * w$$
$$* (ds - tf - \eta * ds) - fy * w * (\eta * ds - tf) - fy * tf * b - f * \rho * bcb * dcb = 0$$

The location of the neutral axis (μ), distance from the edge of the bottom flange of the steel beam to the bottom slab reinforcements (d_{sb}), and percent of plastification in the steel web (η) are then used to calculate the stresses in the bottom slab reinforcements (f) as shown.

$$f = fy * \frac{ds + \mu * dc_t - dsb}{ds + \mu * dc_t - \eta * ds}$$

The maximum stresses in the upper concrete slab shall be calculated using the following equation for the stress distribution ten. The maximum stresses in the upper concrete slab shall not exceed the previously mentioned limits.

$$C = \frac{fy}{n} * dc_t * \frac{1-\mu}{ds - \eta * ds + \mu * dc_t}$$

Using the assumed values of η and μ, the cross-sectional moment can be calculated as follows:

$$\begin{aligned} M = {} & 0.5 * fy * \frac{dc_t - \mu * dc_t}{ds + \mu * dc_t - \eta * ds} * \frac{bc_t}{n} * (dc_t - \mu * dc_t) * \left(ds + \mu * dc_t + \frac{2}{3} * (dc_t - \mu * dc_t)\right) - fy \\ & * \frac{\mu * dc_t}{ds + \mu * dc_t - \eta * ds} * b * tf * \left(ds - \frac{tf}{2}\right) - \frac{1}{2} \\ & * \left(fy * \frac{\mu * dc_t + tf}{ds + \mu * dc_t - \eta * ds} - fy * \frac{\mu * dc_t}{ds + \mu * dc_t - \eta * ds}\right) * b * tf * \left(ds - 2 * \frac{tf}{3}\right) - fy \\ & * \frac{\mu * dc_t + tf}{ds + \mu * dc_t - \eta * ds} * w * (ds - tf - \eta * ds) * \left(\eta * ds + \frac{1}{2} * (ds - \eta * ds - tf)\right) - \frac{1}{2} \\ & * \left(fy - fy * \frac{\mu * dc_t + tf}{ds + \mu * dc_t - \eta * ds}\right) * w * (ds - tf - \eta * ds) \\ & * \left(\eta * ds + \frac{1}{3} * (ds - \eta * ds - tf)\right) - fy * w * (\eta * ds - tf) * \left(tf + \frac{1}{2} * (\eta * ds - tf)\right) - fy \\ & * tf * b * \left(\frac{tf}{2}\right) - f * \rho * bcb * dcb * dsb \end{aligned}$$

Using the assumed values of η and μ, the curvature of the cross-section can be calculated as follows:

$$K = \frac{eys}{ds + \mu * dct - \eta * ds}$$

Stress Distribution Eleven:

The distribution takes place when the neutral axis is located in the upper concrete slab, the steel lower flange is partially plastified, the stresses in the bottom slab reinforcements are less than the yield stresses, and the stress in the upper concrete slab reaches the maximum allowable stress, as shown in Figure 3.13.

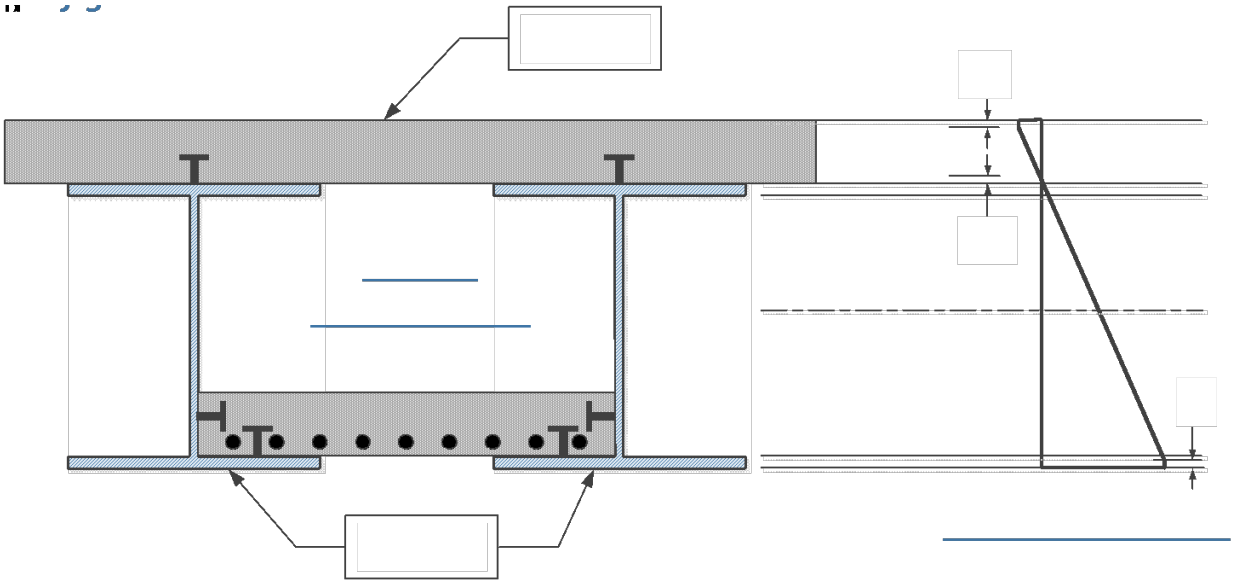

Figure 3.13 Stress distribution eleven

The stress distribution eleven can only be applicable if the following limits are satisfied:

- The neutral axis location is inside the upper concrete slab.
- Only part of the lower steel flanges is plastified.
- The maximum stresses in the upper concrete shall exceed the concrete maximum stresses (f_c).

To analyze the cross-section with stress distribution eleven, the first step is to assume different values for the percent plastification in the steel webs (η), then solve the following two equations to obtain the location of the neutral axis (μ) and the percent plastification of the upper concrete slab (ξ). All values of μ and ξ shall fall in the previously mentioned range.

$$\left(\frac{fc}{1000}\right) * bc_t * \xi * dc_t + 0.5 * \left(\frac{fc}{1000}\right) * bc_t * dc_t * (1 - \xi - \mu) - fy * \frac{\mu * dc_t}{ds + \mu * dc_t - \eta * tf} * b * tf$$
$$- 0.5 * \left(fy * \frac{\mu * dc_t + tf}{ds + \mu * dc_t - \eta * tf} - fy * \frac{\mu * dc_t}{ds + \mu * dc_t - \eta * tf}\right) * b * tf - fy$$
$$* \frac{\mu * dc_t + tf}{ds + \mu * dc_t - \eta * tf} * w * (ds - 2 * tf) - 0.5$$
$$* \left(fy * \frac{ds + \mu * dc_t - tf}{ds + \mu * dc_t - \eta * tf} - fy * \frac{\mu * dc_t + tf}{ds + \mu * dc_t - \eta * tf}\right) * w * (ds - 2 * tf) - fy$$
$$* \frac{ds + \mu * dc_t - tf}{ds + \mu * dc_t - \eta * tf} * b * (tf - \eta * tf) - 0.5 * \left(fy - fy * \frac{ds + \mu * dc_t - tf}{ds + \mu * dc_t - \eta * tf}\right) * b$$
$$* (tf - \eta * tf) - fy * b * \eta * tf - fy * \frac{ds + \mu * dc_t - dsb}{ds + \mu * dc_t - \eta * tf} * \rho * bcb * dcb = 0$$

$$\left(\frac{fc}{1000}\right) * n * (ds + \mu * dc_t - \eta * tf) = fy * dc_t * (1 - \xi - \mu)$$

Using the assumed values of η and the calculated values of μ and ξ, the cross-sectional moment can be calculated as follows:

$$M = \left(\frac{fc}{1000}\right) * bc_t * \xi * dc_t * \left(ds + dc_t - \frac{1}{2} * \xi * dc_t\right) + 0.5 * \left(\frac{fc}{1000}\right) * bc_t * dc_t * (1 - \xi - \mu)$$
$$* \left(ds + \mu * dc_t + \frac{2}{3} * dc_t * (1 - \xi - \mu)\right) - fy * \frac{\mu * dc_t}{ds + \mu * dc_t - \eta * tf} * b * tf * \left(ds - \frac{tf}{2}\right)$$
$$- 0.5 * \left(fy * \frac{\mu * dc_t + tf}{ds + \mu * dc_t - \eta * tf} - fy * \frac{\mu * dc_t}{ds + \mu * dc_t - \eta * tf}\right) * b * tf * \left(ds - \frac{2}{3} * tf\right)$$
$$- fy * \frac{\mu * dc_t + tf}{ds + \mu * dc_t - \eta * tf} * w * (ds - 2 * tf) * \left(\frac{ds}{2}\right) - 0.5$$
$$* \left(fy * \frac{ds + \mu * dc_t - tf}{ds + \mu * dc_t - \eta * tf} - fy * \frac{\mu * dc_t + tf}{ds + \mu * dc_t - \eta * tf}\right) * w * (ds - 2 * tf)$$
$$* \left(tf + \frac{1}{3} * (ds - 2 * tf)\right) - fy * \frac{ds + \mu * dc_t - tf}{ds + \mu * dc_t - \eta * tf} * b * (tf - \eta * tf)$$
$$* \left(\eta * tf + \frac{1}{2} * (tf - \eta * tf)\right) - 0.5 * \left(fy - fy * \frac{ds + \mu * dc_t - tf}{ds + \mu * dc_t - \eta * tf}\right) * b * (tf - \eta * tf)$$
$$* \left(\eta * tf + \frac{1}{3} * (tf - \eta * tf)\right) - fy * b * \eta * tf * \left(\frac{1}{2} * \eta * tf\right) - fy * \frac{ds + \mu * dc_t - d_{add}}{ds + \mu * dc_t - \eta * tf}$$
$$* \rho * bcb * dcb * dsb$$

Using the assumed values of η and the calculated values of μ and ξ, the curvature of the cross-section can be calculated as follows:

$$K = \frac{eys}{ds + \mu * dct - \eta * tf}$$

Stress Distribution Twelve:

The distribution takes place when the neutral axis is located in the upper concrete slab, the steel web is partially plastified, the stresses in the bottom slab reinforcements can be less or more than the yield stress based on the level of the reinforcement, and the stress in the upper concrete slab reaches the maximum allowable stress, as shown in Figure 3.14.

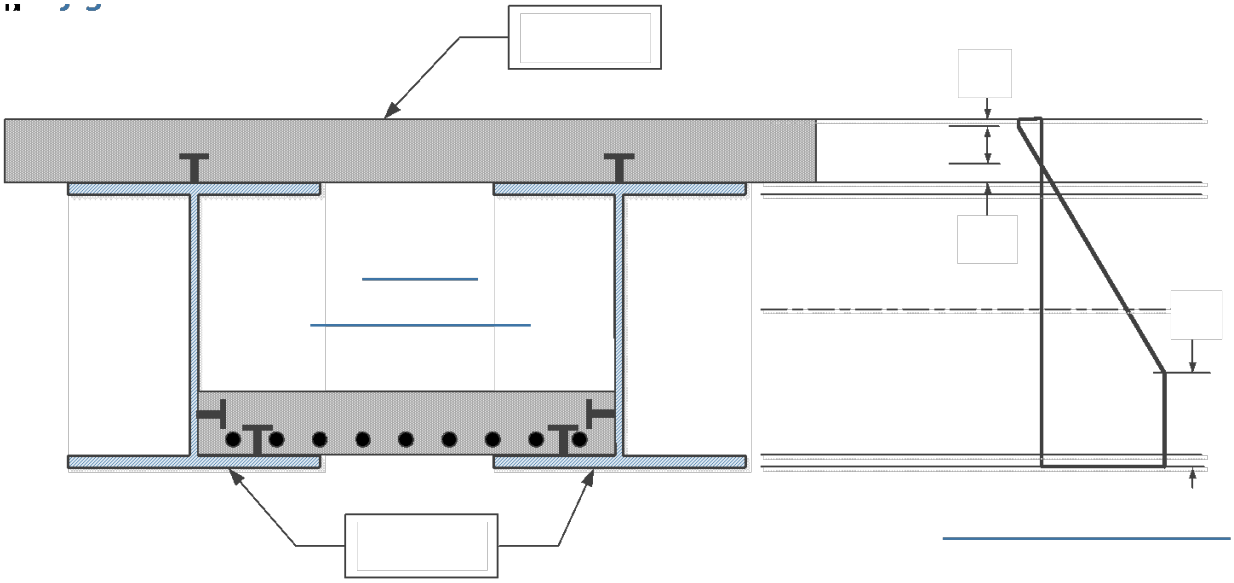

Figure 3.14 Stress distribution twelve

The stress distribution twelve can only be applicable if the following limits are satisfied:

- The neutral axis location is inside the upper concrete slab.
- All the lower steel flanges are plastified in addition to part of the steel webs.
- The maximum stresses in the upper concrete shall exceed the concrete maximum stresses (f_c).

To analyze the cross-section with stress distribution twelve, the first step is to assume different values for the percent plastification in the steel webs (η), then solve the following two equations to obtain the location of the neutral axis (μ) and the percent plastification of the upper concrete slab (ξ). All values of μ and ξ shall fall in the previously mentioned range.

$$\left(\frac{fc}{1000}\right) * bc_t * \xi * dc_t + \frac{1}{2} * \left(\frac{fc}{1000}\right) * bc_t * dc_t * (1 - \xi - \mu) - fy * \frac{\mu * dc_t}{ds + \mu * dc_t - \eta * ds} * b * tf - \frac{1}{2} * \left(fy * \frac{\mu * dc_t + tf}{ds + \mu * dc_t - \eta * ds} - fy * \frac{\mu * dc_t}{ds + \mu * dc_t - \eta * ds}\right) * b * tf - fy * \frac{\mu * dc_t + tf}{ds + \mu * dc_t - \eta * ds} * w * (ds - \eta * ds - tf) - \frac{1}{2} * \left(fy - fy * \frac{\mu * dc_t + tf}{ds + \mu * dc_t - \eta * ds}\right) * w * (ds - \eta * ds - tf) - fy * w * (\eta * ds - tf) - fy * b * tf - f * \rho * bcb * dcb = 0$$

$$fy * dc_t * (1 - \mu - \xi) - \left(\frac{fc}{1000}\right) * n * (ds - \eta * ds + \mu * dc_t) = 0$$

The location of the neutral axis (μ), distance from the edge of the bottom flange of the steel beam to the bottom slab reinforcements (d_{sb}), and percent of plastification in the steel web (η) are then used to calculate the stresses in the bottom slab reinforcements (f) as shown.

$$f = fy * \frac{ds + \mu * dc_t - dsb}{ds + \mu * dc_t - \eta * ds}$$

Using the assumed values of η and the calculated values of μ and ξ, the cross-sectional moment can be calculated as follows:

$$\begin{aligned} M = {} & \left(\frac{fc}{1000}\right) * bc_t * \xi * dc_t * \left(ds + dc_t - \frac{1}{2} * \xi * dc_t\right) + \frac{1}{2} * \left(\frac{fc}{1000}\right) * bc_t * dc_t * (1 - \xi - \mu) \\ & * \left(ds + \mu * dc_t + \frac{2}{3} * dc_t * (1 - \xi - \mu)\right) - fy * \frac{\mu * dc_t}{ds + \mu * dc_t - \eta * ds} * b * tf * \left(ds - \frac{tf}{2}\right) - \frac{1}{2} \\ & * \left(fy * \frac{\mu * dc_t + tf}{ds + \mu * dc_t - \eta * ds} - fy * \frac{\mu * dc_t}{ds + \mu * dc_t - \eta * ds}\right) * b * tf * \left(ds - \frac{2}{3} * tf\right) - fy \\ & * \frac{\mu * dc_t + tf}{ds + \mu * dc_t - \eta * ds} * w * (ds - \eta * ds - tf) * \left(\eta * ds + \frac{1}{2} * (ds - \eta * ds - tf)\right) - \frac{1}{2} \\ & * \left(fy - fy * \frac{\mu * dc_t + tf}{ds + \mu * dc_t - \eta * ds}\right) * w * (ds - \eta * ds - tf) \\ & * \left(\eta * ds + \frac{1}{3} * (ds - \eta * ds - tf)\right) - fy * w * (\eta * ds - tf) * \left(tf + \frac{1}{2} * (\eta * ds - tf)\right) - fy \\ & * b * tf * \left(\frac{tf}{2}\right) - f * \rho * bcb * dcb * dsb \end{aligned}$$

Using the assumed values of η and the calculated values of μ and ξ, the curvature of the cross-section can be calculated as follows:

$$K = \frac{eys}{ds + \mu * dct - \eta * ds}$$

Stress Distribution Thirteen:

The distribution takes place when the neutral axis is located in the upper concrete slab, the steel upper flange is partially plastified, the stresses in the bottom slab reinforcements reach the yield stress, and the stress in the upper concrete slab reaches the maximum allowable stress, as shown in Figure 3.15.

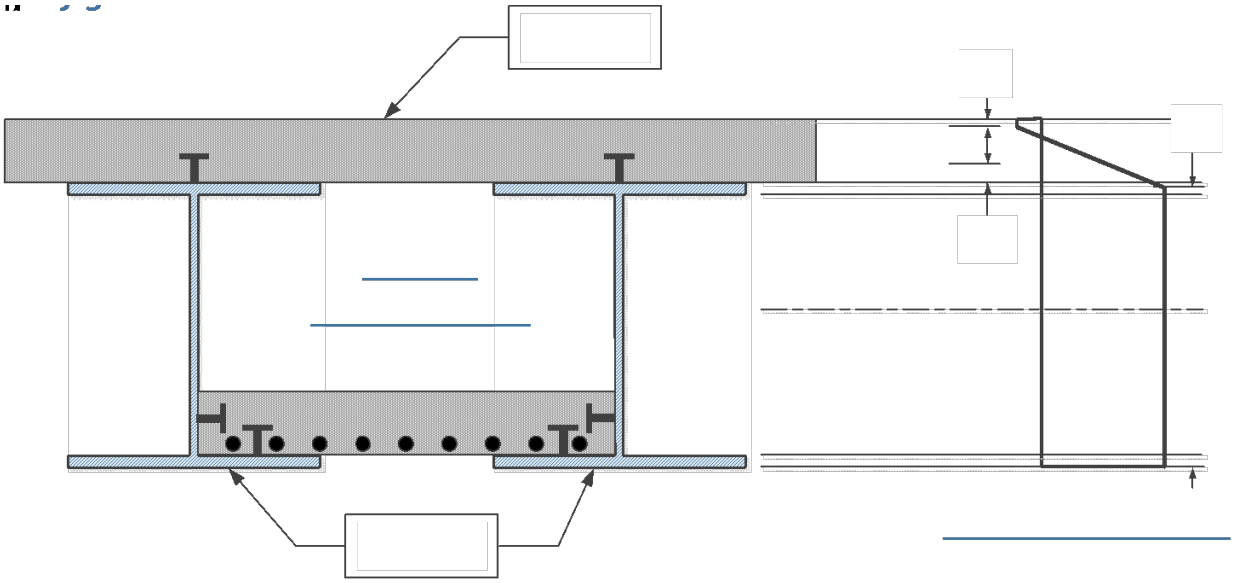

Figure 3.15 Stress distribution thirteen

The stress distribution thirteen can only be applicable if the following limits are satisfied:

- The neutral axis location is inside the upper concrete slab.
- All the lower steel flanges and webs are plastified in addition to part of the steel upper flanges.
- The maximum stresses in the upper concrete shall exceed the concrete maximum stresses (f_c).

To analyze the cross-section with stress distribution thirteen, the first step is to assume different values for the percent plastification in the steel webs (η), then solve the following two equations to obtain the location of the neutral axis (μ) and the percent plastification of the upper concrete slab (ξ). All values of μ and ξ shall fall in the previously mentioned range.

$$\left(\frac{fc}{1000}\right) * bc_t * \xi * dc_t + 0.5 * \left(\frac{fc}{1000}\right) * bc_t * dc_t * (1 - \xi - \mu) - fy * \mu * \frac{dc_t}{ds - \eta * ds + \mu * dc_t} * b * tf$$
$$- 0.5 * \left(fy - fy * \mu * \frac{dc_t}{ds - \eta * ds + \mu * dc_t}\right) * b * (ds - \eta * ds)$$
$$- \left(fy - fy * \mu * \frac{dc_t}{ds - \eta * ds + \mu * dc_t}\right) * b * (\eta * ds + tf - ds) - fy * w * (ds - 2 * tf)$$
$$- fy * b * tf - fy * \rho * bcb * dcb = 0$$

$$fy * dc_t * (1 - \mu - \xi) - \left(\frac{fc}{1000}\right) * n * (ds - \eta * ds + \mu * dc_t) = 0$$

Using the assumed values of η and the calculated values of μ and ξ, the cross-sectional moment can be calculated as follows:

$$M = \left(\frac{fc}{1000}\right) * \xi * dc_t * bc_t * \left(ds + dc_t - \xi * \frac{dc_t}{2}\right) + 0.5 * \left(\frac{fc}{1000}\right) * dc_t * bc_t * (1 - \xi - \mu)$$
$$* \left(ds + \mu * dc_t + \frac{2}{3} * dc_t * (1 - \xi - \mu)\right) - fy * \mu * \frac{dc_t}{ds - \eta * ds + \mu * dc_t} * b * tf * \left(ds - \frac{tf}{2}\right)$$
$$- 0.5 * \left(fy - fy * \mu * \frac{dc_t}{ds - \eta * ds + \mu * dc_t}\right) * b * (ds - \eta * ds) * \left(ds - \frac{2}{3} * (ds - \eta * ds)\right)$$
$$- \left(fy - fy * \mu * \frac{dc_t}{ds - \eta * ds + \mu * dc_t}\right) * b * (\eta * ds + tf - ds)$$
$$* \left(\eta * ds - 0.5 * (\eta * ds + tf - ds)\right) - fy * w * (ds - 2 * tf) * \frac{ds}{2} - fy * b * tf * \frac{tf}{2} - fy$$
$$* \rho * bcb * dcb * dsb$$

Using the assumed values of η and the calculated values of μ and ξ, the curvature of the cross-section can be calculated as follows:

$$K = \frac{eys}{ds + \mu * dct - \eta * ds}$$

4. NUMERICAL APPROACH

In this section, a finite element model for a double composite bridge is presented as an example. Two different finite element software are utilized to investigate the linear and non-linear behavior of the double composite sections, and to evaluate the potential variation of results as a function of the modeling approach used. The first finite element software used is SAP2000 (version 18.1.1), which can capture the linear behavior of the double composite section while considering the bottom slab reinforcements. In addition, ABAQUS, which is a general-purpose finite element software, is also used to investigate both the linear and non-linear behavior of the double composite section. The example used to demonstrate the modeling capabilities comprises a double composite simply-supported bridge.

4.1 Example Description

A simply supported small bridge with a total span length of 15 ft is modeled. It was first modeled by Charles Culver in 1960 (1960) as a single composite and modified in this study to be a double composite bridge. The bridge is only two girders made from W12 X 27 with a total depth of 11.95 in., total flange width of 6.5 in., web thickness of 0.24 in., and flange thickness of 0.4 in. This section has a total cross-sectional area of 7.97 in.^{2} and a moment of inertia about the strong axis of 204.1 in^4. The spacing between the two steel beams is 50 in. The steel cross-sectional stress-strain relation is assumed elastic-perfectly plastic (to match the analytical method presented in Chapter 3) with yield stresses of 39 ksi and with elastic modules of 29,000 ksi. The top slab is a reinforced concrete slab with a thickness of 4 in. and a total width of 122 in. modeled with elastic-perfectly plastic material with maximum compressive stresses of 3.6 ksi and elastic modules of 29,00 ksi. A minimum reinforcement ratio is assumed for the top concrete slab to conservatively obtain the effect of the double composite on the bridge behavior. The bottom slab is 4 in. deep and 49.52 in. wide to fit between the two steel beams. The bottom slab reinforcements are included in the presented model and are assumed to resist the tensile stresses even if the bottom concrete cracked due to its limited resistance under tension. Both the top and bottom slabs are rigidly connected to the steel beams using rigid shear connectors that should be designed to carry the total shear flow up to the bridge failure point. Figure 4.1 shows the cross-section of the investigated bridge.

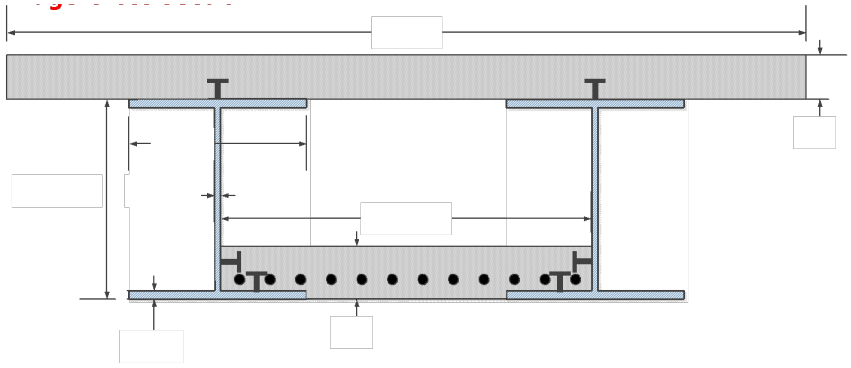

Figure 4.1 Investigated bridge layout

The bridge is loaded by four equal concentrated loads close to the middle of the bridge to ensure a constant moment straining action and no shear straining action along the length of the bridge. The distance between the concentrated loads is 18 in. The loads are applied vertically through the centroid of the steel beams to avoid any lateral deflection, which could rise due to load eccentricity.

4.2 SAP2000 Finite Element Modeling (frame element modeling)

The SAP2000 finite element software was utilized to model the example bridge and capture the linear performance region of the double composite section. An illustration is provided to show the steps required to build and analyze the model. Figure 4-2 shows the general configuration of the investigated bridge.

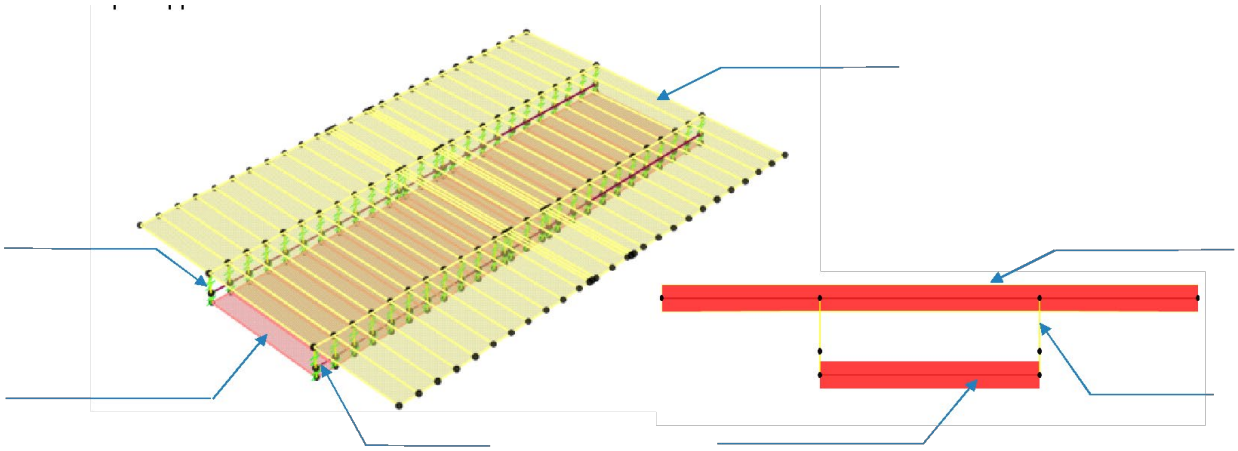

Figure 4.2 Double composite bridge SAP 2000 general configuration

Model construction

- The New SAP2000 model is developed with default units (Kips-in-F).
- A system of 3-dimensional grids is created based on the bridge components dimension.
- Two frame elements of 15 ft long are created that represent the steel beams.
- A horizontal area element is created with offset distance from the frame elements to model the top concrete slab. This offset distance represents the distance between the centerline of the steel beam and the centerline of the top concrete slab.
- Another horizontal area element is created with an offset distance to represent the bottom concrete slab. This offset distance represents the distance between the centerline of the steel beam and the centerline of the bottom concrete slab.
- The two shell elements (top and bottom) are connected to the frame elements using link elements.

Material definition

- From the Define menu, a Materials command is selected, then the Add New Material option is used to define the materials.
- The steel material definition is shown in Figure 4.3 (a), where the elastic modulus of the steel is 29,000 ksi, and the yield stress of the steel material is an option that will not affect the elastic analysis. It is worth noting that even if a value is inserted for the yield stress, the software still conducts linear analysis and is not able to handle non-linear simulations.
- The top slab concrete material definition is shown in Figure 4-3 (b), where the elastic modulus of the concrete is 2,900 ksi and the concrete compressive strength is again an option that will not affect the elastic analysis.
- The bottom slab concrete material has two definitions based on the model type. In the first model, which neglects the bottom slab reinforcements, the concrete material in the tension zone is considered to have no stiffness. Therefore, a new material with a very small (close to zero) elastic modulus is defined. In the second model, which considers the bottom slab reinforcements, the steel material in

the bottom concrete is defined while the effect of the bottom concrete is neglected as it is assumed not to work in the tension zone.

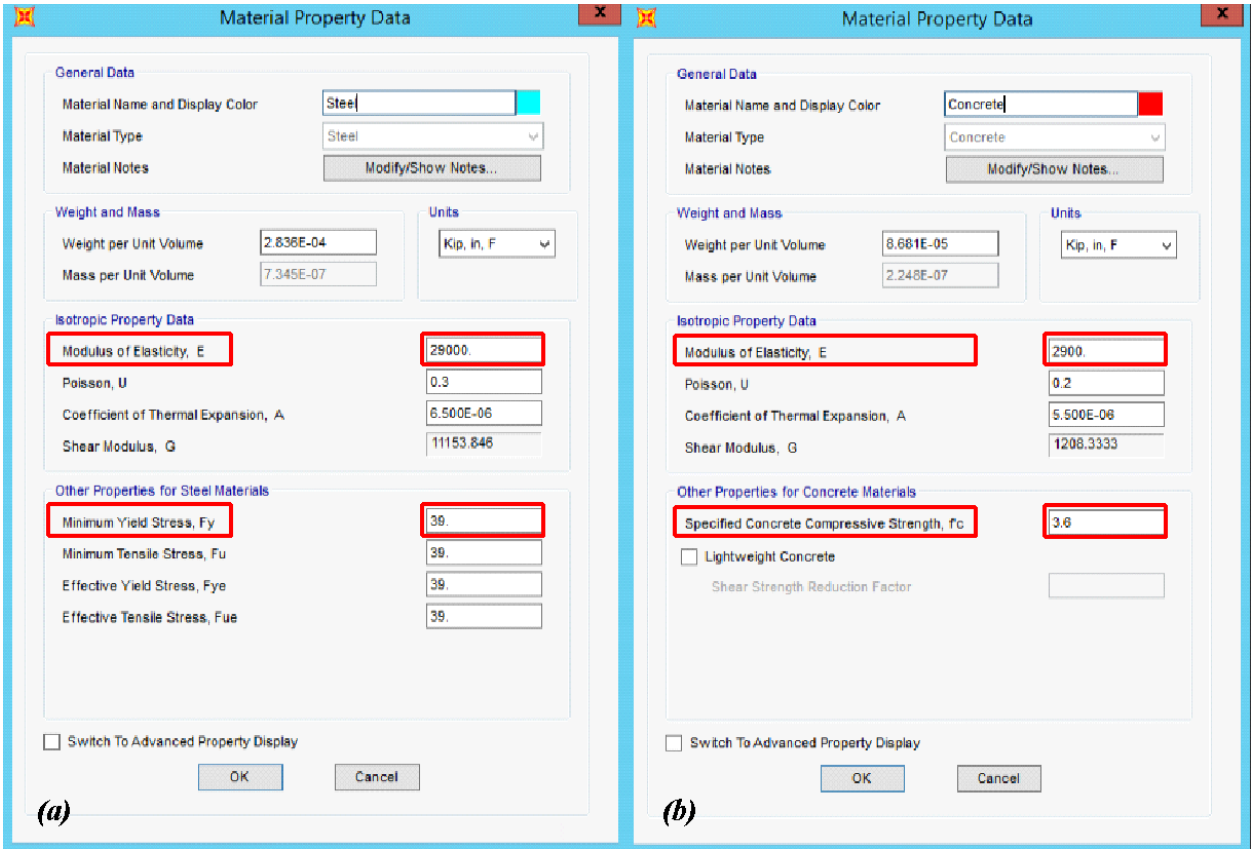

Figure 4.3 (a) steel material properties and (b) concrete material properties

Element definition

- From the Define menu, the section properties command is selected, then the frame section command is selected, and then the Add New Property option is used to define the steel frame element. Figure 4.4 shows the definition of the steel beam cross-section used. The steel material, which was defined before, is assigned to the 12WF27 steel beam section.

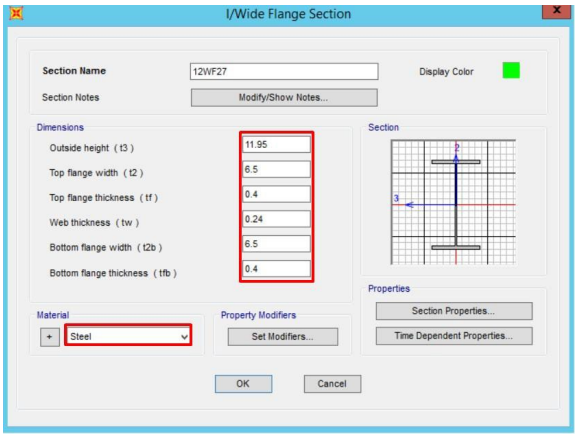

Figure 4.4 Steel beam frame element definition

- From the Define menu, the section properties command is selected, then the area sections command is selected, and then Add New Section option is used to define the top and bottom concrete shell elements. Figure 4-5 shows the definition of the top concrete slab shell element used. The concrete material, which was defined before, is assigned to the top concrete shell element.

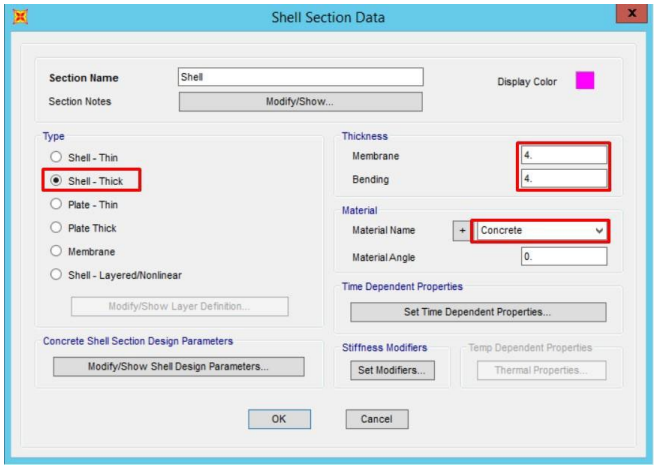

Figure 4.5 Concrete shell element definition

- The bottom concrete element is defined using two models. In the first model, the effect of the bottom slab reinforcements is not included. Specifically, the bottom slab is modeled using non-reinforced concrete. In the second model, the effect of bottom slab reinforcements is included, where the bottom slab is modeled using the steel reinforcement area only. The tensile properties of the concrete are not included since the concrete model will not work under tensile stresses. One of the other approaches to model concrete in the tension is by modifying the concrete tensile capacity.
- The rebar material is selected to have the same material as the steel beam, which was previously defined. The rebars' total area is assumed to be 8.7 $in.^2$ and is divided into two equal layers, while the cover distance for the rebar is assumed to be 1 in.
- The rigid link is modeled using the command Material, then section properties and then link\support properties. A linear link type is selected with all degrees of freedom coupled as shown in Figure 4.6.

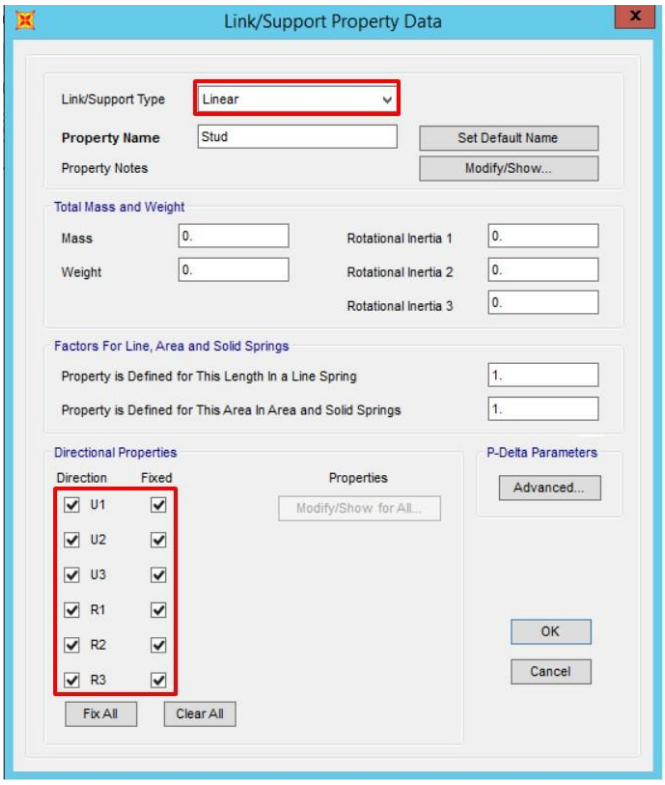

Figure 4.6 The rigid link properties

Element assignment

- The previous properties are assigned to the different bridge components as follows. The 12WF27 steel beam section is assigned to the frame elements to represent the steel beams of the double composite bridge. The shell elements are assigned to the top and bottom area elements to form the top and bottom slab. The stud properties are assigned to the link element that works as the shear stud elements. To assign the properties to different elements, the assign command is used.

Load and support definition

- The investigated bridge is simply supported. Therefore, restraints are applied to the frame section that represents the beam element of the double composite section. The restraints are applied to the frame joints by selecting the end joints, then using the command assign, then command joint, then command restraints. Figure 4.7 shows the frame support definition for hinged support.

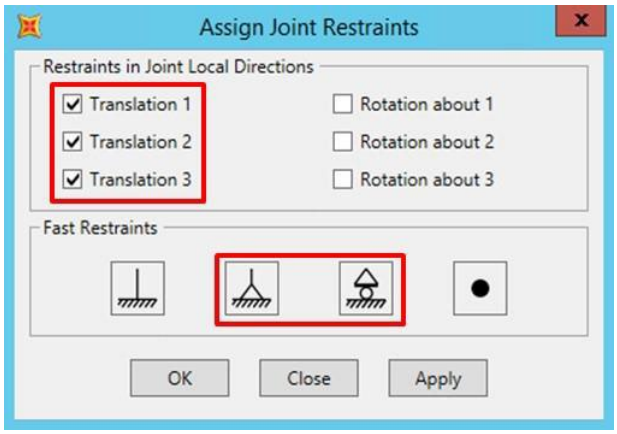

Figure 4.7 Frame restraints definition

- The investigated bridge has four load points (two loads per beam). The load assignment starts with the load pattern definition. A new load case with the name "Push" is defined. In addition, the load case definition for the same load pattern is defined. Moreover, the assign command is used to assign the loads at the loading joints. Figure 4.8 shows the joint load forces assigned at the loading points.

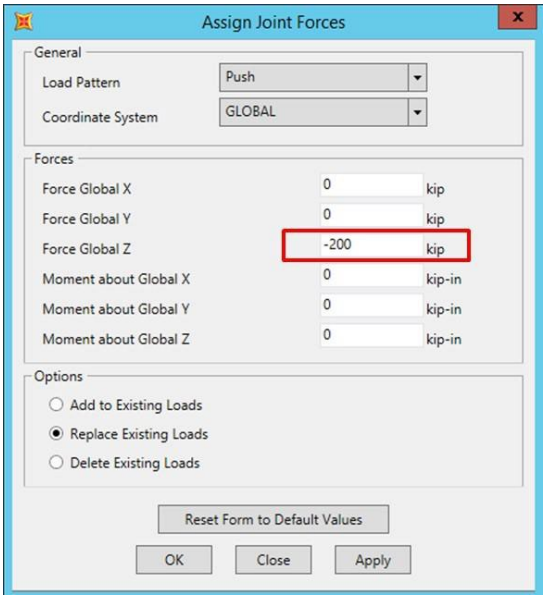

Figure 4.8 The joint load assign

Analysis processing

- A space frame analysis option is selected with a standard solver option.
- The run analysis option is selected to run the analysis.

Post-processing of results

❖ To show the stresses in the different model components, a display option is selected. Figure 4.9 shows the stress distribution in the SAP2000 model components for both cases – that is with and without considering the bottom slab reinforcements effect.

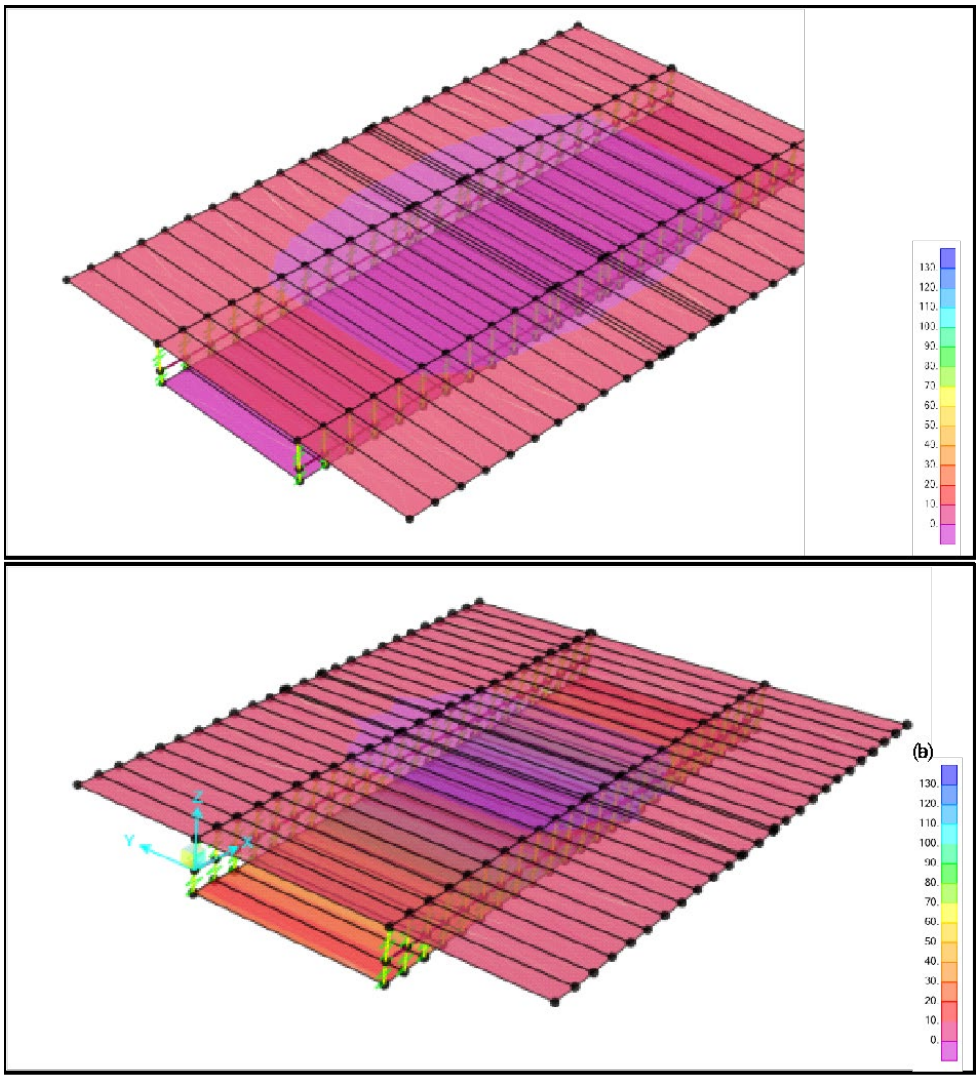

Figure 4.9 Maximum stresses at different model components, (a) without bottom slab reinforcements effect and (b) with bottom slab reinforcements effect

❖ To obtain the deflection at mid-length of the bridge, a display option is used to show the deformed shape command and the load case that contains the bridge load is selected. Figure 4.10 shows the deflection value from SAP2000 for the cases with and without considering the bottom slab reinforcements effect.

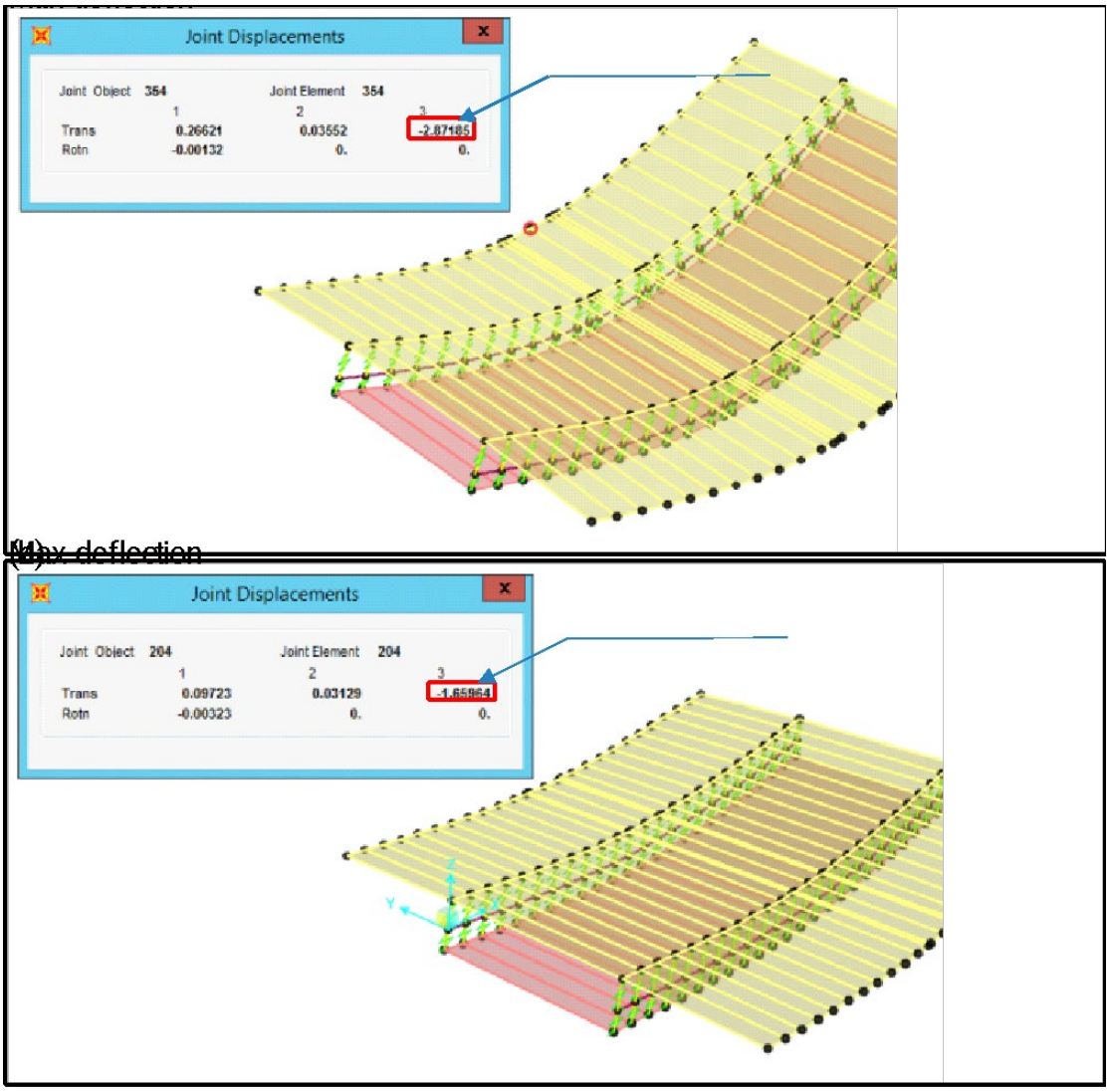

Figure 4.10 The deflection at the middle section in case of neglecting the bottom slab reinforcements, (a) without bottom slab reinforcements effect, and (b) with bottom slab reinforcements effect

- The resulting moment versus deflection relationship is shown in the results section and compared with the analytical solution as well as the ABAQUS finite element model.

4.3 SAP2000 Finite Element Modeling (shell element modeling)

One of the main disadvantages of using frame elements to represent the steel beams in the investigated bridge is the inability to connect the steel beam and concrete slab at the exact location. Using the frame elements, connect the whole steel section (at its centroid) with the concrete, which is not representative of real construction. By adding the offset distance between the steel beam center and the top and bottom concrete, the expected error can be reduced. Modeling the steel beam section using shell elements, on the other hand, allows for the proper connection to be made since only the top flange of the steel beam should be connected to the top concrete slab and only the lower flange should be connected to the lower concrete slab. In addition, it will allow for the connection to be made between the concrete and the corresponding flange faces.

The steps below summarize the proposed modeling modifications of the frame elements in SAP2000 to overcome the issue of proper connection locations and improve the accuracy of the results. Figure 4.11 shows the general configuration of the shell element SAP2000 model for the investigated bridge.

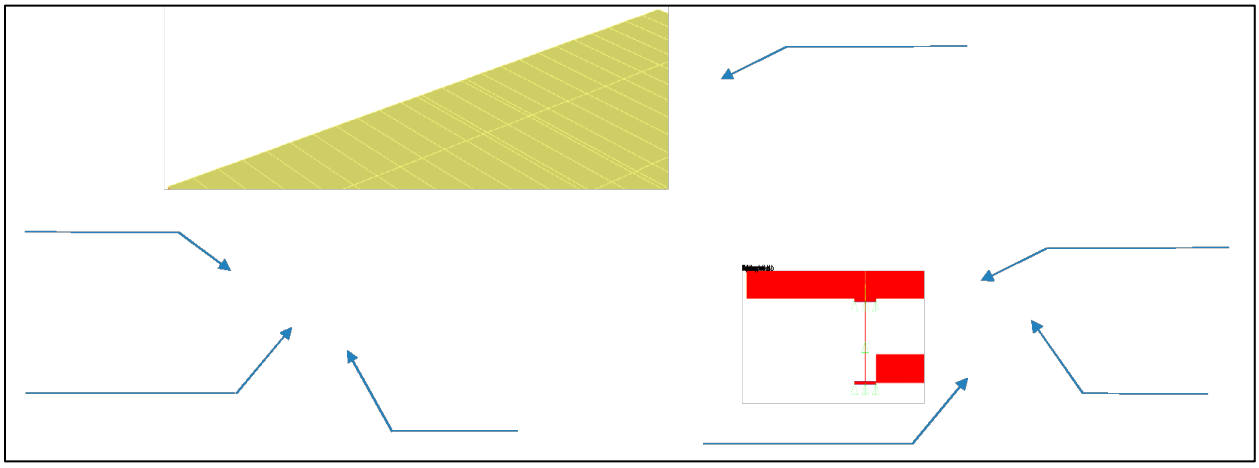

Figure 4.11 General configuration of the SAP2000 shell element model

Model construction

- The model includes the shell element for the steel beams and the top and bottom concrete slab. The shell elements for the steel beams are drawn at the centerline of the beam flanges and web elements.
- The shell elements that form the steel beam web and flanges are meshed together to guarantee no separation between the flanges and web elements.
- The steel beam bottom flange is the only component that connects to the bottom slab shell elements.
- Modeling of the top and bottom shell elements that represent the top and bottom slab is conducted similarly to what was outlined in the previous SAP2000 model except that the width of the bottom flange is reduced.

Material definition

- The material is defined similarly to that of the previous SAP2000 model.

Element definition

- The steel beam elements are the flanges and the web; however, both elements have different thicknesses. Therefore, the flanges and the web are classified into two different elements. The element definition for the slabs, rebar, and rigid links is the same as the previous.

Element assignment

- The element assignment is the same as previously except there is no frame assignment in this model.

Load and support definition

- The load assignment is the same as before.
- The support assignment in the shell element model is realized using joint restraints for the steel beam. In the case of hinged support, the whole steel section nodes at the beam hinged end are constrained against the movement in the global Y and Z directions and only the middle web joint is restrained against the movement in the X direction to guarantee a free rotation and full prevention of the lateral movements, as shown in Figure 4.12 (a). The roller support at the other end of the steel beam is modeled in the same way except without any restraint in the X direction, as shown in Figure 4.12 (b).

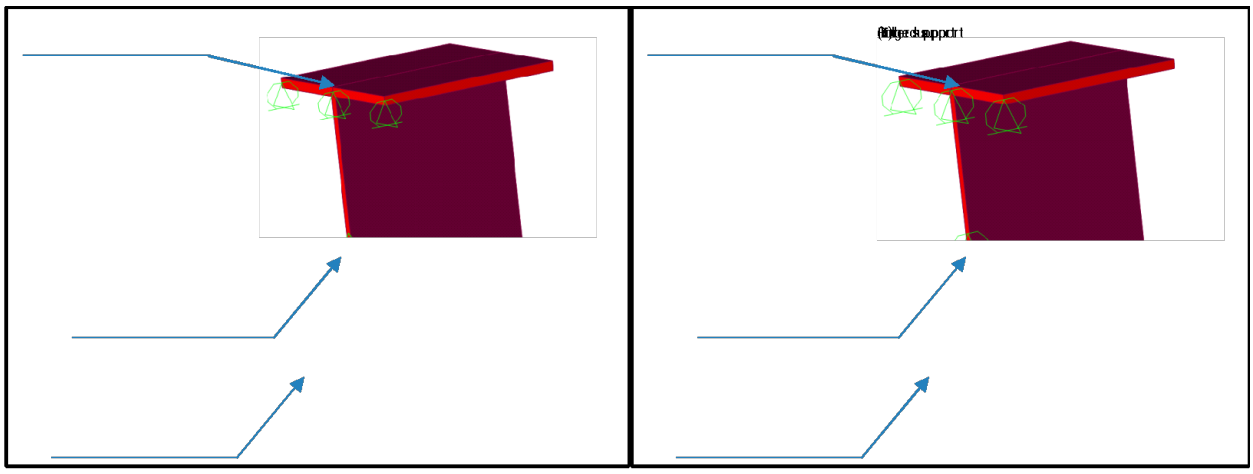

Figure 4.12 (a) The hinged support definition and (b) The roller support definition

Analysis processing

- The analysis processing is the same as mentioned before.

Post-processing of results

- To show the stresses in different model components, a display option is selected. Figure 4.13 shows the stress distribution in the SAP2000 model components for both cases – that is with and without considering the bottom slab reinforcements effect.

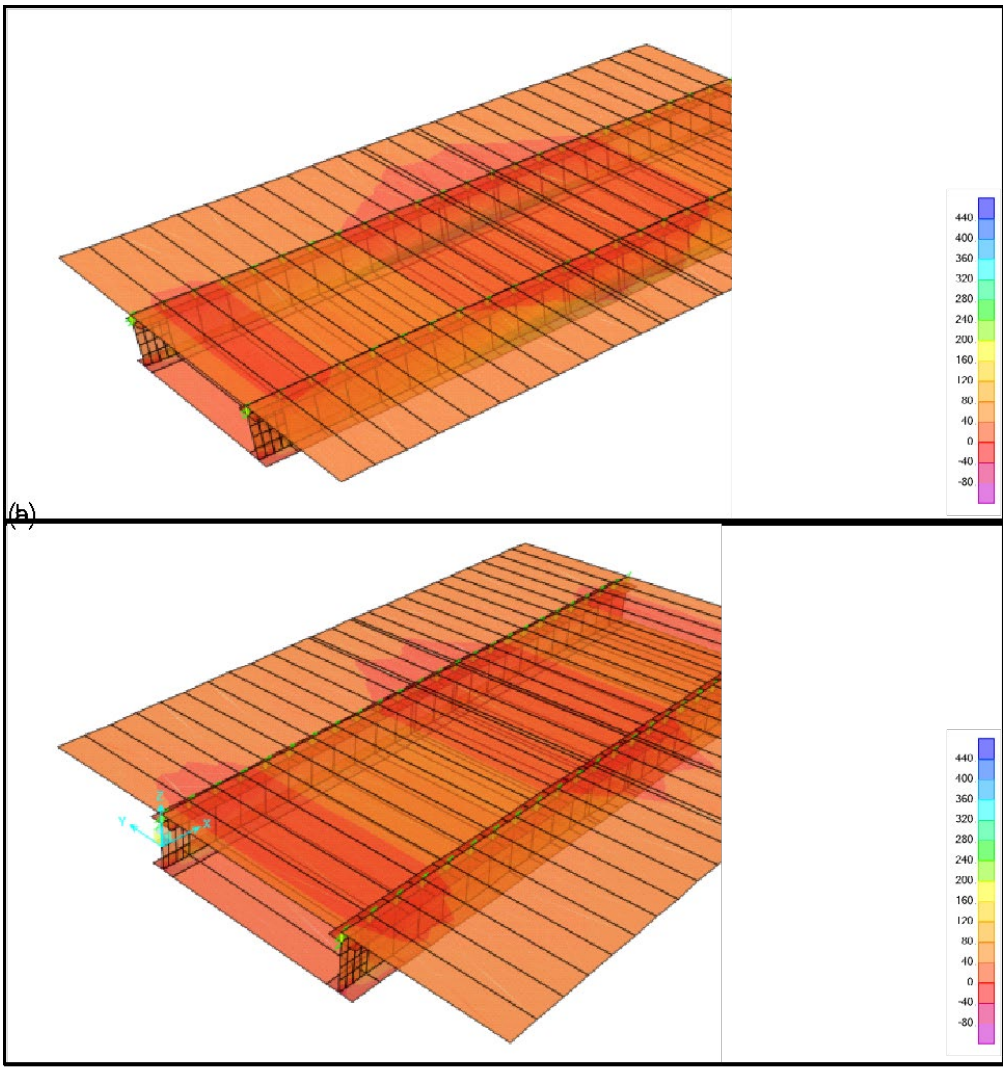

Figure 4.13 Maximum stresses at different model components, (a) without bottom slab reinforcements effect and (b) with bottom slab reinforcements effect

❖ To obtain the deflection at mid-length of the bridge, a display option is used to show deformed shape command and the load case that contains the bridge load is selected. Figure 4.14 shows the deflection value from SAP2000 for the cases with and without considering the bottom slab reinforcements effect.

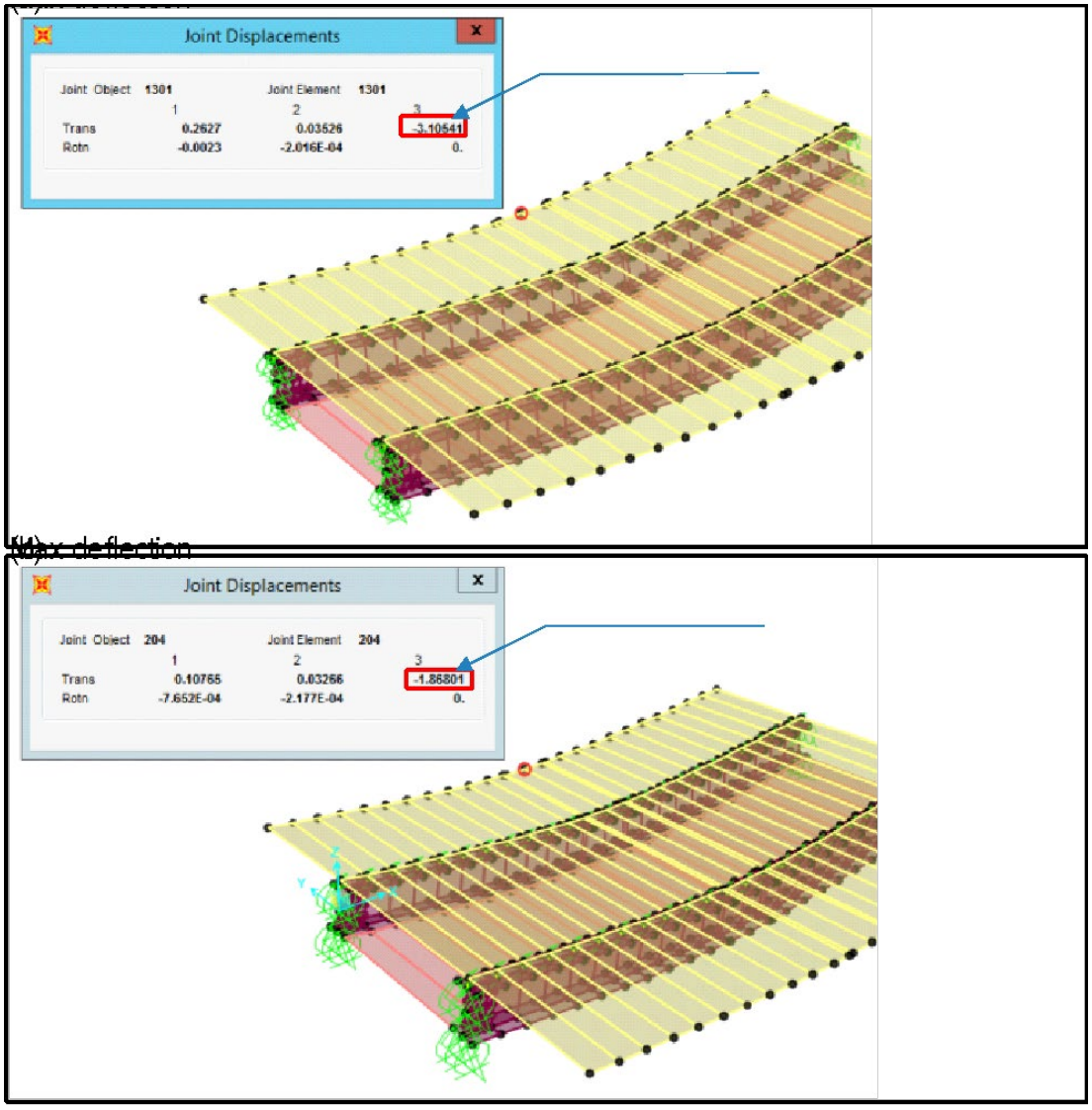

Figure 4.14 The deflection at mid-length of the bridge, (a) without bottom slab reinforcements effect and (b) with bottom slab reinforcements effect

❖ The resulting moment versus deflection relation is shown in the results section and compared with the analytical solution as well as the ABAQUS finite element model.

4.4 ABAQUS Finite Element Modeling

The non-linear behavior of the double composite section is analyzed using the finite element software ABAQUS. The software can model material inelasticity and geometric non-linearity. In this section, a description of the proposed ABAQUS model is provided. Figure 4.15 shows a general 3-D view of the ABAQUS model of the investigated bridge.

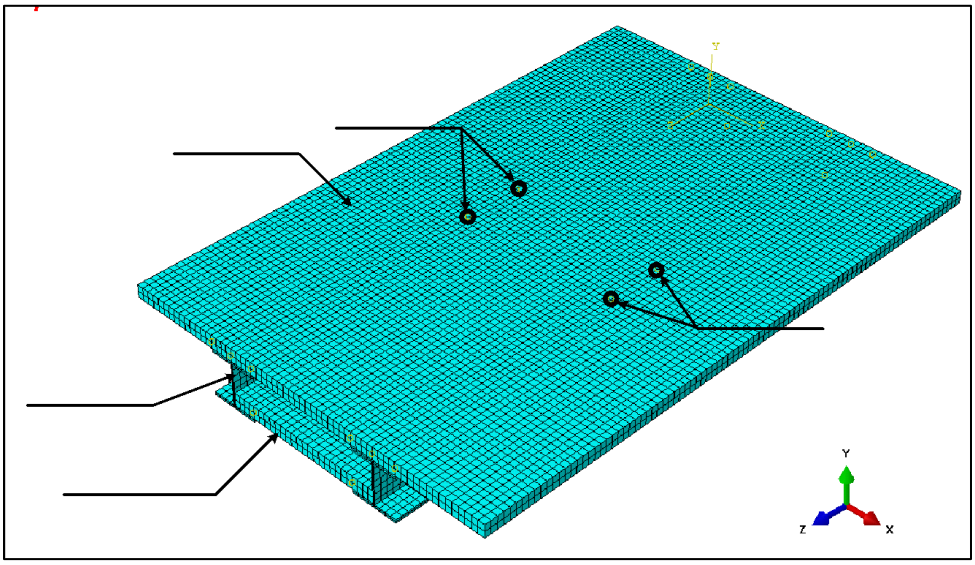

Figure 4.15 General view of the ABAQUS model for double composite bridge

Model construction

- A shell element model type is constructed by defining different areas to represent the different model components (top and bottom slabs, steel beam flanges, and steel beam web). The creation of the different components considers the offset distances between different elements.

Material definition

- The steel material is defined as elastic-perfectly plastic with an elastic modulus of 29,000 ksi and yield stress of 39.0 ksi. The steel is assumed to have the same behavior in tension and compression.
- The concrete material is defined as elastic-perfectly plastic with an elastic modulus of 2,900 ksi and crushing stress of 4.0 ksi. The concrete is assumed to have no stiffness or strength in tension.

Element definition

- Four-node shell element is selected to model all steel and concrete elements. This element type provides six degrees of freedom at each node, which allows for capturing all expected deformations.
- Different thicknesses are assigned to different components.
- A beam element, representing the shear stud, is used to connect the steel beam to the top and bottom concrete slab. The rigid beam element transfers all the deformation between the two connected nodes.

Element Meshing

- A fine mesh with a maximum size of 1 in. is assigned to different components.
- The material and the element type are assigned during the meshing step.

Load and support definition

- The investigated bridge is simply supported. Therefore, one end is selected to be hinged and the other end is a roller. The hinged support is modeled by defining a zero displacement for all nodes on the edge of the steel web in the two perpendicular directions to the beam axis and by defining a zero displacement for the steel flanges in the beam axis.
- The investigated bridge has four load points (two loads per beam). Those loads are defined as a concentrated force at the points of load application.

Analysis processing

- Static non-linear analysis with load control is used to investigate the non-linear behavior of the double composite section.

Post-processing of results

- A stress distribution for the shell elements, which is shown in Figure 4.16, displays the contribution of the steel and concrete in resisting the loads.

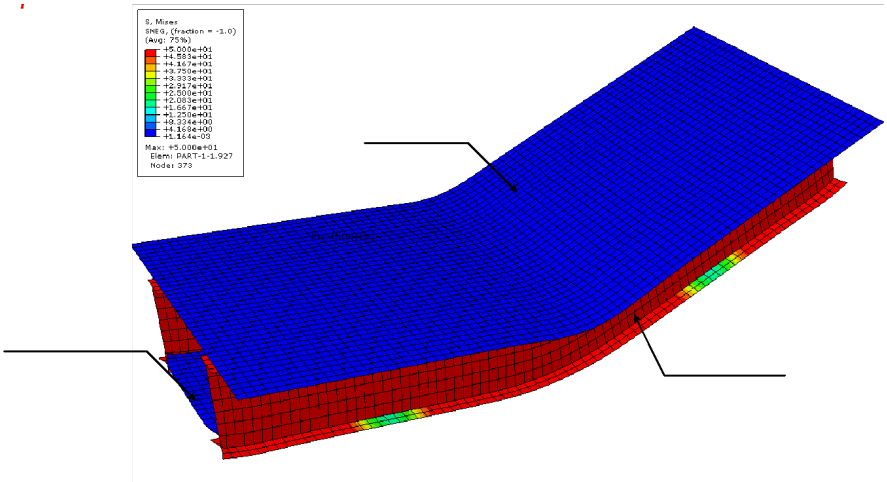

Figure 4.16 Von misses stress distribution for the double composite bridge

- The load and displacement at the mid-length of the steel beam are extracted from the ABAQUS model using the post-processing command.

5. RESULTS AND DISCUSSIONS

In this section, verification of the presented analytical approach and comparison is made between the different finite element analysis approaches used to simulate the behavior of the double composite section in both the linear and non-linear stages. The results also highlight the advantages of using double composite sections in bridge construction.

5.1 Comparison Between Different Modeling Approaches for Double Composite Bridges

The bridge cross-section, previously mentioned in Chapter 4, is used to compare different modeling approaches for the double composite sections. A slight difference between the different analysis approaches used to study the double composite section is shown in Figure 5-1. Following are the main observations when comparing the different analysis approaches for the double composite section when the effect of the bottom slab is included:

- The analytical and ABAQUS finite element models show good agreement in the initial stiffness and the fully plastic moment and deflection values.
- The SAP2000 models show good agreement in the elastic analysis; however, the shell element model is closer to the ABAQUS model as it includes a more realistic connection between the bottom slab and the lower steel flange. Therefore, the shell elements analysis approach is recommended in the case when the double composite behavior is considered.
- The SAP2000 model exhibits less stiffness than both the analytical and ABAQUS models. The reason is that the connection definition in SAP2000 is slightly different than that of ABAQUS; however, it is close to the initial stiffness of the analytical approach, as shown in Figure 5.1.

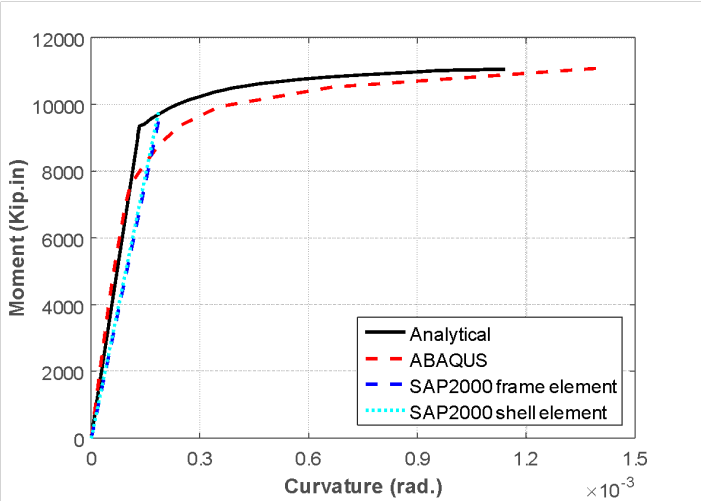

Figure 5.1 Comparison of the moment-curvature relationship between the analytical and finite element approaches to investigate the behavior of the double composite section with the effect of the bottom slab reinforcements

5.2 Verifications and Examples

For validation of the analytical solution, four different simply supported bridges are utilized; these have spans ranging from 4.6 m (15 ft) to 25.4 m (83.3 ft), thicknesses of concrete slabs from 10.2 cm (4 in.) to 25.4 cm (12 in.), number of steel beams including 2, 3, and 5 beams, and steel cross-sections including W14 x 132, W30 x 211, W40 x 324, and W 44x335, as shown in Figure 5.2

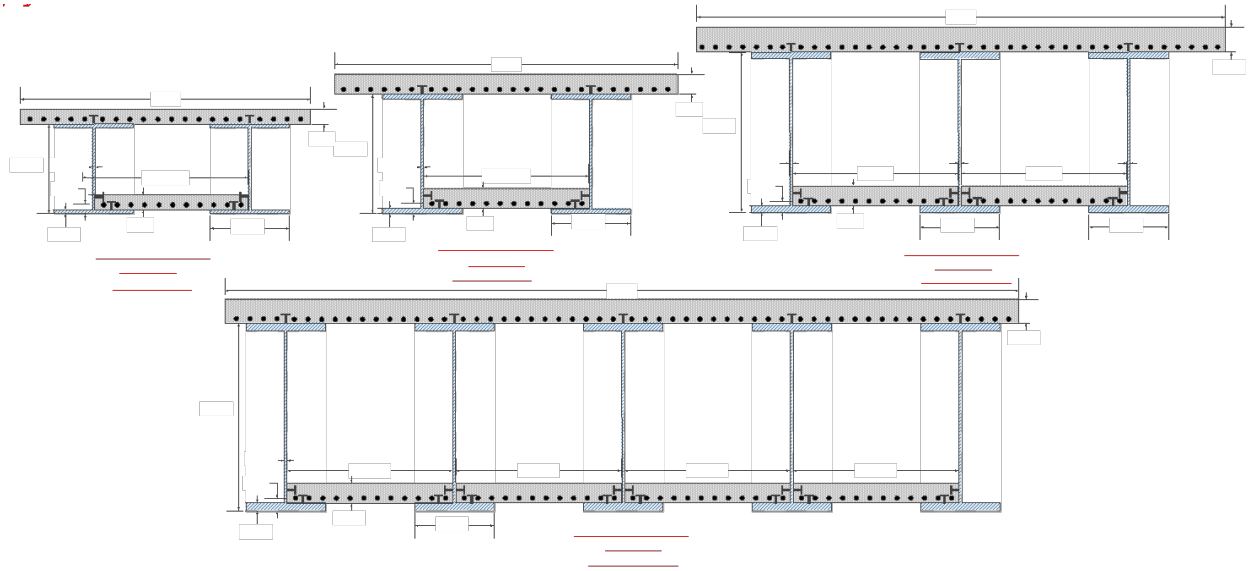

Figure 5.2 The cross-section for the investigated double composite bridges

Finite element models are built for each bridge, as shown in Figure 5.3.

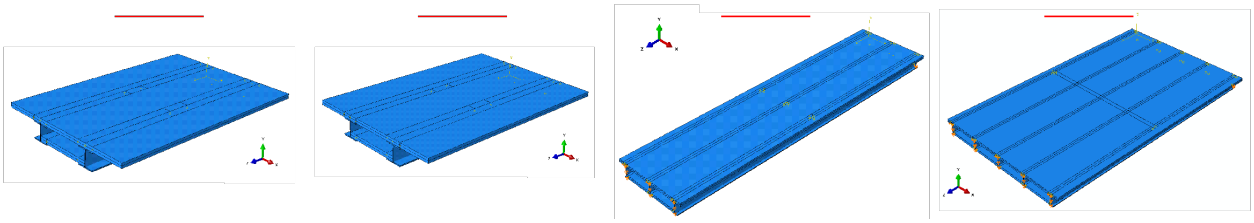

Figure 5.3 The finite element model for the four bridges

A slight difference between the different analysis approaches used to study the double composite section is shown in Figure 5.4 (a), (b), (c), and (d). The analytical and ABAQUS finite element models show good agreement in the initial stiffness, yielding moment, and the fully plastic moment as well as the corresponding deflection values.

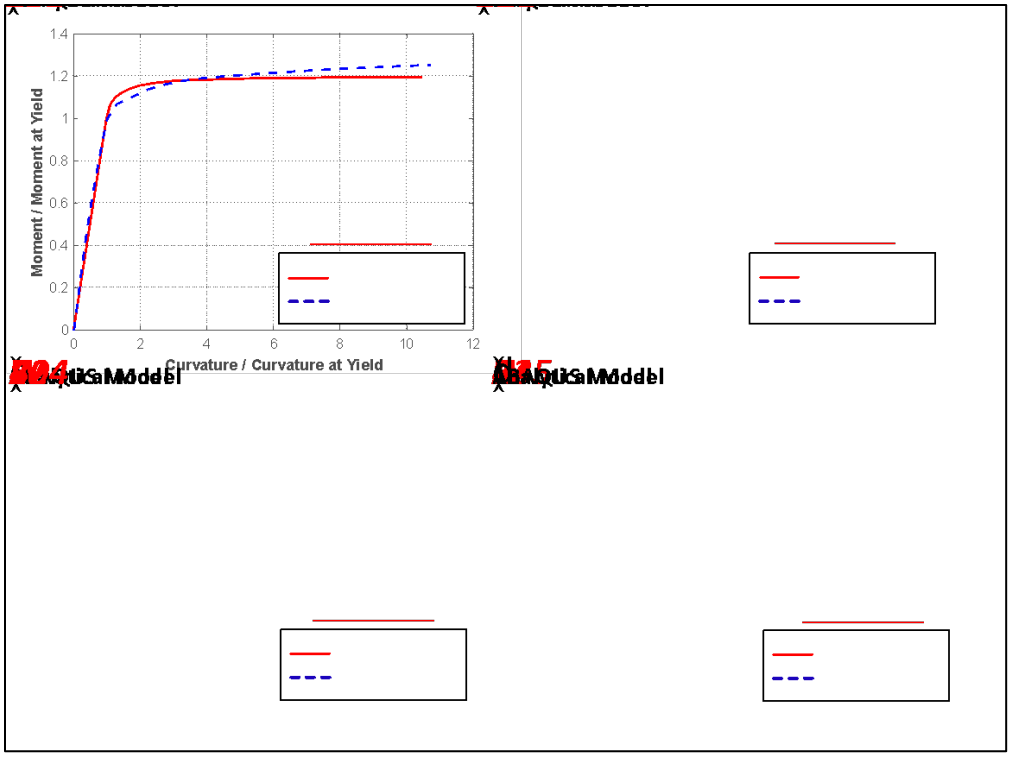

Figure 5.4 Comparisons of the moment-curvature relationship between the analytical and finite element approach for double composite bridges built using a) W14 x 132, b) W30 x 211, c) W40 x 324, and d) W44 x 335

5.3 Effect of Using Double Composite Section

The double composite section enhanced the investigated bridge performance by reducing the deflection and increasing the yield capacity of the bridge. However, in the case when minimum reinforcements are used in the bottom slab, where neglecting the bottom slab reinforcements is valid, the bridge behavior is close to that of a single composite and the advantages of using the double composite section are minimal. Therefore, the bottom slab reinforcements area is considered one of the important factors in deciding on the use of double composite sections. One of the main limits of using more reinforcement in the bottom slab is the strain limit specified by the ACI 318-14 (2014), which limits the maximum reinforcement in the structural elements. This report did not consider that limit for the sake of comparison. To further reflect on the use of double composite sections, the analytical formulation is used to compare between the single and double composite bridge cross-sections. Figure 5 shows a comparison between the single composite and the double composite behavior for the investigated bridges. Here are the main advantages of using the double composite section:

1. The initial rotational stiffness of the double composite section increased in comparison with that of a single composite; however, this increase is a function of bridge dimensions, properties, and the bottom slab reinforcements ratio, as shown in Figure 5-5. The initial rotational stiffness increased by 41% and 2.7% for W 44x335 and W 14x132 bridges, respectively. However, this improvement is mainly due to the increase in the cross-section yield moment and not the curvature at a yield point.
2. The double composite section yield moment increased in comparison with that of a single composite, although the effect on the curvature at the yield points is less.

3. The fully plastic moment increased in comparison with that of a single composite. The curvature at the fully plastic point increased in comparison with that of a single composite except for the W 30x211 bridge, in which the top concrete slab is expected to reach the failure limit state before the steel beams and the failure was dominated by the top concrete.

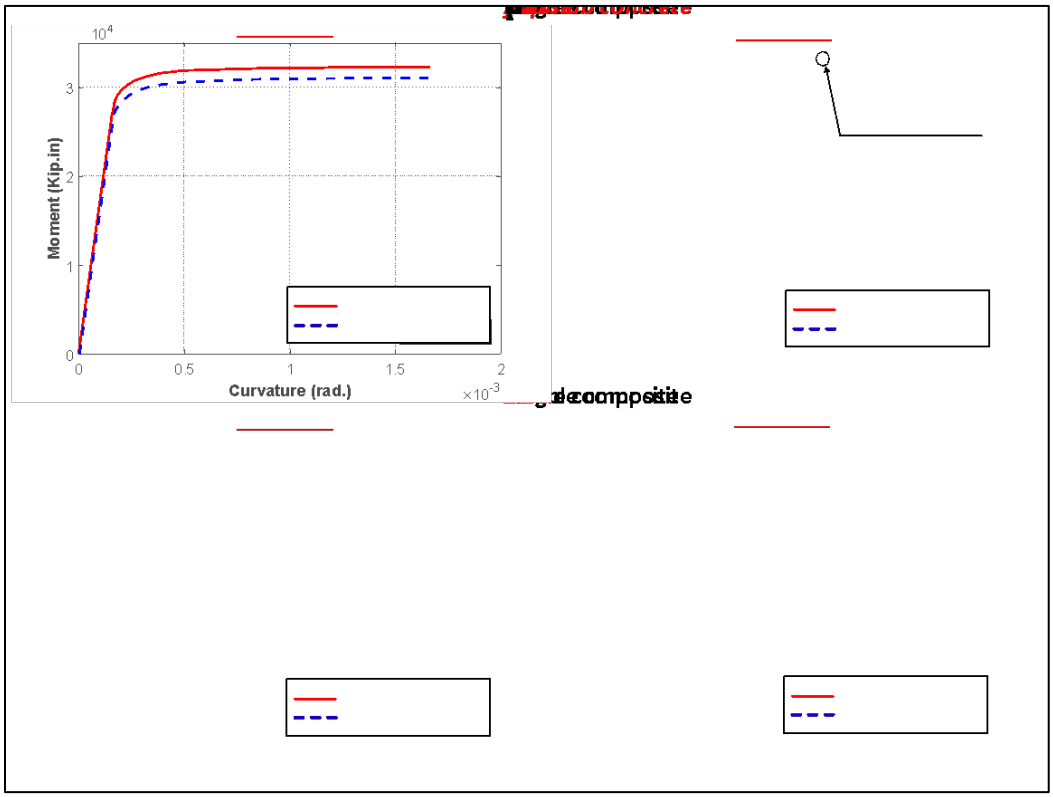

Figure 5.5 Effect of the double composite section on the moment versus curvature relationships for: a) W 14x132, b) W 30x211, c) W 40x324, and d) W 44x335

5.4 Effect of Span Length on the Elastic Deflection of the Double Composite Bridge

Bridge serviceability limit state, in the form of deflection, is included in the AASHTO Bridge Design *Specifications* (American Association of State Highway and Transportation Officials 2012). Service loads shall be used to calculate the bridge maximum deflection, which is then compared with the specified limit based on bridge usages. For instance, general bridges with vehicular loads have a deflection limit of span/800. The devised analytical approach is used in this section to estimate the bridge curvature values for different W sections. Figure 5 shows the investigated bridge cross-section. The beam cross-section, loading conditions, and supports change in every analysis to investigate the effect of these parameters on the elastic deflection of the double composite bridges. Bridges with spans from 20 ft to 90 ft are investigated. Both simply supported and fixed supported bridges are examined. Single concentrated versus uniformly distributed loads are assigned separately in every analyzed case.

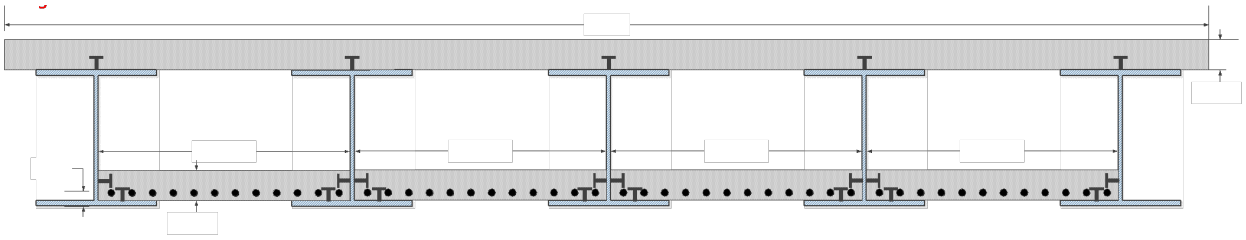

Figure 5.6 The investigated bridge cross-section

The analytical analysis output is moment versus curvature. Therefore, a relationship between the curvature and deflection is required to calculate the maximum deflection for different bridge loading and boundary conditions. Using Euler–Bernoulli beam theory, beam curvature can be written as $K = M/EI$, where the maximum moment at the mid-span can be calculated as $M = PL/4$ for simple supported beams with concentrated load (P) at the mid-span, $M = PL/8$ for fixed end beams with concentrated load (P) at the mid-span, $M = (WL\text{^}2)/8$ for simple supported beams with distributed load (W) and $M = (WL\text{^}2)/24$ for fixed end beams with distributed load (W). By double integrating the curvature (K) equation, the maximum deflection of the beam at the mid-span section can be calculated as $\Delta = (PL\text{^}3)/48EI$ for simple supported beams with concentrated load (P), $\Delta = (PL\text{^}3)/192EI$ for fixed end beams with concentrated load (P), $\Delta = (5WL\text{^}4)/384EI$ for simple supported beams with distributed load (W), and $\Delta = (WL\text{^}4)/384EI$ for fixed end beams with distributed load (W). Therefore, for linear elastic beams, where the boundary conditions are constant (i.e., no plastic hinge formation and spread of inelasticity along with the member), the deflection can be calculated from curvature by dividing the previously mentioned equations. Figure 5.7 shows the relationship between the maximum elastic deflection calculated at the yield point of the double composite bridge and the span of the bridge. Eight steel sections from W 24x162 to W 44x335 are selected for the analysis, which covers a wide range of moments of inertia from 5,170 in^4 to 50,400 in^4. As shown in Figure 5.7, the bridge boundary conditions have a major effect on the maximum deflection compared with the loading conditions. Cross-sections with less inertia will reach higher deflection values at lower applied loads as expected.

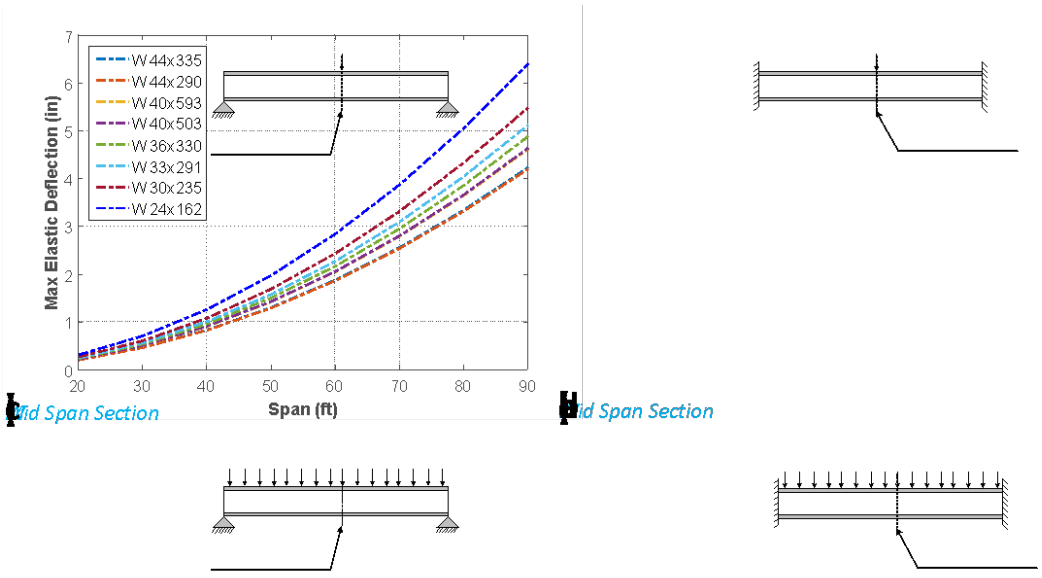

Figure 5.7 Relationship between the maximum elastic deflection and span length for different W sections for (a) simply supported BCs with concentrated load, (b) fixed BCs with concentrated load, (c) simply-supported BCs with uniform load, (d) fixed BCs with uniform load

Using a double composite section is expected to enhance a bridge's initial stiffness compared with the single composite section as mentioned earlier. The proposed analytical approach is used in this section to highlight the effect of adding a bottom slab to the regular single composite section. The previously mentioned eight steel sections from W 24x162 to W 44x335 are modeled as single and double composite sections for comparison, as shown in Figure 5.8. This figure shows a significant increase in the initial rotational stiffness of the section when a double composite configuration is used instead of a traditional single composite section for both positive and negative moment areas. This enhancement varies with the steel cross-section used as shown in the figure.

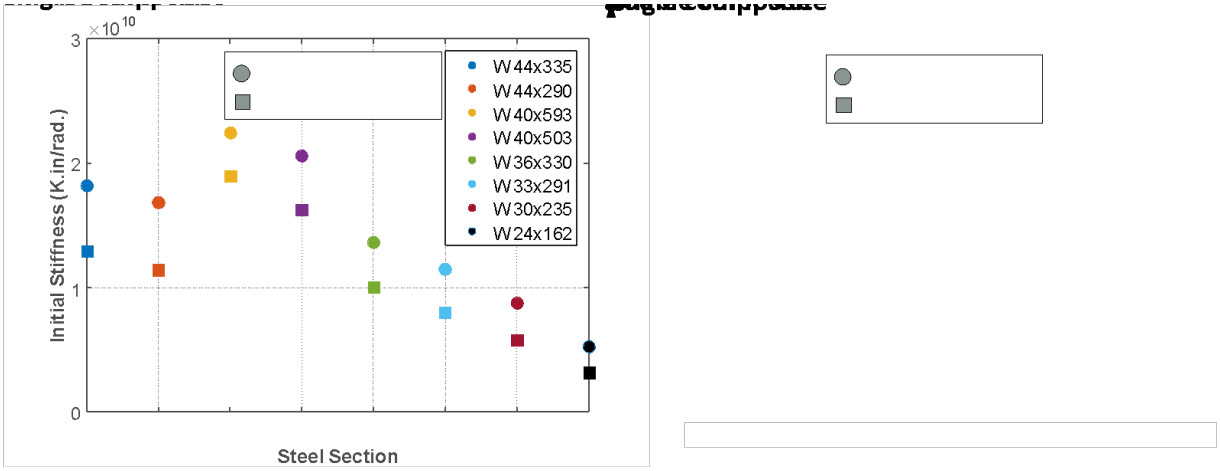

Figure 5.8 Comparison between the initial rotational stiffness (Kip.in/rad) for different single and double composite sections for: a) positive moment areas and b) for negative moment areas

Increasing the initial stiffness of the investigated bridge is also expected to increase the yield moment and reduce the maximum deflection. Using a double composite section on continuous bridges will enhance the bridge performance in the positive and negative moment areas and reduce the maximum deflection of the bridge. Therefore, in this section, a series of three span bridges are modeled using the analytical approach with different span lengths. The same eight cross-sections, which ranged from W 24x162 to W 44x335, are used for comparison. Figure 5-9 shows the comparison of the expected deflection of single and double composite bridges at the instance when the single composite bridges reach the AASHTO deflection limit state of L/800. The listed deflections are measured for a section located at 0.44L from the outer support, where L is the bridge span. A distributed load and equal spans are used for all investigated bridges. Figure 5.9 demonstrates that the double composite section can significantly reduce the maximum deflection of continuous bridges with a more evident effect for longer spans. It is important to emphasize that the double composite section will also increase the yield moment as noted in section 5.3.

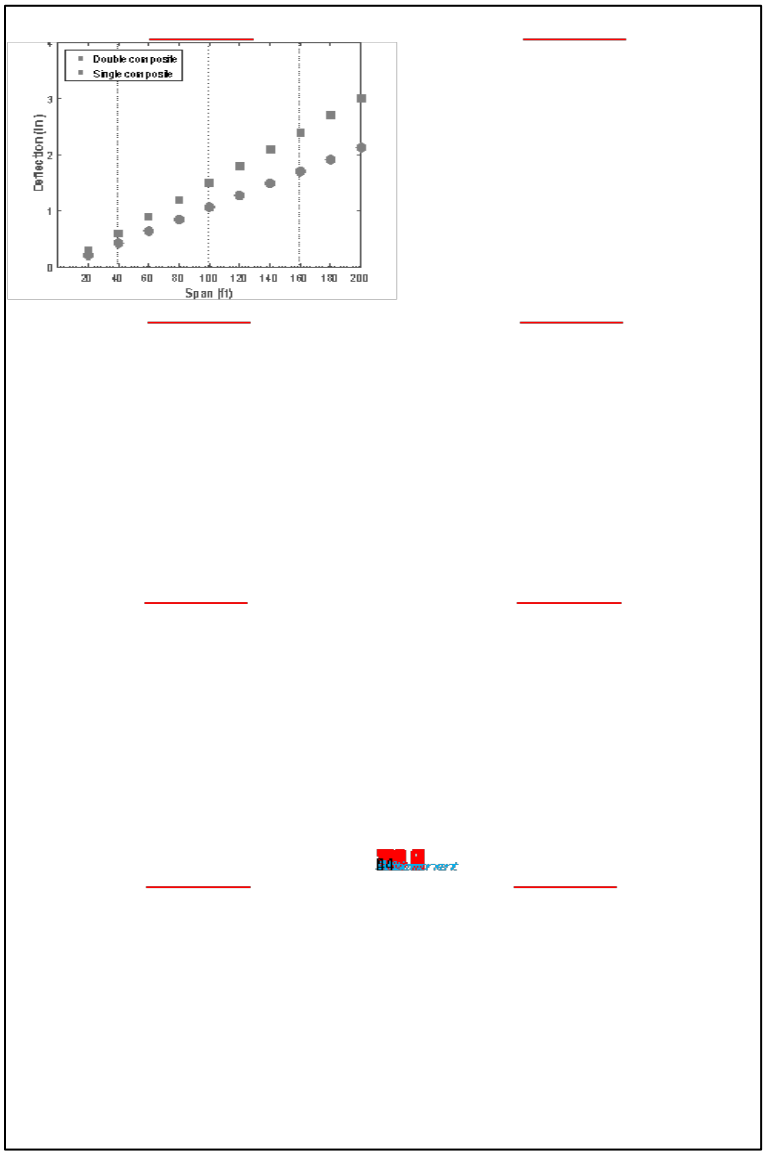

Figure 5.9 Comparison between the deflection of single and double composite sections versus the span length for three-span bridges built using different W sections

6. SUMMARY AND CONCLUSIONS

This study pertained to investigating the behavior of double composite bridges and quantifying the enhancement in deflection and moment capacity that can be gained by their employment in bridge construction. Analytical/mathematical formulations were devised where 13 different stress distributions are assumed. Numerical finite element models were developed using SAP2000 to model the elastic behavior and ABAQUS to simulate the performance of the double composite bridges in the elastic and plastic stages. These numerical models were then used to verify the proposed analytical formulations in which good agreements were found between the two approaches. Different bridge configurations were tested in this study to investigate the effect of the span length on the double composite bridges on their expected elastic deflection and initial stiffness. The following conclusions can be drawn from this study:

- The introduced analytical approach can be used as a computationally efficient method to determine the global performance of single and double composite bridges.
- The double composite section can significantly enhance bridge performance by reducing the elastic and inelastic deflection and increasing the yield and ultimate capacity of the bridge.
- Utilizing the double composite section resulted in the enhancement of the investigated bridges' behavior.
- The bridge loading and boundary conditions impacted the double composite bridge deflections as expected.

7. REFERENCES

Abbiati, G., Cazzador, E., Alessandri, S., Bursi, O. S., Paolacci, F., and Santis, S. De. (2018). "Experimental characterization and component-based modeling of deck-to-pier connections for composite bridges." *Journal of Constructional Steel Research*, Elsevier Ltd, 150, 31–50.

ACI Committee 318. (2014). *Building Code Requirements for Structural Concrete: (ACI 318-14) ; and Commentary (ACI 318R-14).* Farmington Hills, MI.

American Association of State Highway and Transportation Officials. (2012). *AASHTO LRFD Bridge Design Specifications*. Washington, DC 20001.

Bharil, R.K. (2016). "Girders." *Innovative Bridge Design Handbook Construction, Rehabilitation and Maintenance*, A. Pipinato, ed., Elsevier Inc., Butterworth Heinemann, 359–382.

Culver, C. (1960). *The Moment Curvature for Composite Beams*.

Deng, Y., and Morcous, G. (2013). "Efficient Prestressed Concrete-Steel Composite Girder for Medium-Span Bridges. I: System Description and Design." *Journal of Bridge Engineering*, 18(12), 1347–1357.

EN 1992-1-1. (1992). *Eurocode 2: Design of concrete structures Part 1-1: General rules and rules for buildings*. (European Committee for Standardization (CEN), ed.), Brussels.

M., D. Miranda (2016). "Long-span bridges." *Innovative Bridge Design Handbook Construction, Rehabilitation and Maintenance*, A. Pipinato, ed., Elsevier Inc., Butterworth Heinemann, 383–425.

Matos, J. C., Moreira, V. N., Valente, I. B., Cruz, P. J. S., Neves, L. C., and Galvão, N. (2019). "Probabilistic-based assessment of existing steel-concrete composite bridges – Application to Sousa River Bridge." *Engineering Structures*, Elsevier, 181(December 2018), 95–110.

Mendes, T. A. A. (2010). "Mixed Steel-Concrete Trays with Double Mixed Action." Technical University of Lisbon, Portugal.

Pańtak, M. (2012). "Double composite bridges: The main concept and examples of its implementation." 244–251.

Patel, P. (2009). "LRFD design of double composite box girder bridges." University of South Florida.

Rodriguez, S. (2004). "Design of Long Span Concrete Box Girder Bridges: Challenges and Solutions." *Structures Congress*, Structural Engineering Institute of ASCE, Nashville, Tennessee, 1–11.

Saul, R. (1997). "Design and Construction of Long Span Steel Composite Bridges in Composite Construction in Steel and Concrete III." *Proceedings of an Engineering Foundation Conference*, Irsee, Germany, 700–712.

Sennah, K. M., and Kennedy, J. B. (2002). "Literature Review in Analysis of Box-Girder Bridges." *Journal of Bridge Engineering*, 7(April), 134–143.

SteelConstruction.info. (2019). "Box girder bridges." *Bridges*, <https://www.steelconstruction.info/Box_girder_bridges>.

Stroh, S. L., Sen, R., and Ansley, M. (2010). “Load Testing a Double-Composite Steel Box Girder Bridge.” *Journal of the Transportation Research Board*, 36–42.

Stroh, S., and Sen, R. (2009). “Steel Bridges with Double-Composite Action: Innovative Design.” *Journal of the Transportation Research Board*, 1696(1), 299–309.

Wordpress. (2015). “Box Girder Bridges.” *Civil Engineering*, <https://erkrishneelram.wordpress.com/2015/03/12/box-girder-bridges/>.

Xu, C., Su, Q., Wu, C., and Sugiura, K. (2011). “Experimental study on double composite action in the negative flexural region of two-span continuous composite box girder.” *Journal of Constructional Steel Research*, Elsevier Ltd, 67(10), 1636–1648.

Yen, B. T. (1982). *Strength of rectangular composite box girders: recommendations for design of composite box girders final report*. Fritz Laboratory Reports.